The Formation of Parallel and Perpendicular Collisionless Shocks in the Big Red Ball

by

Douglass A. Endrizzi

A dissertation submitted in partial fulfillment of
the requirements for the degree of

Doctor of Philosophy

(Physics)

at the

UNIVERSITY OF WISCONSIN–MADISON

2021

Date of final oral examination: 06/25/2021

The dissertation is approved by the members of the Final Oral Committee:
Cary Forest, Professor, Physics
Jan Egedal, Professor, Physics
John Sarff, Professor, Physics
Ellen Zweibel, Professor, Physics
Riccardo Bonazza, Professor, Engineering Physics

CONTENTS

LIST OF TABLES

LIST OF FIGURES

ABSTRACT

Collisionless shocks have been observed both in simulations and in spacecraft observations to exhibit strong ripples and undergo cyclic reformation processes [13, 72, 79, 67, 58]. For a nonstationary shock that frequently reforms, the formation mechanism becomes an important part of the overall time averaged shock structure. Two laboratory pulsed power experiments designed to investigate collisionless shock formation mechanisms were performed: the first by using a theta pinch compressing a cylindrical plasma, and the second with a coaxial plasma gun firing into a plasma along the magnetic field direction. These two configurations, where the shock normal is first perpendicular and second parallel to the magnetic field, allow for full exploration of the range of shock geometries. The results from both experiments can be mostly explained by Hall-Magnetohydrodynamic theory, describing magnetized fluid electrons and ions that are unmagnetized on either spatial or temporal scales. Reflected ions are a distinct feature of both experiments, as are Hall currents and whistler waves (both Hall-MHD phenomena). Comparing dimensionless parameters (plasma beta, alfvén Mach number, magnetic Reynolds number) between these laboratory experiments and heliospheric shocks indicate that the observations here may hold particular relevance to interplanetary and bow shocks. Suggested upgrades that might extend the experiment durations to several ion cyclotron periods are presented.

1 INTRODUCTION AND SCIENTIFIC MOTIVATION

A shock is a fluid discontinuity that appears generally whenever flow speeds approach or exceed the fastest wave speed of the medium. The sonic boom produced by a supersonic aircraft, the crack of a whip or the sound of a thunderclap are familiar examples. The average human has mercifully little experience with these loud phenomena. Nonetheless, one might have experience with the stop-and-go motion of a highway traffic jam, the crashing of waves at the beach, and the cavitation of motorboat propellers, all of which involve analogues of shock dynamics.

While neutral shocks take the directed kinetic energy and efficiently convert it to thermal energy, plasma shocks can redistribute this flow energy in myriad ways: into an unequal partition of thermal energy between electrons and ions, into electromagnetic wave energy and radiation, and even into the acceleration of high energy particles and cosmic rays. From a fundamental science perspective, this complexity makes them very interesting. While we as a scientific community understand much about how plasma shocks work, we do not have a complete theory that would allow us to make predictions about this energy redistribution for all environments [16].

And shocks do appear in nearly all plasma environments. In the heliosphere, we observe planetary bow shocks, forward and reverse shocks around interplanetary coronal mass ejections, photospheric flare induced shocks, and the solar wind termination shock. Beyond the heliosphere, astrophysical shocks include galactic halo shocks, shocks in accretion flows, radio lobe termination shocks, supernova remnant shocks, et cetera. The spiral arms of the Milky Way galaxy are not stationary structures, but are in fact propagating shock waves [34]. This ubiquity makes understanding plasma shocks, particularly collisionless shocks, all the more important.

It is well known that collisional shocks are mediated by particle-particle collisions. These collisions provide the source of dissipation in the shock layer that converts the directed flow kinetic energy into thermal energy. However, most of the aforementioned heliospheric and astrophysical shocks are fully collisionless. That is, the observed shock layer is much thinner than the particle-particle mean free path. In collisionless shocks, some other dissipation mechanism must fill that role. Often this means scattering off of electromagnetic waves and turbulent fluctuations.

While in collisional shocks the energy transformation is well described analytically [66], collisionless shocks are vastly more complicated. The flow energy can be converted into an unequal energy partition between electron and ion species, into strong electromagnetic waves or radiation, or into energetic particles and cosmic rays. The ability to predict the

flow of energy in a collisionless shock would enable more accurate astrophysical models all of the above systems. This could improve near earth space weather forecasting [16], our understanding of cosmic ray acceleration [19], models of galactic evolution [59], and more.

In the half century since the existence of collisionless shocks was properly accepted by the scientific community [100], spacecraft observations and computational simulations have vastly advanced our understanding of collisionless shocks. However, both of these scientific avenues are limited in particular ways: repeatibility and coverage are challenges for spacecraft measurements, while expense and fidelity are current barriers to computational simulations. Laboratory experiments, while also limited in particular ways, can complement these other approaches.

This thesis describes laboratory experiments conducted to test our understanding of how collisionless shocks form. There are two primary experimental configurations: the perpendicular shock with a traditional theta-pinch geometry, and the parallel shock which uses a coaxial plasma gun. Together these two experiments explore a range of parameters, and in certain ways are comparable to the Earth's bow shock and interplanetary shocks.

One particular limitation of these experiments is in the definition of "collisionless." While the experiments exhibit ions that are effectively collisionless (the ion mean free path λ_{mfp}^{i} is larger than the experiment size), the electron temperature T_e is always too low and the density n_e too high for the electrons to be anything less than moderately collisional. This is often the case for laboratory experiment, and serves as a reminder that these are *c*omparable with and not *i*dentical to heliospheric shocks, which are truly devoid of Coulomb collisions. This high collisionality may limit the types of dissipative instabilities that would otherwise appear.

A second limitation is in the experimental duration. While the bow shock exhibits cyclic reformation in both the parallel and perpendicular configurations, it generally exists in a fully developed turbulent state evolved from from many ion cyclotron periods ω_{ci}^{-1}. For these experiments, observing development for longer than a few ω_{ci}^{-1} is challenging. These experiments are then particularly relevant to early times in the shock formation/reformation process. However, as collisionless shocks are often non-stationary or exhibit cyclic reformation, this formation structure may be a significant part of its overall average state rather than a one-and-done event.

In spite of these limitations, this work allows for two general statements about collisionless shocks and their formation process. First, Hall effects between the ion and electron species are generally important. This is a somewhat tautalogical statement: shocks appear when flow speeds exceed Alfv'enic speeds, which violates the condition of single fluid MHD that the system changes slower than ion gyroperiod ω_{ci} or ion plasma period ω_{pi}

scales. Second, the reflection of ions from moving potentials is a characteristic feature of collisionless shocks. In this experimental work, these two effects dictate the configuration of the shock as it evolves.

The vast majority of what was learned in the course of this thesis is experimental in nature: isolating and measuring signals in noisy environments, working safely with pulsed power, producing reliable target plasmas, et cetera. For the future graduate student or postdoc working on the Big Red Ball (BRB), I document these experimental details to serve as a useful reference. However, such discussion distracts from the interpretation of the experimental results. When possible, experimental details have been moved to appendices. This is not a diminution of the work therein, which I consider to be the foundation of these results.

The following chapter presents theory and background necessary for interpreting the experimental work. Chapter 3 presents results from the perpendicular theta-pinch shock experiments. Chapter 4 discusses the parallel shock experiment results. And finally Chapter 5 summarizes and explores possible future experimental work. Appendix A provides a complete derivation of the MHD Rankine-Hugoniot jump conditions. The remaining appendices are entirely experimental: B discusses the Compact Toroid Injector (CTI) development and operation. C documents probe development for shock and pulsed power plasma environments. D details upgrades and use of the plasma washer guns and pulse forming networks on the BRB.

2 SHOCK PHYSICS OVERVIEW

This thesis aims to answer experimentally the question of how collisionless shocks form. That is, what happens when a fast collisionless flow encounters an impenetrable piston? How does that structure evolve into the quasi-steady state conditions we observe in fully developed shocks?

To properly interpret the experimental results, substantial background theory is presented in this chapter. The intended audience is an early graduate student looking to begin shock focused work on the Big Red Ball. The following two paragraphs give a brief summary and interpretation of the experiments. If reading them is trivial, then consider skipping this chapter.

Perpendicular Shock Experiment

The first primary shock experiment on the Big Red Ball models a perpendicular collisionless shock. As a supersonic flow impinges on a magnetic piston, ions are specularly reflected from the piston front. This reflection mechanism is well explained by Hall-Magnetohydrodynamics: as the magnetized electron fluid separates from the ion fluid by up to the ion skin depth, a restoring ambipolar potential is established. This moving potential leads to near total specular reflection of ions. The speed u_p at which the piston penetrates is dictated by pressure balance between the piston magnetic pressure and the incoming/reflected ion ram pressure $2\rho u_p^2$. These reflected ions form a gyrating distribution amidst the cold background flow. When they re-encounter the piston they alter the pressure balance, slowing the speed at which the piston penetrates and themselves forming the "shocked" downstream population. Dynamics beyond this point are limited by the experiment size and duration. However, theory suggests a smaller potential jump would appear at the leading edge of the downstream population that, on average, reflects a fraction of ions so as to satisfy mass, momentum, and energy continuity. At such a point, the collisionless reflection dissipation mechanism has decoupled from the piston and a "canonical" shock has formed.

Parallel Shock Experiment

The second BRB experiment explores the parallel shock configuration. As in the first experiment, a collision of a supersonic flow with a piston also produces reflected ions. As the electron fluid is coupled to the magnetic field, the ion skin depth scale reflection mechanism naturally generates dispersive whistler waves. Our cylindrical experimental

geometry exhibits a concave-forward cone shaped potential, and from that we observe ion reflection that is not perfectly specular but in fact heats this reflected ion population above its initial temperature. Unlike the perpendicular case, these ions will not gyrate back to the layer and automatically lead to shock-piston detachment. Instead, resonant cyclotron interaction (or possibly non-resonant interaction) with the upstream whistlers can cause those whistlers to grow in amplitude until they can scatter these reflected ions back towards the piston and also reflect incoming upstream ions. At such a point, the dissipation mechanism has detached from the piston and again a canonical shock has been formed.

To repeat: if any part of the above two paragraphs was confusing to you, this chapter may be useful. Otherwise, feel free to skip this pedantic refresher.

This chapter will begin with an introduction to fluid/hydrodynamic shocks, followed by extension of the fluid theory to plasmas and magnetohydrodynamic (MHD) shocks, and then finally some experimentally relevant complications of collisionless shocks will be introduced. The purpose here is not rewrite the many good reviews and books that exist, but to provide an experimentalist understanding of collisionless shock formation. Suggestions for further reading are provided throughout.

In the following sections, a theory of shock formation in the analytically tractable case of collisional and MHD shocks is introduced. This single fluid theory fails when extended to collisionless shocks. An attempt to repair that with Hall-MHD is presented. While there are many further features of collisionless shocks, only issues particularly relevant to interpreting the experimental results are discussed.

2.1 Shock Formation from Non-Linear Wave Steepening

One simple description of collisional shock formation relies on non-linear wave steepening. The term non-linear is used here to indicate that the wave speed depends on the wave amplitude. To illustrate by way of example, let's imagine a pressure wave in a neutral, compressible fluid with sound speed c_s defined as:

$$c_s^2 \equiv \frac{\gamma P}{\rho} \tag{2.1}$$

Where P is the pressure, ρ the mass density, and γ the adiabatic index defined as the ratio of specific heats at constant pressure and constant volume. The adiabatic index γ is fundamentally related to the degrees of freedom f of the gas, where $\gamma = (f+2)/f$, and is

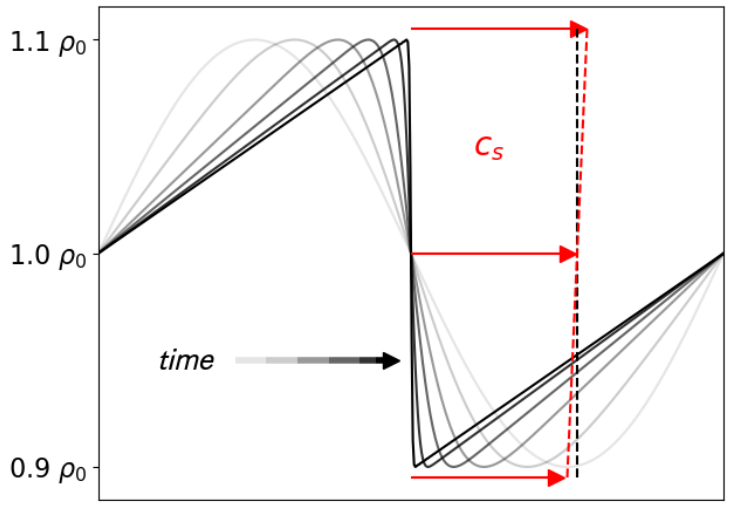

Figure 2.1: A simple diagram showing how a large amplitude sinusoidal pressure wave might non-linearly steepen by velocity dispersion. The shaded colors represent different moments in time, remaining in the wave reference frame as it translates in space.

1.4 for air, with a max value of 3 in a one dimensional system. For adiabatic compression $P = \rho^\gamma$, the sound speed becomes $c_s = \sqrt{\gamma P_0 \rho^{\gamma-1}}$, and since $\gamma > 1$ this means that as the density increases, so does the sound speed.

This peculiar property leads to wave dispersion, where larger amplitude waves travel faster. Figure 2.1 shows a simple depiction of this non-linear steepening. For an initially sinusoidal compression, as time passes the denser peaks will catch up to the slower troughs and form a steep discontinuity or shock.

The steepening is ultimately limited by dissipation in the strong gradient. The shock thickness thins to the order of the largest dissipation scale length [66, 26]. While for neutral shocks this is trivially the particle-particle mean free path, this dissipative scale length argument is useful when considering plasma shocks where many dissipation mechanisms (resistivity, viscosity, thermal conductivity, instabilities, etc.) are possible.

Let's put values to this to build some intuition. For a $\gamma = 5/3$ ideal gas, a 10% compression in the density increases the sound speed by 7%. The time it takes for the fast crest to overtake the background is approximately $t \sim (\lambda_0/4)/(c_s^{max} - c_{s0})$. For a 262 Hz Middle C, a shock could form in 14 ms or within 5 m of propagation given $c_s = 343$ m/s. However, this 10% compression is far louder than a passenger jet at takeoff.

This idea of shock formation via steepening is particularly useful when combined with the piston driven shock model. In that framework, we imagine a fast flow colliding with a stationary piston, or equivalently a fast moving piston through a stationary fluid. For flow speeds well below the sound speed (subsonic), pressure/sound waves can transmit information into the upstream/oncoming flow and move the fluid mass out of the way of the piston. Above the sound speed, sound waves cannot travel into the upstream. The fluid immediately in front of the piston is compressed, leading to a local increase in the

density and adiabatically increasing the temperature. This increases the local sound speed, and now pressure waves are able to move the fluid out of the way of the piston. A new equilibrium is reached where the incoming flow is slowed and compressed in the shock As particle collisions are the fundamental mechanism in pressure waves, we expect that the formation of a shock in front of a supersonic piston occurs on the order of a few particle collision times ν^{-1}.

2.2 Hydrodynamic Shock Derivation

Hydrodynamic or fluid systems exhibit collective behavior provided by frequent inter-particle collisions. These frequent elastic scatterings force the probability distribution function towards a Maxwell-Boltzmann distribution, the maximal entropy configuration. In this section, we briefly summarize the fluid shock derivation based off the work done by W.L.M. Rankine in 1870 and H. Hugoniot in 1887.

Shock behavior can be derived quite simply with the following one-dimensional continuity argument. First, presuppose the existence of a time-stationary planar discontinuity of infinitesimal thickness, separating a homogeneous normal inflow upstream from a homogeneous outflow downstream.[1] A simple diagram is given in the top row of figure 2.2. The problem can now be framed: given the upstream density n, temperature T, and inflow velocity v, calculate the downstream parameters.

Across the shock layer we require the conservation of mass, momentum, and energy, which is always true. We can represent those three constraints as the fluid continuity equations:

$$\frac{\partial \rho}{\partial t} + \nabla \cdot \rho \boldsymbol{v} = 0 \tag{2.2}$$

$$\frac{\partial \mathbf{p}}{\partial t} + \nabla \cdot \mathbb{T} = 0 \tag{2.3}$$

$$\frac{\partial \mathcal{E}}{\partial t} + \nabla \cdot \mathbf{Q} = 0 \tag{2.4}$$

Where $\rho = mn$ represents the mass density, $\mathbf{v}$ the velocity, $\mathbf{p}$ the momentum, $\mathbb{T}$ the stress tensor, E the scalar energy, and $\mathbf{Q}$ the energy flux vector. Importantly, because of the collisional nature, we can assume pressure is a scalar and thus provide a closed set definitions

[1] Many of these assumptions are inappropriate for collisionless shocks, as will be discussed later.

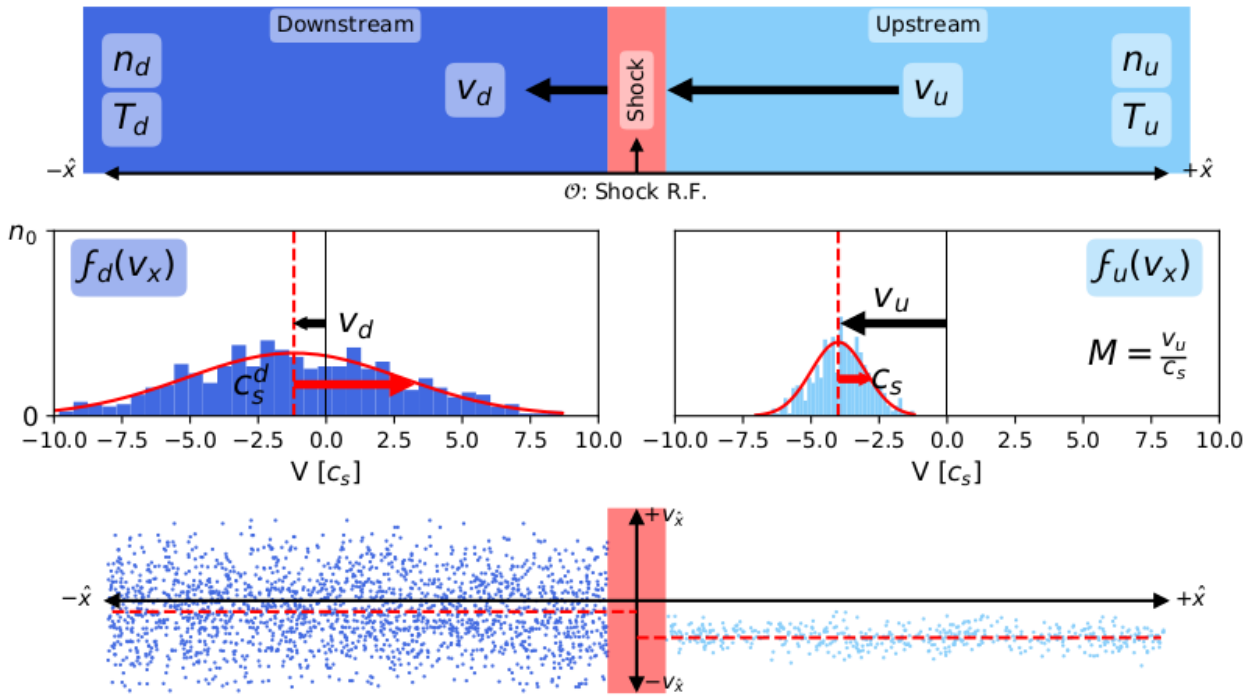

Figure 2.2: A canonical depiction of a hydrodynamic shock in the shock layer reference frame. The shock converts the fast flowing but cold upstream into a weakly flowing but hot downstream, dissipating the flow kinetic energy via collisions. The top row represents the 1-D geometry of the system, with an upstream and a downstream separated by a thin shock transition layer. The "piston" is somewhere to the left moving away at the downstream flow speed. The middle row shows particle distribution functions for the upstream and downstream, normalized to the upstream density, $n_u = \int_{-\infty}^{+\infty} f_u(v_x) dv_x$. The scales accurately depict a M = 4.0 shock using Eqs. 2.8 and 2.9. The bottom is a phase-space representation of the middle row generated from the statistical distributions of 10^3 particles and not from a kinetic simulation. This phase-space representation will be useful in comparing to collisionless shocks later.

for $\mathbb{T}$, E, and $\mathbf{Q}$:

$$\mathbb{T} = P\mathbb{1} + \frac{\rho \boldsymbol{v}\boldsymbol{v}}{2} \tag{2.5}$$

$$\mathcal{E} = \frac{\rho v^2}{2} + \frac{P}{\gamma - 1} \tag{2.6}$$

$$\mathbf{Q} = \left(\frac{\rho v^2}{2} + \frac{\gamma}{\gamma - 1} P \right) \boldsymbol{v} \tag{2.7}$$

The continuity equations can be solved via integration, as will be described in the next section and in Appendix A. Defining the Mach number $M = v/c_s$, the sound speed

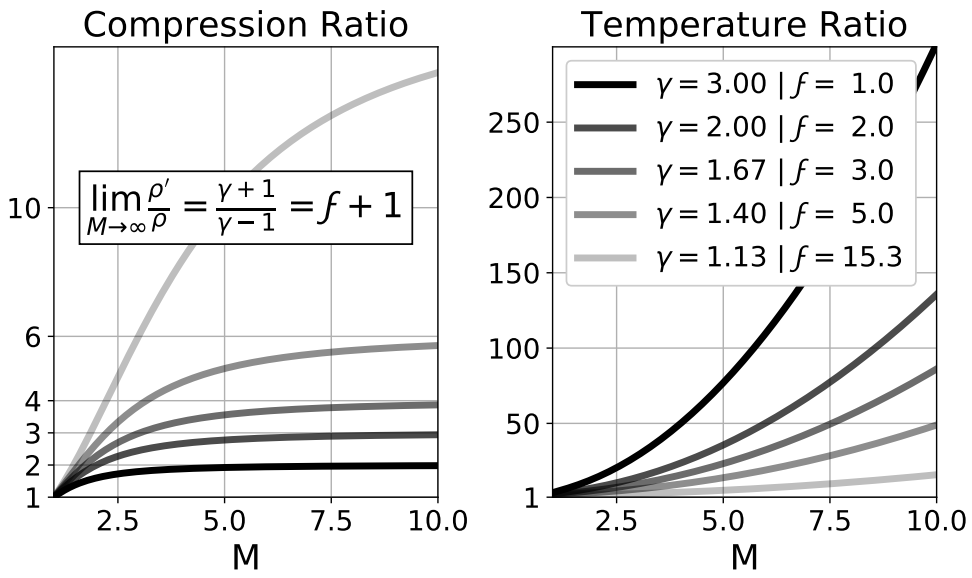

Figure 2.3: Solutions to the fluid Rankine-Hugoniot jump conditions for shocks of varying adiabatic index, from Eqs. 2.8 and 2.9. Note that the density compression ratio tends to a finite value that depends on the degrees of freedom of the fluid, while the temperature jump increases without bound. $\gamma = 3$ describes a 1-D (one degree of freedom, $f = 1$) fluid. $\gamma = 2$ describes a 2-D fluid (or strongly magnetized 3-D plasma). $\gamma = 5/3$ describes an ideal monatomic gas with 3 degrees of freedom. $\gamma = 1.40$ describes an ideal diatomic gas with $f = 5$, which happens to be $\sim 99\%$ of our atmosphere, and finally $\gamma = 1.13$ is the measured value for propane, with $f \sim 15.3$

$c_s = \sqrt{\frac{\gamma P}{\rho}}$, and the density compression ratio $\delta = \rho'/\rho$, we find:

$$\delta = \frac{\rho'}{\rho} = \frac{(\gamma+1)M^2}{(\gamma-1)M^2+2} \tag{2.8}$$

$$\frac{P'}{P} = \frac{2\gamma M^2 - (\gamma-1)}{\gamma+1} \tag{2.9}$$

The temperature jump across the shock is easily found by combining equations 2.8 and 2.9, using $P = nT$.

Figure 2.3 plots the shock density and temperature ratios as a function of Mach number for a selection of adiabatic indices. Note that, as the Mach number increases, the density compression ratio tends to a finite value that depends directly on the degrees of freedom available to the fluid particles. For atmospheric gases with $\gamma = 1.4$, at high Mach number the density compression ratio δ approaches 6. In contrast with the density, the temperature ratio increases without bound. Historically, this efficient temperature scaling was the motivating factor for fusion scientists looking to achieve thermonuclear ignition through shock heating.

This surprising behavior is a result of satisfying mass, momentum and energy continuity simultaneously in a collisional fluid. When higher vibrational modes, ionization, radiation, or any energy pathway become accessible, this changes the available degrees of freedom f and hence the adiabatic index γ. For example, at very high Mach numbers neutral particles can dissociate into plasma; this ionization acts as another degree of freedom, further increasing the compression ratio.

We have assumed that interparticle collisions provide the dissipation in the layer. This suggests that the mean free path λ_{mfp} is a likely scale length for the thickness Δ of the layer. More careful theory suggests that the minimum fluid shock thickness occurs around $M = 3.6$ and is about $6\,\lambda_{mfp}$ thick [11]. This supports the hypothesis earlier that a collisional shock would form in a few collision times.

2.3 Fluid Plasma and Magnetohydrodynamic Shocks

Significantly more complexity is introduced when the fluid being considered is a plasma. With two species there are three collisional scale lengths: the electron-ion λ_{ei}, the ion-ion λ_{ii}, and the electron-electron λ_{ee} mean free paths. In fluid terms, these types of collisions are represented by resistivity, viscosity, and thermal conductivity.

In addition, the disparate proton/electron mass ratio $\mu = m_p/m_e = 1836$ means that large Mach number flows relative to the ion thermal speed may be small relative to the electron thermal speed. That is, only the ions may experience a shock and the electrons are instead collisionally coupled. A simple depiction of this state in a collisional fluid plasma shock is shown in Fig. 2.4.

As plasmas are made of charged particles that interact via the Lorentz force, we need to re-derive the Rankine-Hugoniot jump conditions for an MHD shock. This is substantially more complicated and is performed in excruciating detail in Appendix A. The result is the MHD Rankine-Hugoniot Shock Adiabatic equation:

$$\begin{aligned} 0 = &\left[v_n^2\left[(\gamma-1)(\delta+1)-2\gamma\right]+2\delta c_s^2\right]\left(v_n^2-\delta v_A^2\cos^2\theta\right)^2 \\ &-\delta v_n^2 v_A^2\sin^2\theta\left[v_n^2\left[\gamma(\delta+1)-2\delta(\gamma-1)\right]-\delta v_A^2\cos^2\theta\Big((\gamma-1)(\delta+1)-2\gamma\Big)\right] \end{aligned} \tag{2.10}$$

where v_n is the upstream normal velocity, δ is the compression ratio $\rho_{down.}/\rho_{up.}$, $\theta = \theta_{bn}$ the upstream angle between the shock normal and magnetic field, and c_s and v_A the upstream sound and Alfvén speeds.

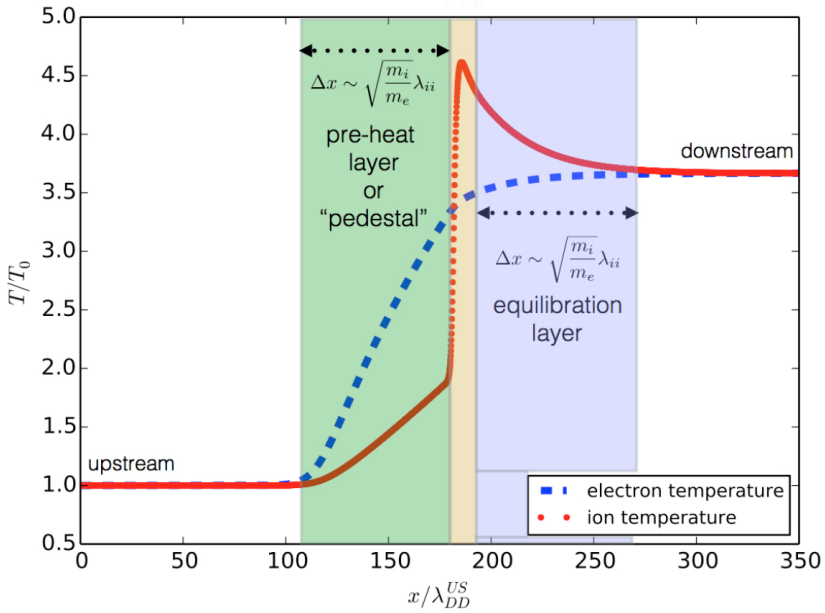

Figure 2.4: Diagram showing the temperature jump for each species in a strong ($M \gg 1$), collisional, Helium plasma shock. The width of the shock region in the center is over 10 mean free paths thick, while the equilibration regions upstream an downstream are larger by the square root of the mass ratio. Image taken from Keenan et al 2017.[68]

In the $\delta = 1$ zero compression limit, the above equation recovers the three standard Fast magnetosonic, Intermediate, and Slow magnetosonic MHD waves. This suggests that the MHD shock solutions are steepened branches of these waves. These wave speeds are plotted in polar coordinates in Fig. 2.5 in what's known as a Friedrich Diagram. While each wave has its own Mach number (M_f, M_I, M_s), when unspecified the Mach number generally refers to M_f.

The Friedrich diagram raises an important point about compressibility and the relationship between the magnetic field and the plasma density. As shown in Fig. 2.7, perpendicular compression of a flux tube increases the magnetic field strength proportionally with the density. Parallel compression increases the density without changing the field strength. This is apparent in the Friedrich diagram: for $\beta < 1$, the incompressible Shear Alfvén wave is the Fast mode in the parallel direction, while in the perpendicular direction the wave becomes compressible.

Interpreting the MHD Shock Adiabatic equation (Eq. 2.10) is complicated. A very nice diagram of the possible types of MHD discontinuities is given by De Sterck [32] and reproduced in Fig. 2.6. Early interpretations of collisional experimental work relied heavily on this classification system (see, e.g. [28]).

As the two BRB experiments are limiting cases ($\theta_{bn} = 0$ and $\pi/2$), the possible waves are restricted further: in the perpendicular case there is only one wave speed (Fast magnetosonic) and so only one MHD shock solution. In the parallel case, from Fig. 2.6 only the Hydro shock or the Switch-On shock are possible solutions. Experimental deviations from these ideal cases will reveal the obvious limitations of applying a theory of slow

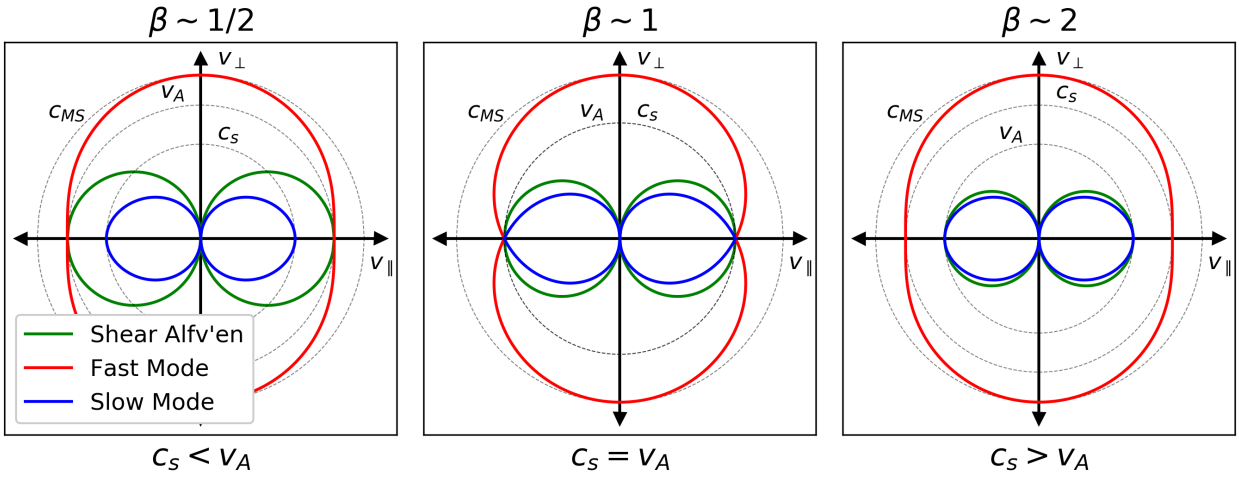

Figure 2.5: A Friedrich diagram, showing the ideal MHD wave solutions for three values of plasma beta. These polar plots show the wave speeds as a function of polar angle for the Fast (Magnetosonic), Intermediate (Shear Alfvén), and Slow modes. For purely perpendicular flows, the interpretation is simple: flow speeds need only to exceed the Fast speed for a shock to form. For parallel and quasiparallel flows multiple solutions can exist.

phenomena (MHD) to an abrupt discontinuity.

Analytic solutions to the internal structure of a collisional plasma shock wave were attempted by adding dissipative terms (resistivity, viscosity, thermal conductivity) to the continuity equations and solving for a stable solution connecting the two states. This was nicely demonstrated by Coroniti in 1970 [26]. A simplified interpretation is that shock steepening is limited by the dominant dissipative mechanism, which is usually resistivity, but sometimes with additional viscosity, and never thermal conductivity.

Applying the conclusions in Coroniti to BRB experiments contradicts some experimental results. For typical laboratory plasmas of $n_e = 10^{18}/m^3$ and $T_e = 2eV$, the shock layer would need to thin down to millimetres before the current density is high enough that resistivity can provide the necessary dissipation. This is far smaller than the observed layer width, which is on the order of the ion skin depth $c/\omega_{pi} \sim 18$ cm. Coroniti directly acknowledged the limitations of an MHD theory in collisionless plasmas, and said that two fluid effects, turbulent electromagnetic waves, and finite Larmor radius effects need to be properly included. Nonetheless, such work is useful to discriminate collisional from collisionless behavior.

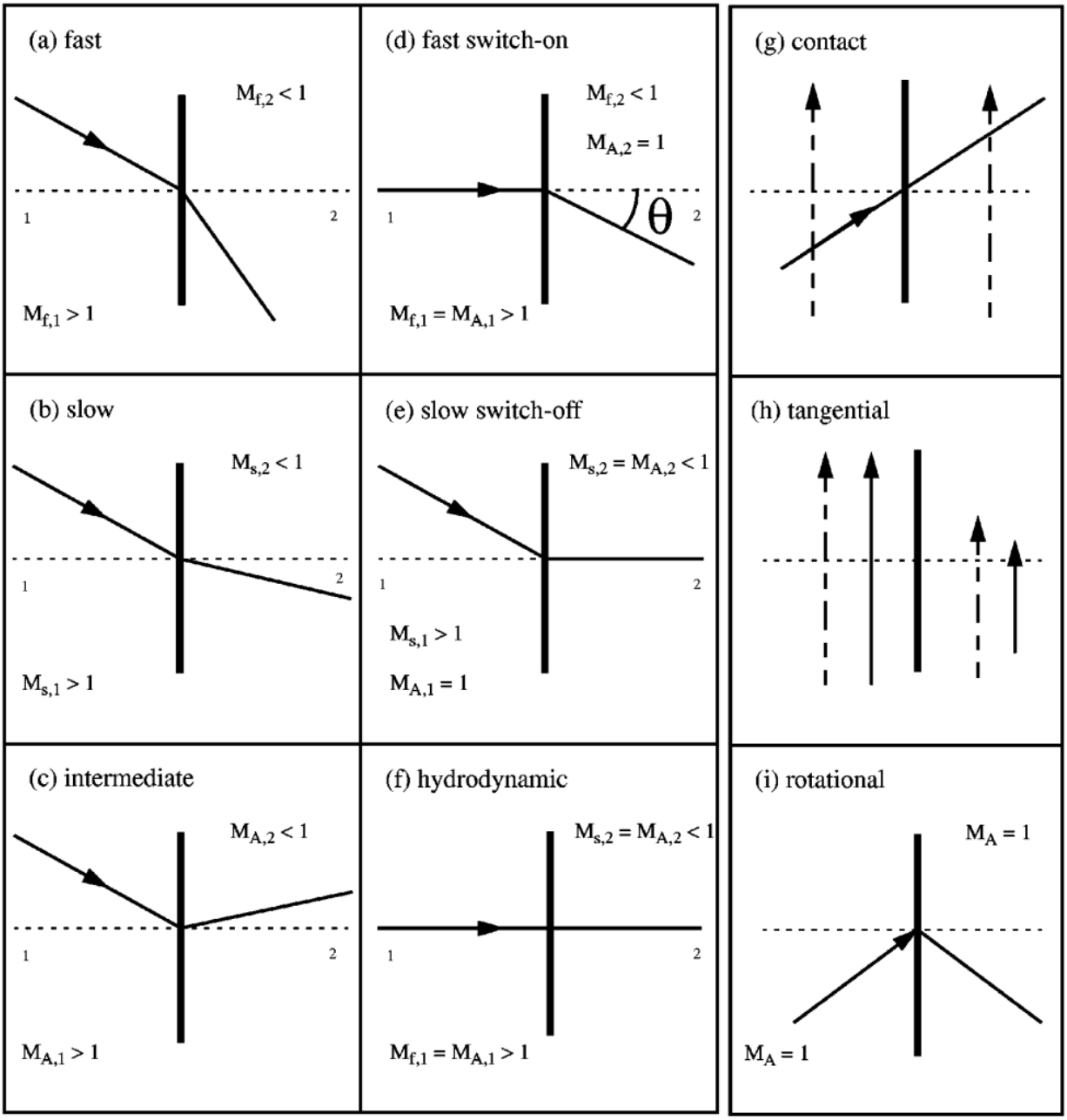

Figure 2.6: A complete description of possible MHD discontinuities from solutions of the shock adiabatic equation, Eq. 2.10. The thick vertical line and the dashed horizontal line are the shock and the shock normal. Magnetic field lines are represented by the arrowed lines, while the dashed arrowed lines are velocity vectors shown only when $\hat{b} \parallel \hat{v}$. Region 1 is upstream, 2 is downstream. Figure reproduced from De Sterck, 1998 [32].

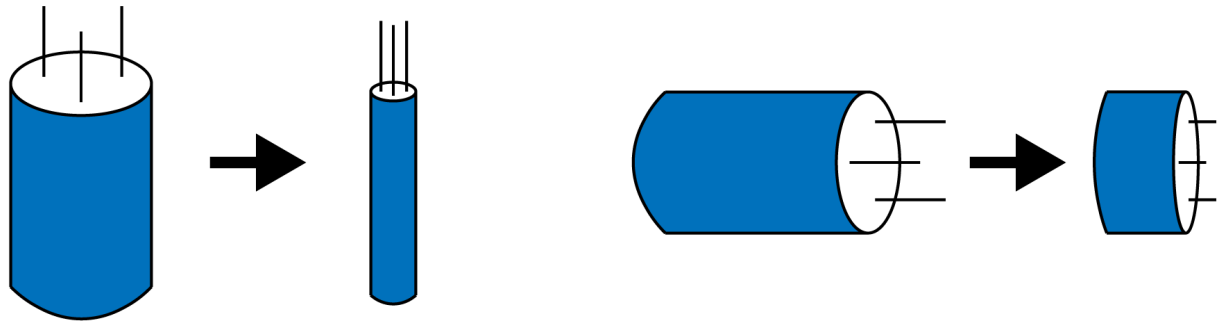

Figure 2.7: A simple diagram showing the difference between perpendicular and parallel compression of magnetic fields. In the perpendicular direction, compression changes the density of magnetic field lines, and thus the magnetic pressure/energy density. The same compression in the parallel direction does not change the field line density. This heuristic argument is often invoked to argue that only the perpendicular component of the field is involved in setting the RH jump conditions. The parallel magnetic field nonetheless plays an important role in shock formation and evolution through whistler wave dynamics.

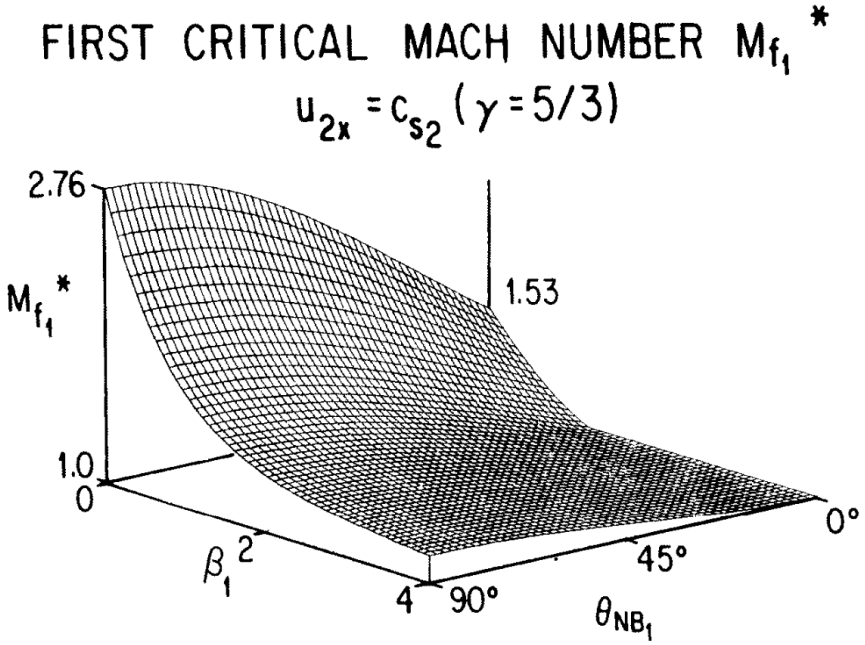

Figure 2.8: The first critical Mach number surface, plotted as a function of the Alfvén Mach number and the shock normal direction θ_{bn}. For a high-β shock, the Mach number can be quite low before the required dissipation exceeds the maximum possible resistive dissipation. Figure reproduced from Edmiston and Kennel, 1984 [36].

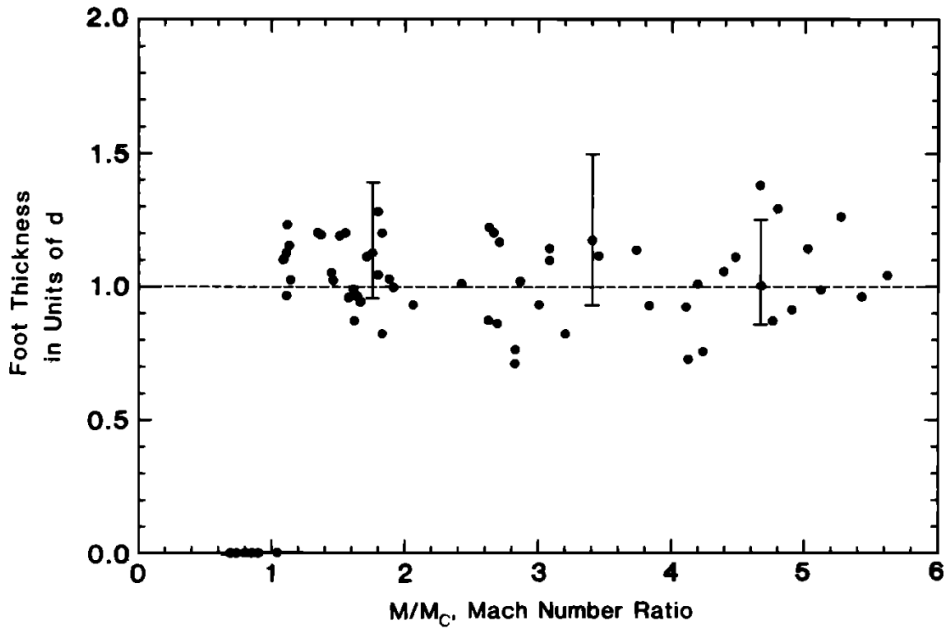

Figure 2.9: Spacecraft observations of the thickness of the shock foot against the Mach number normalized to the first critical Mach number for ion reflection. Above the first critical Mach number, a reflected ion foot is observable in spacecraft data. Later work by Greenstadt and Mellot examined wave signatures of reflected ions and found them present even in subcritical shocks [55], suggesting that the threshold is not so sharp. Figure reproduced from Livesey et al. 1984 [74].

2.4 Ion Reflection in MHD: the First Critical Mach Number

Before we talk in detail about the limits of MHD theory, the work by Coroniti and others directly acknowledges these limits through the identification of a critical Mach number M_c. In perpendicular shocks, as the Mach number gets large the magnetic field compression ratio asymptotes to the density compression ratio $\delta(\gamma, M)$. However, the plasma temperature heats without bound (Fig. 2.3). Since resistivity is dissipating the magnetic energy which is limited to the finite value $(\delta - 1)B_0^2/2\mu_0$, then that there is some threshold where the required dissipation and heating exceeds the maximum resistive dissipation. This threshold, which is solved analytically by Edmiston and Kennel in 1984 [36], is plotted in Fig. 2.8.

In the single-fluid MHD framework, the existence of this critical Mach number means that some other dissipation mechanism must step in. Above M_c, one could have a resistive shock with a steepened viscous subshock where the $\nu_i \nabla u_i$ ion viscosity provides the remaining dissipation required by the RH jump conditions.

Another possibility, that exists outside of single fluid MHD, is the reflection of ions

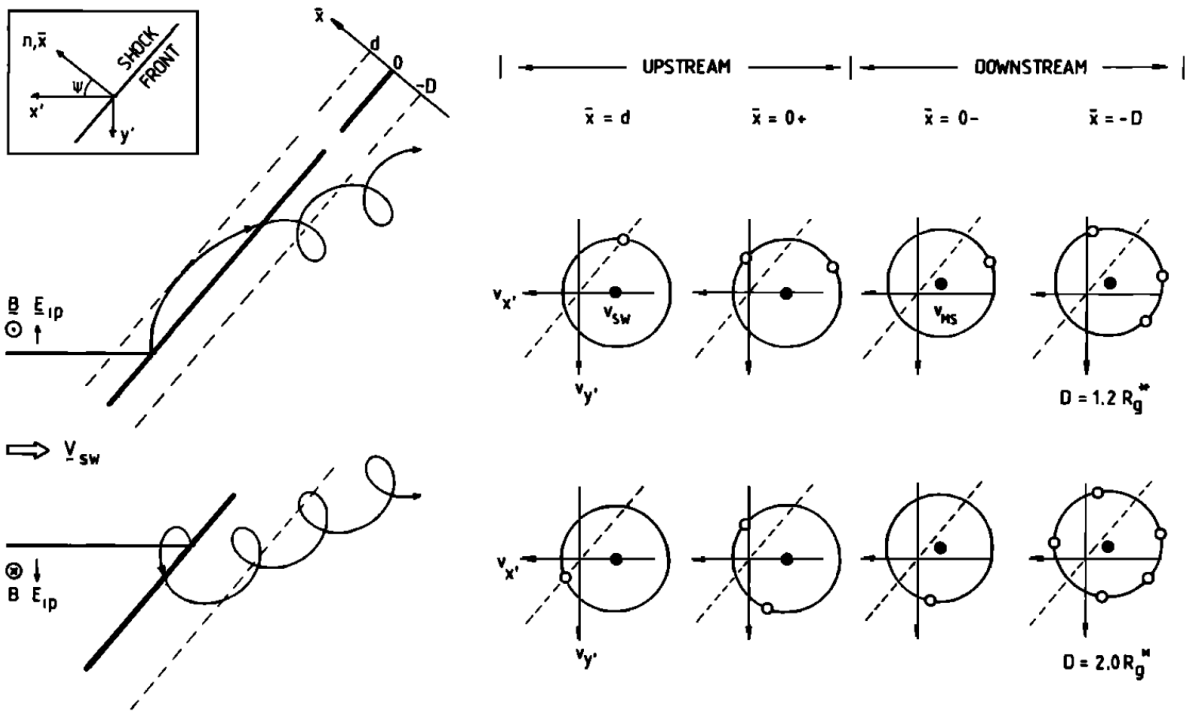

Figure 2.10: The trajectories of cold ions specularly reflected from a shock front. After they cross into the downstream, these ions gyrate about the mean flow in velocity space. This spatially varying non-gyrotropic distribution leads to magnetic overshoots and large downstream oscillations as the ions collisionlessly relax. Figure reproduced from Sckopke et al., 1983 [105]. This paper was also the first spacecraft observation of this non-Maxwellian downstream ion distribution.

from the shock layer. In this situation, a fraction of incoming ions (typically 10-25%) are reflected from a strong potential barrier at the shock layer. These ions gyrate around and re-encounter the layer, eventually crossing into the downstream but now carrying a substantially larger energy. While the immediate downstream distribution is no longer Maxwellian (or isotropic, or gyrotropic), the expectation is that the mean particle energy satistifies the continuity equations.

Specularly reflected ions make fluid descriptions difficult, as they introduce spatially dependent off-diagonal terms to the ion pressure tensor. Analytic attempts to include the complications of reflected ions into the shock jump conditions are vastly more complicated [29, 50]. Theoretical predictions have recently been very successful, as shown in Fig. 2.11. These agyrotropic ions have a position dependent pressure tensor, which must be balance by the magnetic pressure, and result in downstream waves [48].

To summarize, a single fluid MHD description is insufficient to capture reflected ion physics, which is observed in experiment, simulations, and spacecraft observations, and is

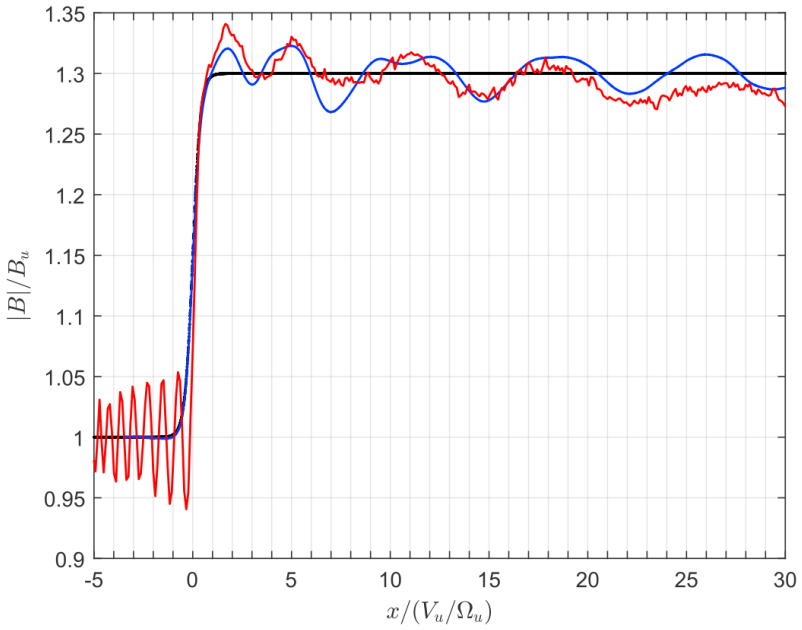

Figure 2.11: Spacecraft measurements of downstream fluctuations from collisionless ion relaxation. The red trace shows normalized magnetic field data from the THEMIS spacecraft of a low Mach number quasi-perpendicular shock, while the blue trace shows a numerical prediction of the same value with excellent agreement. This is evidence that reflected ions are present even for Mach numbers below M_c, which underscores the limitations of the single fluid MHD M_c prediction. The upstream fluctuations are likely oblique whistler waves, although that is not conclusively demonstrated in this case. Figure reproduced from Pope et al. 2019 [96]

fundamentally important to collisionless shocks.

2.5 Limits of MHD Theory and Hall Physics

MHD applies in the long wavelength limits where the scales of interest are much longer than an ion skin depth, $L \gg c/\omega_{pi}$. Yet in the MHD Shock derivation earlier, we presuppose the existence of an "infinitesimally thin" shock layer. Deviations from the predicted far up- and downstream states can clearly be seen in Fig. 2.4 and 2.11. Those looking to apply MHD shock theory generally just "zoom out" and look at the far downstream states which, after some relaxation process, should approach the predicted values[2].

MHD shock theory also relies on particle collisions to maintain Maxwellian distributions. The existence of collisionless shocks wasn't accepted until the mid-1960s; the review paper

[2]Unless energy has been radiated away from the shock in the form of waves, EM radiation, energetic particles, or other unanticipated phenomena.

by Sagdeev in 1966 acknowledging consequences of this holds up remarkably well [100]. Following Coroniti's suggestions to improve the single fluid theory, we first consider two fluid effects by writing separate momentum balance equations for each fluid species [53]:

$$n_\alpha m_\alpha \left(\frac{\partial \mathbf{u}_\alpha}{\partial t} + \mathbf{u}_\alpha \cdot \nabla \mathbf{u}_\alpha\right) = q_\alpha n_\alpha \left(\mathbf{E} + \mathbf{u}_\alpha \times \mathbf{B}\right) - \nabla \cdot \mathbf{P}_\alpha + \mathbf{R}_\alpha \tag{2.11}$$

where $\mathbf{R}_\alpha$ is the drag experienced by species α after collisions with all other species. The electron momentum balance equation can, by defining the fluid velocity $\mathbf{u}(m_e + m_i) = m_i \mathbf{u}_i + m_e \mathbf{u}_e \simeq m_i \mathbf{u}_i$, neglecting the miniscule electron mass, assuming quasineutrality $n_e = n_i = n$, representing $\mathbf{J} = en(\mathbf{u}_i - \mathbf{u}_e)$, and representing the drag as a resistive term $\mathbf{R}_e = \eta e n_e \mathbf{J}$, be transformed into what's known as the Generalized Ohm's Law [53]:

$$\mathbf{E} + \mathbf{u} \times \mathbf{B} = \eta \mathbf{J} + \frac{\mathbf{J} \times \mathbf{B}}{e n_e} - \frac{\nabla \cdot \mathbf{P}_e}{e n_e} \tag{2.12}$$

where the terms on the right are referred to as the resistive, Hall, and electron pressure terms. While the ion momentum balance equation must still be considered separately, this will be a very useful equation for analyzing dynamics that are slow on electron timescales (ω_{ce}^{-1} and ω_{pe}^{-1}). As the flows in plasma shocks are often far less than the electron thermal speed, this provides a simple fluid interpretation of shock phenomena.

This first suggestion of considering two-fluid effects will be very useful. Coroniti's second suggestion of including turbulence can be accomplished by using an anomalous resistivity due to field fluctuations. This will be discussed in a following section. Their final suggestions of including finite Larmor radius effects leads to very complicated analytic descriptions. This thesis will avoid this by instead considering ions in a mostly kinetic framework.

Those three modifications to single fluid MHD (two fluid effects, turbulence, and finite Larmor radius effects) still don't properly capture all of the dynamics in shocks. The other assumption in the earlier MHD Shock derivation is of a time independent or stationary shock structure. In 1989, Burgess first published simulations of quasi-parallel collisionless shocks displaying non-stationary behavior [13]. He hypothesized that, rather than be a discrete surface, quasi-parallel collisionless shocks might instead be "a constantly changing mosaic of shock surfaces embedded within the overall shock transition." This is sometimes referred to as the "pulsation shock" model.

Perpendicular shocks also routinely exhibit non-stationarity and cyclic reformation. In simulations, overshoots in the predicted density and magnetic field values are often correlated with non-stationary or reforming shocks [73, 72]. Spacecraft observations routinely

observe overshoots and that may indicate the ubiquity of perpendicular collisionless shock reformation, particularly in high Mach number shocks [75, 79]

In light of this, most modern computational shock simulations use either fluid-electrons with kinetic ions or fully kinetic particle-in-cell simulations. Chapter 3 will include a description of the Vector-Particle-In-Cell (VPIC) code that was used in analyzing the perpendicular experiment. While kinetic simulations are not some reduced model and technically include all of the physics, that doesn't always lead to increased understanding. Combining both techniques to use a Hall-MHD framework to interpret PIC results can be a useful method for understanding complex shock dynamics.

Hall-MHD Whistler Waves and Reflected Ions

Whistler waves can be directly derived from a linearization of the Generalized Ohm's law []. These mostly parallel propagating waves have a maximum group velocity of ~ 27 times the Alfvén speed (see Fig. 4.8). As such, these waves are capable of carrying energy away from very super-Alfvénic and/or very oblique shocks. Fig. 2.11 shows typical dispersive waves observed in the upstream of a $M_A = M_s = 1.2$, $\theta_{bn} = 71^\circ$ quasi-perpendicular shock. Whistler wave dispersion can limit the shock thickness, as its scale length is often much larger than any resistive scale length (following Coroniti's length scale argument). This will be discussed more in Chapter 4.

Whistler waves are particularly important because of their interaction with reflected ions. In the parallel shock configuration, it was realized that the anticipated shock heating should lead to a population of ions able to "evaporate" into the upstream [35]. Observations also show populations of cold specularly reflected ions amidst this hot background (see Fig. 2.16). These superthermal ions constitute the ion foreshock, which will be discussed in Section 2.8.

Without ion gyration returning the reflected ions to the layer, how then do these ions become part of the shocked downstream? Fig. 2.12 shows a result from a 1D PIC code run by M. Scholer in 2003. Here, a quasi-parallel, moderate Mach number shock reflects ions and launches whistler waves into the upstream. The interaction between those reflected ions and either incoming ions or whistler waves is key to the shock dissipation.

Previous simulations in similar geometries [87] explained the reflected ion and whistler wave interaction in terms of a resonant cyclotron process, as described by Gary in 1991 [47]:

$$\omega - \mathbf{k} \cdot \mathbf{v}_{\text{beam}} \pm m\omega_{ci} = 0 \tag{2.13}$$

That is, the doppler shifted cyclotron resonance between reflected ions and shock launched

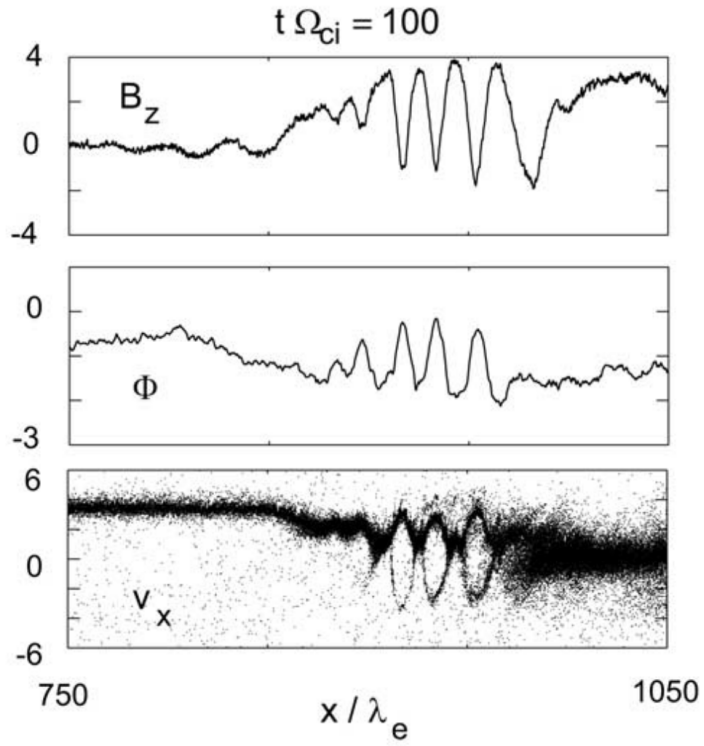

Figure 2.12: Results from a 1D PIC simulation originally by Biskamp [4] and reproduced by Scholer [102] of a $\theta_{bn} = 30°$ and $M_A = 4.7$ shock. Their interpretation is that the electric fields from shock-generated whistler waves trigger an ion-ion beam instability, leading to the rings in phase space and collisionless isotropization of the incoming ions. After several oscillations, these rings form a Maxwellian shocked downstream population.

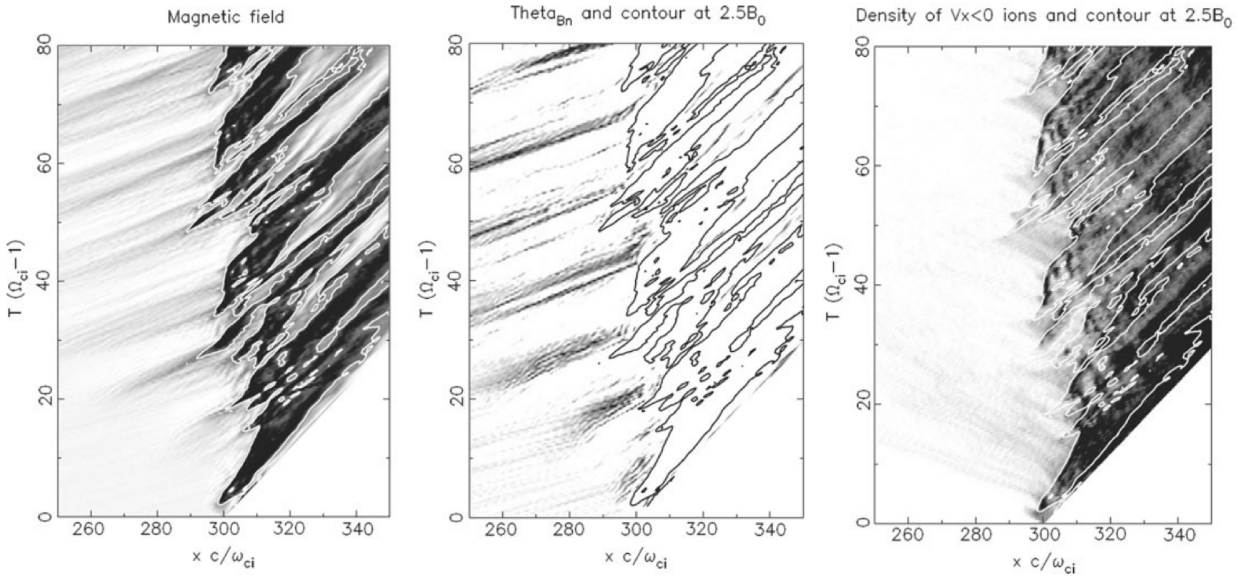

Figure 2.13: Results from a quasi-parallel ($\theta_{bn} = 30°$) hybrid shock simulation showing time evolution of magnetic field (white-black: $0.9B_0 - 3.5B_0$, contour at $2.5B_0$), the field orientation θ_{bn} (white-black: $30° - 5°$), and backstreaming ion density (white-black: $0.03n_0 - 2.0n_0$). Burgess calls attention to how the episodes of shock disruption are linked to regions of low θ_{bn} convected into the shock. Note how the backstreaming ions are trapped as the incoming waves grow to a critical threshold, discontinuously advancing the shock location forward [15, 14].

whistlers can scatter the ions and cause the whistlers to grow in amplitude. However, for the specific simulation in Fig. 2.12, Scholer interprets this not as a resonant interaction but as the non-linear two-ion beam instability first identified by Biskamp and Welter in 1972 [4]. The non-linear instability they describe is excited by the electric potential oscillations of the whistler. This shows remarkable similarities to the parallel shock experimental work.

A different example of whistler and reflected ion interaction is shown in Fig. 2.13, which shows a zoomed out view of the parallel shock reformation process. The shock front, which is held fixed in this reference frame, clearly undergoes a cyclic reformation process with a period of $\sim 20\omega_{ci}$. In this simulation, the waves are advecting into the shock, rather than dispersing from it. A different interaction between the waves and reflected ions can be seen here, and is not conclusively identified by the authors. However, the waves grow until some critical threshold where they begin trapping the backstreaming ions and form a shocked population.

Whatever the specific mechanism, the interaction between upstream/foreshock waves and reflected ions appears critical to parallel shock formation.

2.6 Anomalous Resistivity

Many attempts were made to preserve the elegant single fluid MHD shock results by invoking an "anomalous" resistivity. In this framework, an effective resistivity is provided by particles scattering off of large amplitude, short wavelength turbulence embedded in the shock layer. Such waves are generated by instabilities driven by the steep gradients present in the shock layer.

Some of the early thermonuclear theta-pinch experiments observed electric fields with fluctuating amplitudes of the order $\langle E^2 \rangle \geqslant 20\ (kV/cm)^2$ [69]. A good description of the origin of these fluctuations from the electron cyclotron drift instability is provided by Forslund et al. [45], while other experiments identified the source of these fluctuations as from an ion acoustic instability [31].

Regardless of the source, such strong fluctuations demanded calculations of the anomalous resistivity. From Tidman and Krall [112], a collisionless momentum sink term $e\langle \delta E \delta n \rangle$ can be included in the electron momentum equation, and then rewritten into the $\eta_{anom.}\mathbf{J}$ form.

However, the experimental work in this thesis observes no turbulent fluctuations, likely because the drive is substantially weaker than the several hundreds of kilovolts used in those thermonuclear experiments. In addition, the electron coulomb collision frequency remains high and should damp most instabilities. Recent work by S. Greess and the TREX

group appear to have identified 3D current driven instabilities in the reconnection layer [56]. Such instabilities might be present, particularly at higher drive voltages.

In our later analysis of the generalized Ohm's law, we will rely on traditional Spitzer resistivity as our only source of resistive dissipation [25].

2.7 The Shock-Piston Detachment Challenge

After a decade of the first theta pinch experimental work, it was recognized that forming a "canonical" laboratory shock of the type depicted in Fig. 2.2 is difficult. Davis in 1971 describes their theta pinch experimental results in very similar language as ours [31]:

> This is then a shock only in the simplest sense: the ions are reflected at a potential barrier set up by charge separation in the magnetic gradient, and stream out front at twice the piston velocity, while the electrons serve only to carry the necessary currents and to neutralize ionic charges. The electrons remain cold while the ion beam tends to "thermalize", as is shown by the appearance of the beam at the piston speed. ... The potential barrier has been observed by floating electric probes in hydrogen and reaches an amplitude sufficient to reflect the ions.

For a laboratory experiment to serve as a complete collisionless shock model, it was believed that the shock layer where the ion reflection is occuring should be at least one convective ion gyroradius away from the piston (in the perpendicular case) [88]. To capture downstream collisionless ion relaxation dynamics, tens of convective ion gyradii might be needed (see Fig. 2.11). In the parallel case, separation of one or more $\lambda_{\parallel}$ might indicate the dissipation mechanism is independent of the piston. Achieving these conditions is a substantial experimental challenge.

2.8 The Magnetospheric Bow Shock as a Case Study

The Earth's bow shock is by far the best studied collisionless shock. Good reviews of the bow shock include [71] and [15]. The goal of this section is not to rehash what is said better there, but to provide the bare minimum of context for the BRB experimental work.

The solar wind is a nearly collisionless plasma. At 1 A.U. it has nominal densities and temperatures of 1 cm^{-3} and 10 eV and a mean flow velocity of 400 km/s. The average solar wind particle undergoes the equivalent of one hard scattering Coulomb collision by the time it reaches the Earth. And yet, collisionless shocks are observed with thicknesses of

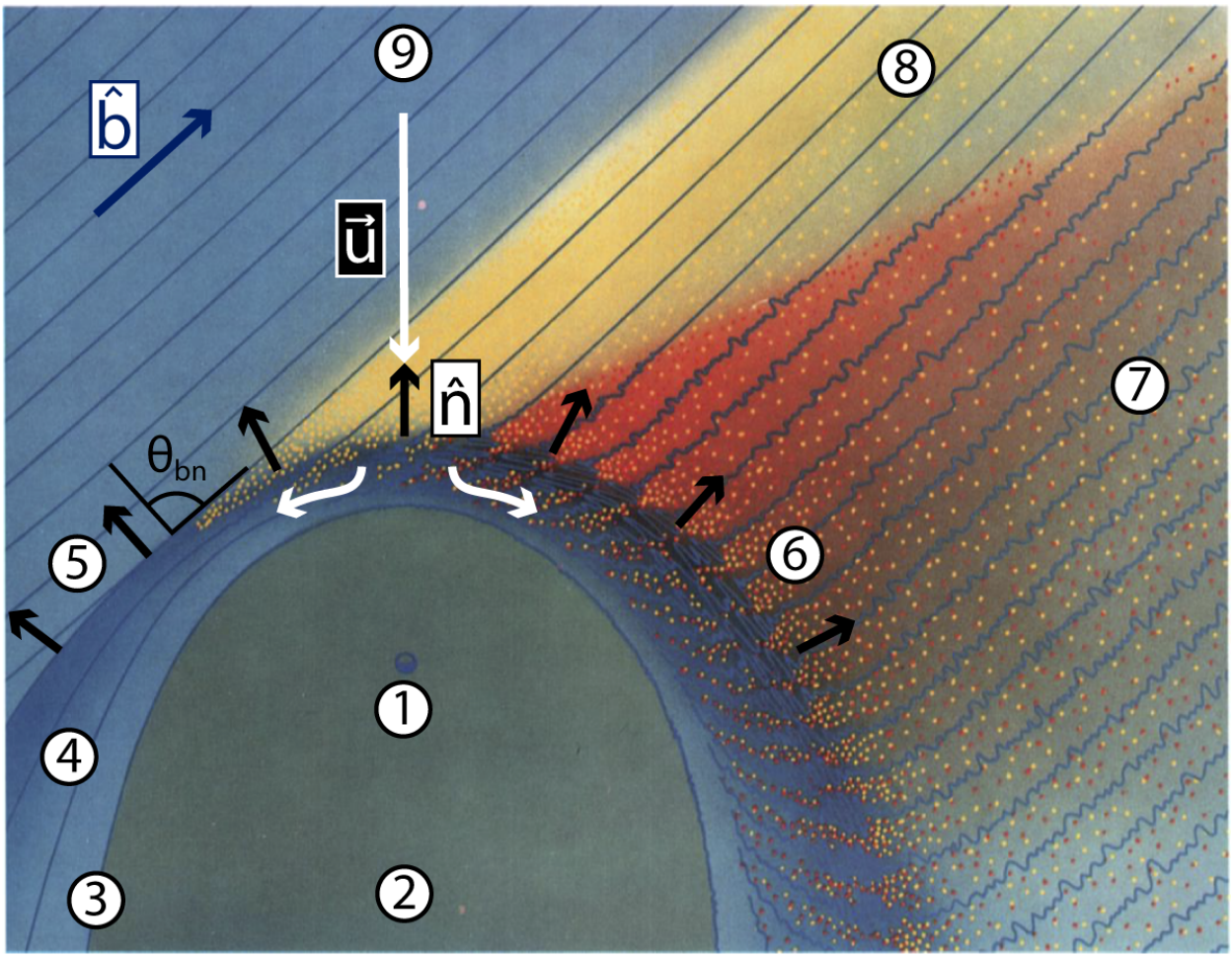

Figure 2.14: A cartoon diagram of the Earth's bowshock. The incoming solar wind with flow $\vec{u}$ and embedded magnetic field with direction $\hat{b}$ impinges on the shock layer with normal $\hat{n}$, and angle between the field and normal θ_{bn}. (1) the Earth, (2) the Magnetosphere, (3) the Magnetopause, (4) the magnetosheath, (5) the perpendicular bowshock, (6) the parallel bowshock, (7) the ion foreshock, (8) the electron foreshock, and (9) the unperturbed solar wind. Image reproduced from Tsurutani and Rodriguez, 1981 [113]

.

order 100 km in both the interplanetary solar wind and at the bow shock. This is roughly a factor of 10^6 smaller than the mean free path, so collisions are obviously an insufficient dissipation mechanisms.

Fig. 2.14 depicts the bow shock around the Earth produced as the solar wind collides with the magnetosphere. This system is very dynamic: the location of the shock and magnetosheath moves towards and away from the sun as it responds to changes in the solar wind ram pressure. The direction of the solar wind magnetic field changes with the location of the heliospheric current sheet. Sudden events like ICMEs (Interplanetary Coronal Mass Ejections) can drive the bow shock much closer to the Earth.

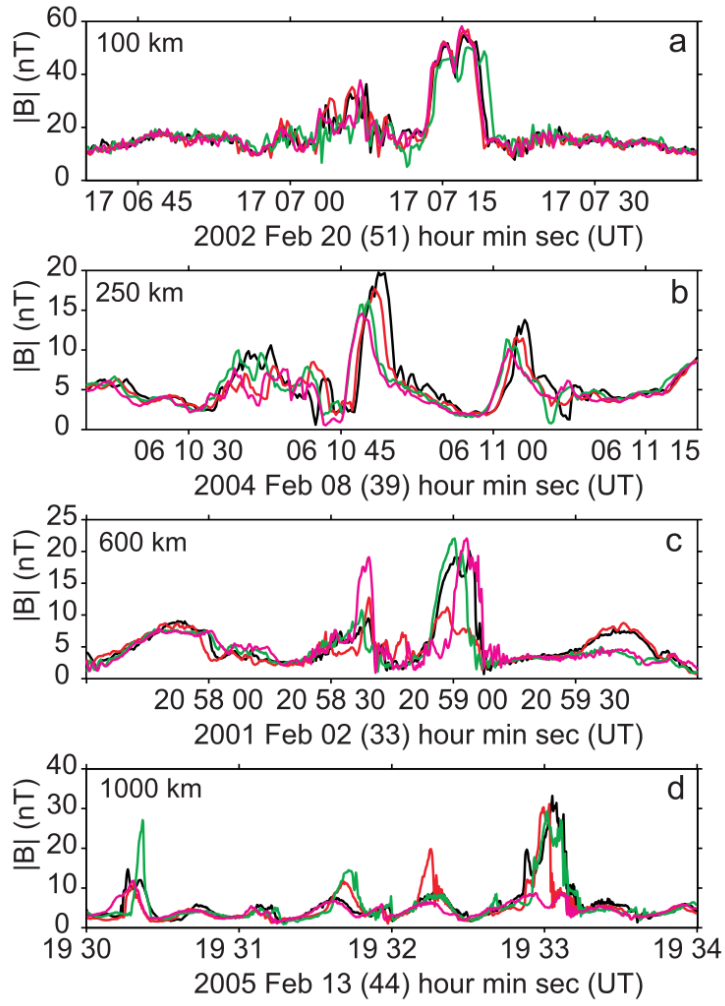

Figure 2.15: A series of observations from the CLUSTER spacecraft of SLAMS in the quasi parallel bow shock. For each of these events, the separation between spacecraft in the tetrahedral configuration is indicated in the upper left. The four colors represent the magnetic signals from each spacecraft, which begin to decorrelate on the 600 – 1000 km scale, indicating the approximate feature size. The unshocked solar wind plasma on either side of each SLAMS is evidence it is part of the extended parallel shock transition region. Figure reproduced from Lucek et al., 2008 [77].

The solar wind carries with it a magnetic field produced in the solar dynamo, drawn as thin blue lines in the picture. This provides a natural orientation to the system. At location (5) in Fig. 2.14, the magnetic field is perpendicular to the shock normal direction, while at location (6) the field is parallel. For intermediate angles, shocks are classified into quasiperpendicular ($\theta_{bn} > 45°$) and quasiparallel ($\theta_{bn} < 45°$). This classification is arbitrary and not always useful in predicting shock behavior.

The structure of the two regions is quite distinct. For strongly perpendicular bow shock events, the shock thickness is small, less than one upstream ion Larmor radius or about 100 km [ ]. This contrasts starkly with the quasi parallel bow shock, which is less of a discrete event, and more of a collection of many smaller pulsation events that convect downstream and merge to form a shock. The pulsation shock model described earlier was developed to explain the observed features [13]. The thickness of the parallel shock is around 100 times greater than the perpendicular case, or on the order of the Earth's radius.

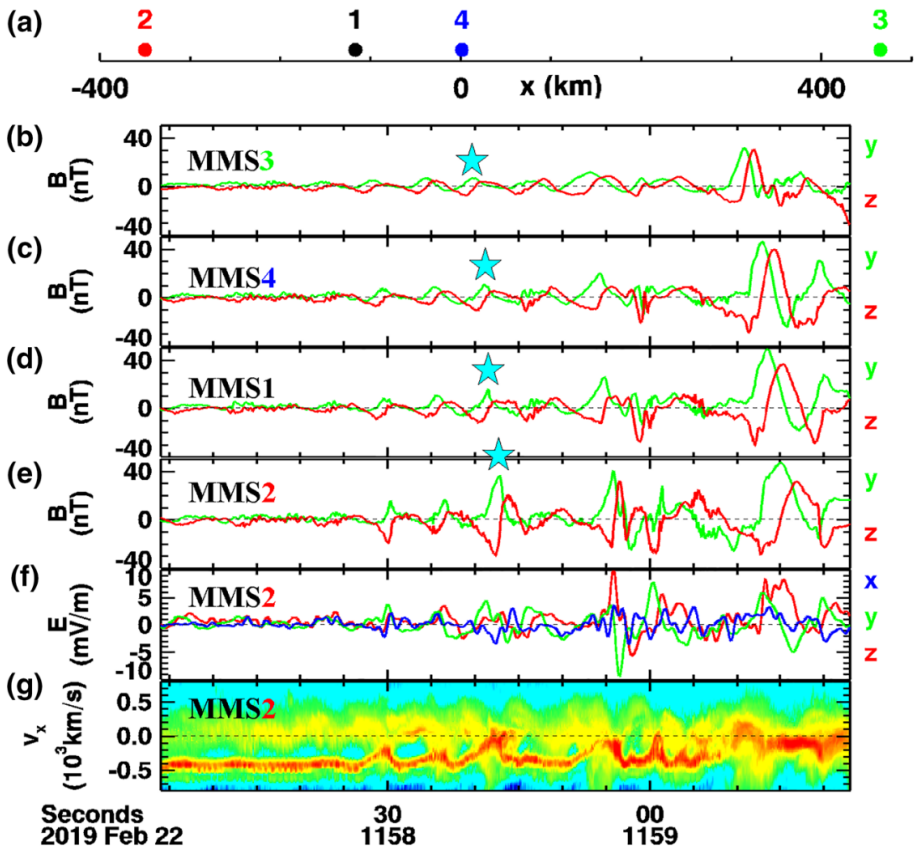

Figure 2.16: Data from the MMS spacecraft flying in a linear formation, with spacecraft separation shown in (a). The low amplitude whistler wave (top plot) grows under the influence of the counterstreaming ions (bottom) until by MMS2 it is a solitary large amplitude magnetic structure. Figure from Chen et al. 2020 [23].

What both of these systems share is the importance of reflected ions to the dissipation process. In the perpendicular case, a small fraction of incoming ions are reflected by the shock layer. As they re-encounter the layer and cross into the downstream, they form a heated ring distribution that together with the colder background approximately satisfy the MHD jump conditions.

In contrast, in the parallel case ions are reflected from somewhere in the shock and form a counterstreaming beam in the ion foreshock region. This beam interacts with ambient VLF (Very Low Frequency) whistler waves, causing them to grow into SLAMS [23]. Those SLAMS are convected back towards the shock, where they merge with other pulsations to collectively form the quasi-parallel bowshock.

Both of these statements are gross oversimplifications. They neglect the role that turbulent fluctuations play in isotropizing the ion distribution function, and ignore myriad other phenomena encountered in parallel shocks (shocklets, cyclic reformation, etc). These

descriptions are presented here because they represent the bare minimum of understanding of collisionless shocks necessary to interpret the BRB experimental results.

3 THETA PINCH EXPERIMENT

3.1 Intro

The first part of this chapter has been neatly lifted from a *PRL* paper [38]. The latter half is additional material supporting points casually mentioned or assumed in the paper.

3.2 Abstract

Supermagnetosonic perpendicular flows are magnetically driven by a large radius theta-pinch experiment. Fine spatial resolution and macroscopic coverage allow the full structure of the plasma-piston coupling to be resolved in laboratory experiment for the first time. A moving ambipolar potential is observed to reflect unmagnetized ions to twice the piston speed. Magnetized electrons balance the radial potential via Hall currents and generate signature quadrupolar magnetic fields. Electron heating in the reflected ion foot is adiabatic.

3.3 Motivation

Collisionless shocks are ubiquitous astrophysical phenomena, appearing in diffuse plasmas wherever flows exceed sonic and Alfvénic speeds. In the heliosphere, interplanetary shocks produce gradual solar energetic particle events, and near the Earth the magnetospheric bow shock helps determine our space weather [18, 16]. Such heliospheric shocks show wide variation in magnetosonic Mach number (M_{MS}) and in magnetic field orientation, which leads to a variety of dissipation mechanisms and complex kinetic physics [70]. Above a critical Mach number, ion reflection becomes a significant contributor to energy dissipation [36]. These reflected ions add a foot to the shock structure, which affects electron heating and influences the overall energy partition [22, 103].

In recent years, laboratory experiments using laser generated plasma have advanced our understanding of collisionless shocks. Experiments have shown shown evidence for counterstreaming instabilities and even first-order Fermi acceleration [98, 83, 89, 43]. Before high powered lasers were available, pulsed power experiments like the theta-pinch (θ-pinch) made collisionless flows using magnetic pistons. Many observations first made in θ-pinches were later made by spacecraft and simulations, including turbulent anomalous resistivity [91, 69, 107], specularly reflected ions [31, 90], and a critical Mach number for ion reflection [95, 74]. However, their short duration ($\tau_{exp} \leqslant \omega_{ci}^{-1}$) limited their relevance to shock formation processes rather than steady state dynamics [88]. Designed as thermonu-

clear experiments, θ-pinches generally did not operate with plasma beta ($\beta = 2\mu_0 nT/B^2$) above one and had limited diagnostic access [5, 92, 80].

Compared to prior pinches, the Big Red Ball (BRB) at the Wisconsin Plasma Physics Laboratory (WiPPL) can make measurements of high-β super-Alfvénic flows with unprecedented detail at the micro scale and simultaneous coverage of the mesoscale structure [44]. In this Letter, we present laboratory observations of weakly magnetized laminar flows in a θ-pinch with $\beta \sim 5$ and $M_{MS} \sim 3.6$. These 2D measurements reveal previously unseen features such as Hall magnetic fields, which are potentially important in reforming quasi-perpendicular shocks that are recently observed to be modulated by strong Alfvénic perturbations [67]. While the normalized system size ($R \sim \rho_i$), duration ($\tau_{exp} \sim \omega_{ci}^{-1}$), and turbulence levels are all vastly smaller than in space environments, this experiment studies basic dynamics in early shock development not easily investigated in situ by spacecraft. We make three observations that are new or significantly advanced compared to prior experimental work: First, we confirm that the initial penetration speed of the magnetic piston is governed by the reflected ion ram pressure and that these reflected ions lead to upstream adiabatic electron heating. Next, we identify quadrupolar out-of-plane magnetic fields generated by the reflected ion cross field current. Finally, analysis of the two-fluid terms in Ohm's law shows the current layer dynamics are governed by electron-MHD. These results show how, absent anomalous resistivity, Hall physics alone couples magnetic pistons to superalfvénic flows and begins shock formation.

3.4 Experimental Design

The experiment, shown in Fig. 3.1, consists of a large radius plasma column with a weak axial magnetic mirror field that is cylindrically compressed in a super-magnetosonic flow. An array of 18 washer guns (10 ms duration, 100 kW each [40]) produce plasma at the mirror throat which expands into the background field ($|B_{z0}| < 0.5$ mT, mirror ratio ~ 100). Midway through the discharge, four internal toroidal coils generate a fast-rising aligned axial field that compresses the plasma (pointing in the -$\hat{z}$ direction, rise time $\tau_{1/4} \sim 70$ μs) [85]. Measurements are made with a 5 MHz 16-tip Langmuir probe and linear arrays of 10 MHz 3-axis $\dot{B}$-coils, with resolution limited by their temporal resolution as the plasma flows past. For 100 km/s flows, they have spatial resolution of 2 and 1 cm, respectively. Both probes are jogged radially between shots, while stationary reference probes (labeled 'axial' and 'radial') align probe signals by measuring shot-to-shot variations. Subsequent experiments with toroidally spaced magnetic probes confirm good cylindrical symmetry.

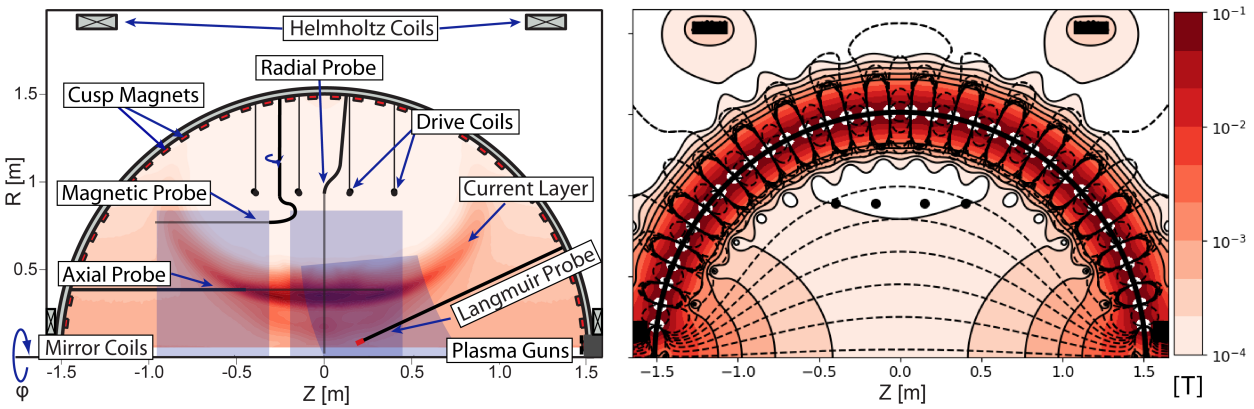

Figure 3.1: Experimental cross section. Blue shaded regions show the coverage of the Langmuir probe (wedge) and magnetic probes (rectangles). The red contour map qualitatively depicts the density during θ-pinch compression, with blue-dashes showing selected magnetic field lines. The four drive coils can be seen at R = 92 cm, Z = ±15, ±40 cm. Washer guns on axis supply the background plasma, which in the mirror configuration exhibits a relatively flat initial radial density profile.

3.5 Results and Analysis

The time dynamics of the implosion as reconstructed from over 200 shots are shown for a radial slice in Fig. 3.2. Between 10 and 16 μs, the current layer peak (dashed line) has an inward velocity of $v_l = 65$ km/s, given by its slope. The dotted line with slope $2v_l$ aligns with the leading density and temperature features. These two lines partition the experiment into four regions, which we define as the upstream, foot, current layer, and downstream, shown in the colored regions in Fig. 3.3. The layer and foot have M_{MS} of 3.6 and 7.2, respectively. Table 3.1 lists measurements and estimates of important scale lengths at the starred locations. While within the frame of the layer the mean free path for the upstream ions is large, within their own rest frame these ions are cold and collisional; this may damp turbulence within the layer.

The strong electric potential jump across the moving current layer reflects ions. The green line in Fig. 3.3 shows the steep rise in plasma potential at the layer. Ion reflection occurs as a result of the potential moving: in the layer reference frame moving at speed $-v_l$, incoming ions are reflected if their kinetic energy K_i is less than the jump in potential $\Delta\Phi_p$ across the layer. If $\Delta\Phi_p \geqslant 1/2 m_i v_l^2 = K_i$, then in the lab frame stationary ions experience a velocity change of $-2v_l$. Fig. 3.4 a) shows the measured linear relationship between the jump in plasma potential and the convected ion kinetic energy K_i for a variety of gases and drive voltages.

The experiment exhibits substantial ion reflection that regulates the speed of the piston.

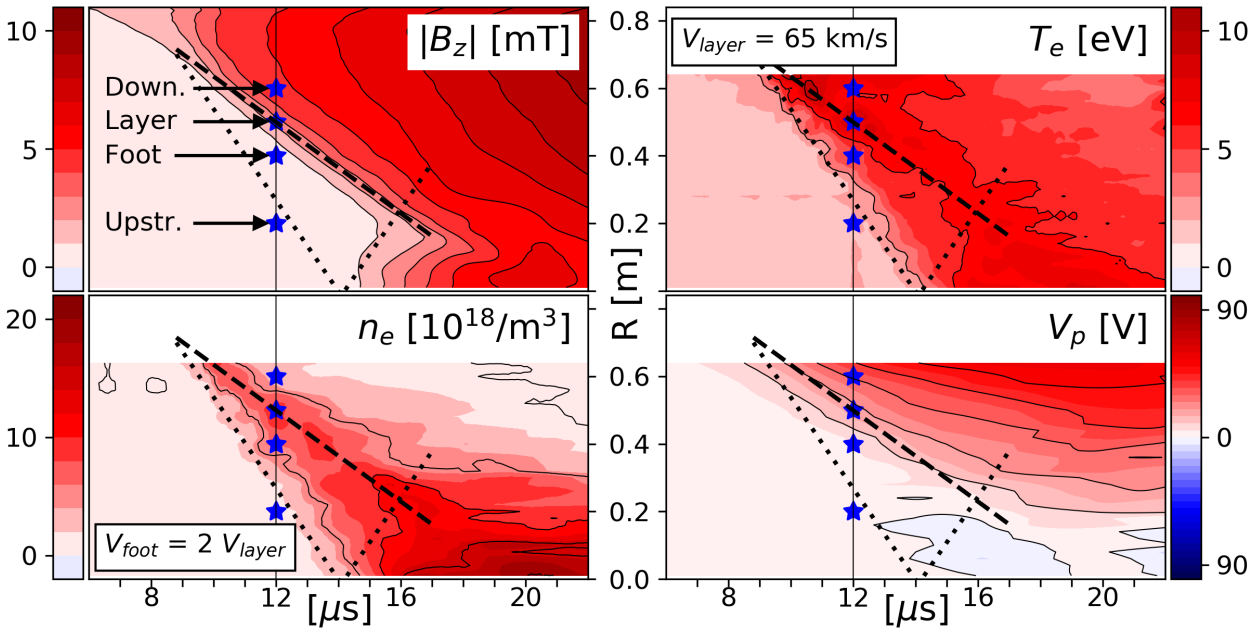

Figure 3.2: Magnetic and Langmuir probe measurements of radially imploding θ-pinch. This slice is taken at z=0.05 m, parallel to the "Radial Probe" in Fig. 3.1. The black dashed line is a linear fit to the peak of the toroidal current layer, with the dotted lines plotted for convenience at twice the speed. Note that the dotted lines border the earliest rise in density and temperature, and that the "reflection" through the axis aligns with an increase in B_z. Values from the starred locations are listed in Table 3.1, and data along the line at $t = 12$ μs are shown in Fig. 3.3. The radial electric field $E_r = -\nabla_r V_p$ is strongest along the current layer, as seen in Fig. 3.3. The drop in potential after 12 μs is a result of boundary conditions and electron heating in the foot, but does not affect E_r in the layer.

We use a 1-D pressure balance model to estimate both the layer speed and the reflected ion fraction α:

$$\frac{B_u^2}{2\mu_0} + (1+\alpha)\rho_0 v_l^2 + P_u = \frac{B_d^2}{2\mu_0} + P_d \tag{3.1}$$

Where subscripts u/d refer to the upstream/downstream [99, 3]. The total particle inventory below the layer is constant, suggesting that within measurement error α is one. Using values from Tab. 3.1 (and with ρ_0 at the layer location, r=0.5 m, where $n_0 = 1.0\ 10^{18}$ m^{-3}), Eq. 3.1 predicts a speed of 60±9 km/s, in agreement with the measured 65±5 km/s. Alternatively, solving Eq. 3.1 for α predicts $\alpha = 0.66 \pm 0.33$. Regardless if α is 0.66 or 1.0, Eq. 3.1 is dominated by the ram pressure term (95% of the LHS) and the downstream magnetic pressure (75% of the RHS). The nearly constant speed is due to the initial radial density gradient conveniently balancing the increasing strength of the magnetic piston, which grows from 4.0 to 6.0 mT from 10 - 16 μs.

An out-of-plane quadrupolar magnetic field is observed moving ahead of the layer in

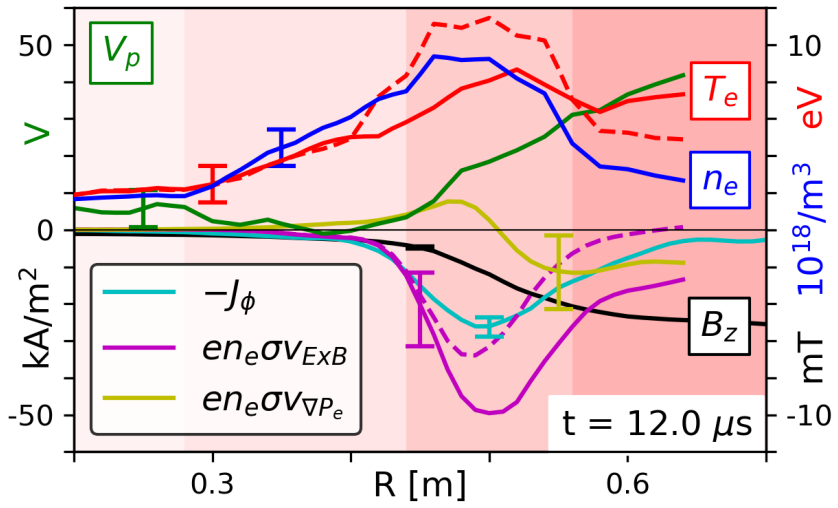

Figure 3.3: R-profile at z=0.05 m, t=12 μs showing n_e, T_e, and V_p from Langmuir measurements, and J_ϕ and B_z from magnetic measurements. Error bars show total error, not shot-to-shot uncertainty, which is small. The four colored areas left to right show the upstream, foot, layer, and downstream regions. The dashed red line is an adiabatic heating model, $T_e = T_{e0}(n_e/n_0)^{\gamma-1}$, for $\gamma = 2$. The factor $\sigma \equiv \omega_{ce}^2/(\nu_e^2 + \omega_{ce}^2)$ is an experimental parameter that accounts for collisional slowing [21]. The dashed magenta line estimates the sum current of the electron and ion E×B $\hat{\phi}$ drifts, which is zero in MHD. Within error, the measured toroidal current is the sum of the E×B $\hat{\phi}$ and electron diamagnetic drifts.

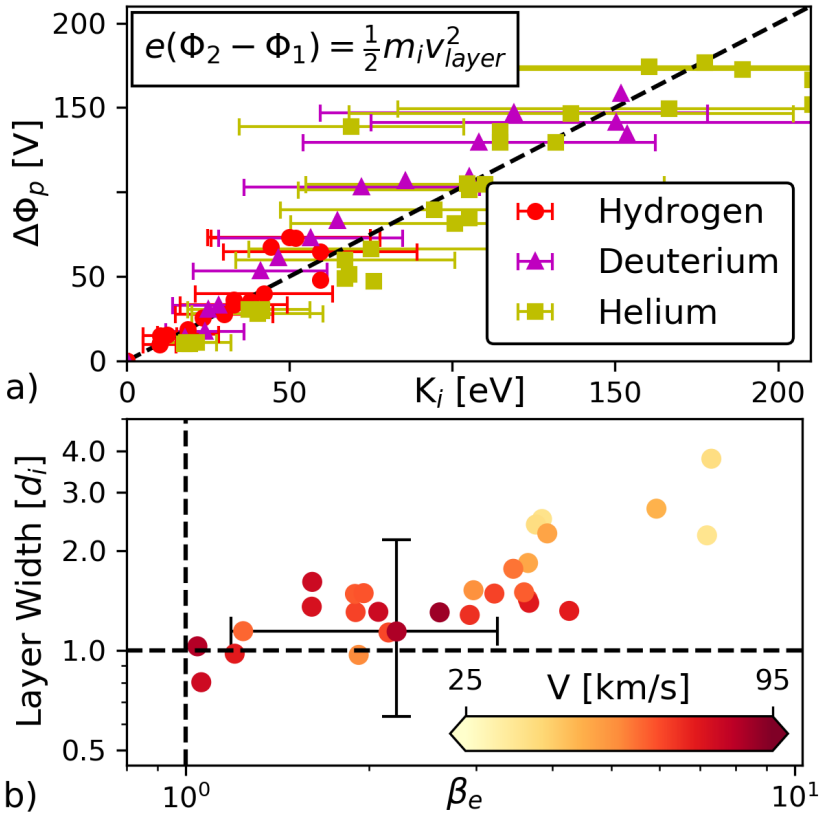

Figure 3.4: a) Plasma potential jump $\Delta\Phi_p$ vs convected ion kinetic energy $K_i = \frac{1}{2}m_i v_i^2$ showing a 1:1 relationship. $\Delta\Phi_p$ was measured a distance of $d_i/2$ on either side of the layer peak with both emissive and Langmuir probes. b) Current layer thickness against β_e in the current layer for a variety of drive strengths in H_2. As the magnetic piston becomes larger, the relative β_e decreases, leading to weaker ∇B drifts and a thinner current layer.

	Upstream	Foot	Layer	Downstream
T_e eV	2.0	5.0	8.0	6.7
n_e $10^{18}/m^3$	1.6	6.1	8.6	3.0
B_z mT	0.45	0.68	2.5	4.8
λ^e_{mfp} cm	5.1	8.4	15	30
$\rho_e = \frac{v_{the}}{\omega_{ce}}$ cm	1.1	1.3	0.4	0.2
λ^i_{mfp} cm	7	$> 10^3$	160	460
$\rho_i = \frac{v_i}{\omega_{ci}}$ cm	45	220	31	15
$d_i = \frac{c}{\omega_{pi}}$ cm	18	9.2	7.8	13

Table 3.1: Electron temperature, electron density, axial magnetic field, and important scale lengths at the four points in Fig. 3.2. Ion Larmor radii (ρ_i) and mean free paths ($\lambda^i_{mfp} = v_i/\nu_i$) are approximated using $v_i = (2T_e/m_i)^{1/2}$, $2v_l$, v_l, and v_l, respectively. The electrons are always magnetized but collisional on experimental timescales, with $\omega_{ce} > \nu_e > \tau^{-1}_{exp}$. In contrast, the reflected ions in the foot and layer are unmagnetized and collisionless, with $R_{exp} < \rho_i < \lambda^i_{mfp}$.

Fig. 3.5. The unmagnetized reflected ions ($\rho_i \sim 2$ m) freely cross the weak upstream field lines while the electrons ($\rho_e \sim 1$ cm) can not. To preserve quasineutrality, electrons from the current layer stream out to the wings of the experiment, cross field lines at some magnetic null, and then flow back to join the reflected ions. The red and blue arrows indicate the direction of these flows, which agree with the toroidal field polarity at (r,z)=(0.6,-0.8) m and quadrupolar character. Further scans in the axial direction reveal parallel electric fields localized to the density and temperature gradients at the edges of the foot near $z = \pm 0.4$ m. The net current is a result of electrons being trapped locally by the excess reflected ion charge, not by electric fields along the entire blue path.

Electron heating in the foot is strongly correlated with the density suggesting adiabatic heating. The dashed red line in Fig. 3.3 models $T_e \propto n_e^{\gamma-1}$, with $\gamma \simeq 2$ characteristic of magnetized electrons. In the layer the adiabatic model over-predicts the electron temperature, likely because of increased thermal losses to the wall cusp. This foot region adiabatic heating is consistent with the parallel electric fields observed along the axial density gradient, which preserve quasineutrality by confining the heated electrons.

The toroidal current layer dynamics are explained by an electron-MHD model. The generalized Ohm's law neglecting electron inertia can be written:

$$\mathbf{E} + \mathbf{v} \times \mathbf{B} = \eta \mathbf{J} + \frac{\mathbf{J} \times \mathbf{B}}{e n_e} - \frac{\nabla \cdot \mathbf{P_e}}{e n_e} \tag{3.2}$$

Assuming Spitzer resistivity η_s, the resistive term is everywhere small ($E_\phi > 100\,\eta_s J_\phi$) and can be neglected. Examining the radial components of Eq. 3.2, the relative contributions

of the J×B and ∇P_e terms can be estimated from electron E×B and diamagnetic drifts, as shown in Fig. 3.3. The E×B drift is largest and can provide all of the necessary current, but as the ions become magnetized in the sub-Alfvénic downstream the separate E×B drifts cancel any net current. The diamagnetic drift reverses direction at the pressure peak, first opposing and then reinforcing the E×B drift. This reduces the peak current density and widens the layer. Since $v_{\nabla P_e} \propto T_{e\perp}/B^2 \propto \beta_e/n_e$, as β_e decreases the total electron drift weakens and the current layer should thin. We observe this in Fig. 3.4 b), and expect it is generally true in laminar high-β super-critical flows.

3.6 Summary

With these observations, the θ-pinch dynamics can be explained as follows. The applied axial magnetic field induces via Faraday's law a toroidal electric field, beginning a radially inwards E×B electron drift. The resultant charge separation produces a radial electric field that drives a second E×B electron drift in the toroidal direction. This toroidal current is not limited by the weak resistivity and grows until the applied field is canceled. On ion inertial timescales, the radial electric field accelerates ions, moving the current layer inwards at a speed governed by the reflected ion ram pressure $(1+\alpha)\rho v_l^2$. Magnetized electrons move globally to preserve quasineutrality, leading to adiabatic electron heating in the foot. These hot electrons reduce the toroidal current density, broadening the layer beyond the one d_i expected for the $T_e = 0$ case. Finally, the on-axis rise in B_z at 14 μs is from a toroidal current of reflected ions, as suggested by the dotted line in Fig. 3.2. The Lorentz force on the reflected ions gently deflects their radial velocity ($\rho_i \sim 2$ m). Modeling of ion trajectories confirms most are deflected in the -$\hat{\phi}$ direction producing a substantial toroidal current.

In summary, we observe the interior and large-scale structure of a laminar super-Alfvénic θ-pinch piston. The short time scale precludes ion gyration back to the layer, and so the enhanced ion reflection is not forbidden by Rankine-Hugoniot considerations [36]. Any instability growth should be strongly damped by the electron collisionality, which is large compared to the inverse layer crossing time, $\nu_e \geqslant 20\,(d_i/v_l)^{-1}$. Furthermore, the relatively weak drifts of this experiment ($v_e \leqslant c_s$) are insufficient for the thin electron skin depth scale turbulent dissipation layers seen in prior pinches where $v_e \gg 10\,c_s$ [5, 69]. Without ion gyration or turbulent dissipation, the large ion reflection $\alpha = 66-100\%$ exceeds the $10-25\%$ commonly observed in space [105, 116]. Future measurements up to the electron plasma frequency will provide better estimates of the levels of turbulence present.

The Hall physics mechanism presented here may apply during the shock reformation process, especially when turbulence is weak or if ion reflection is high. This, and the curved

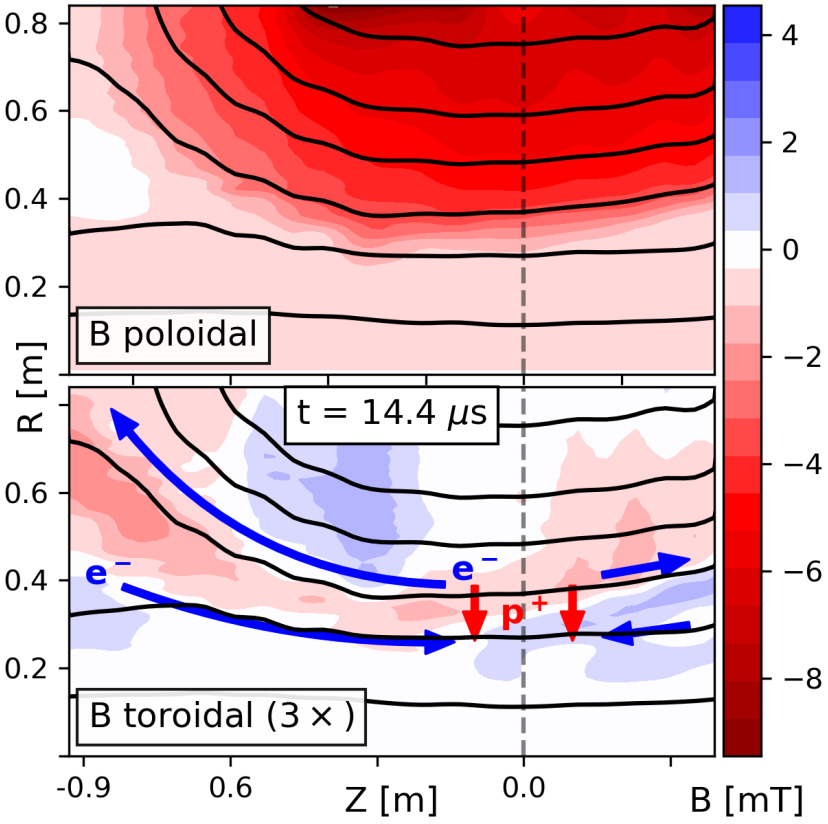

Figure 3.5: Profile of toroidal magnetic field with arrows indicating direction of electron and ion flows. The red lobe at $(z, r) = (-0.8, 0.5)$ m implies current in the clockwise direction, consistent with an electron flow needed to maintain $\nabla \cdot \mathbf{J} = 0$. The peak of the toroidal current layer is near the base of the red arrows. The axial density gradient from plasma injection at the $+\hat{z}$ north pole skews the quadrupole slightly to the south.

experimental geometry, makes it relevant to rippled perpendicular shocks, which were first predicted in simulations [76] and recently measured by spacecraft [67, 58]. As multi-spacecraft missions become more comprehensive, quadrupolar magnetic fields similar to this experiment may be useful for identifying nearby enhancements or focusing of reflected ions.

Further Discussion

The following sections expand upon statements briefly mentioned in the above published work or analysis that was not included in the final version.

3.7 Hall Physics Considerations

Let's compare the Spitzer resistivity $\eta_\perp$ with the toroidal electric field E_ϕ and the current J_ϕ. As a reminder, $\eta_\perp$ has only small dependence on density through the coulomb logarithm, which for these plasmas, we will use $\ln \Lambda \simeq 10$.

$$\eta_\perp = \frac{4\sqrt{2\pi}}{3} \frac{e^2 m_e^{1/2} \ln \Lambda}{(4\pi\epsilon_0)^2 T_e^{3/2}} = 1.03 \cdot 10^{-3}\ \Omega\text{m} \tag{3.3}$$

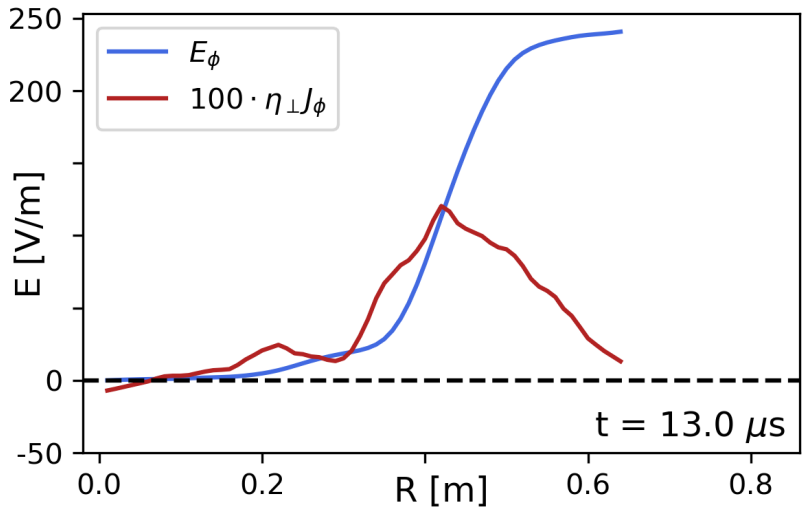

Figure 3.6: A comparison of the toroidal electric field and the resistive term in the electron momentum balance equation using the estimate Spitzer perpendicular resistivity. Note that the resistive term must be multiplied by a factor of 100 before it is comparable to the inductive electric field in either the foot or the layer.

This resistivity $\eta_\perp$ is distinct from the magnetic diffusivity η, which we used long ago when calculating r_m the magnetic reynolds scale length:

$$r_m = \frac{\eta}{V} = \frac{1}{\mu_0 \sigma_\perp V} = \frac{\eta_\perp}{\mu_0 V} = 5 \text{ mm} \tag{3.4}$$

We used this small size relative to the layer thickness to argue that resistivity is not the dissipation mechanism in the layer. We can also compare the expected toroidal current $\sigma_\perp E_\phi$ to the measured current. This is plotted below for a radial slice at t=13.0 μs. The $\eta_\perp J_\phi$ term has been scaled by a factor 100 to make it comparable. This discrepancy trigger the pursuit of anomalous resistivity by the first scientists investigating the theta pinch.

3.8 Adiabatic Electron Heating

When this data was first taken, the Langmuir probe fitting routine consistently overestimated the electron temperature. After some work to improve the accuracy by using a different fitting routine, the measured electron heating dropped dramatically. Now, peak electron temperatures are 10 eV, whereas before they were above 25 eV. Also, it is now apparent that there is a distinct correlation between the electron density and the electron temperature in the foot region. This is visible to some extent in figure 3.2 below the current layer:

We can also see this in an axial scan in figure 3.7. Here, regions in the foot connected by field lines show local heating of the electron temperature where the density increases. There is an obvious gradient in the electron temperature parallel to the magnetic field and density gradient.

Finally, figure 3.3 shows even more clearly the relationship, which exists up to the start of the current layer. The dashed curves labeled represents adiabatic heating of the background electron population, where the density and temperature are related by $T = n^{\gamma-1}$. This kind of heating is often seen in space plasmas with $\gamma = \frac{5}{3}$ obviously being characteristic adiabatic heating [106].

3.9 Expected Parallel Electric Fields

Let's imagine a particular flux tube in the experiment: mostly straight, length of 3 m and central field of 3 gauss sitting at a radius of 30 cm, bounded on either end by magnetic mirrors of 300 gauss. As ions stream across field lines and enter the middle of the flux tube, electrons must stream down from the poles to maintain quasineutrality. Whether these electrons enter the flux tube via jumping field line nulls in the cusp or from exposed grounded endcaps, we can remain agnostic.

This potential serves to draw in electrons to preserve quasineutrality and maintain this large density gradient along the fluxtube. The reflected ion population has a directed energy of 88 eV, and unless this parallel potential grows to some large fraction of that, this is what's driving the system. Let's give the background population some density n_0 and temperature T_0. The reflected ion density n_r increases the density in some region around the midplane, with the ϕ being the potential difference between the two regions. Let's also start with our collisional plasma (see below for estimates of electron collisionality) and assume Maxwellian distributions. Given a polytropic heating relationship, what magnitude of potential must grow to maintain this pressure gradient? Let's assume that the high parallel electron mobility ($v_{the} \sim 880$ km/s) ensures that this system rapidly reaches equilibrium, so we just need a potential to maintain constant electron fluxes between the two regions. At the left boundary, all rightward moving particles from the background fall down the potential well, and vice-versa at the right boundary. From the center, only particles with directed kinetic energy larger than the potential can escape. Thus, we can write a very simple particle flux balance equation.

$$n_0 \int_{-\infty}^{\infty} u f_0(u) du = (n_0 + n_r) \cdot 2 \int_{\sqrt{\frac{2e}{m}\phi}}^{\infty} u f_1(u) du \tag{3.5}$$

The left side, which represents the particles falling into the potential well, is trivially $n_0 v_{the}$. The right side represents all the particles with kinetic energy sufficient to escape

the potential well. The 1-D Maxwell-Boltzmann distribution f is

$$f(v_x)dv_x = \left(\frac{m}{2\pi T}\right)^{1/2} \exp\frac{-mv_x^2}{2T}dv_x \tag{3.6}$$

With our expression for T_1, we can write:

$$\frac{n_0}{n_0+n_r}\nu_{the} = 2\int_{\sqrt{\frac{2e}{m}\phi}}^{\infty}\left(\frac{m}{2\pi T_1}\right)^{1/2} v_x \exp\left\{\frac{-mv_x^2}{2(T_0+e\phi)}\right\}dv_x \tag{3.7}$$

Which evaluates nicely to:

$$T_1 \ln\left[\left(\frac{n_0}{n_0+n_r}\right)\sqrt{\pi}\sqrt{\frac{T_0}{T_1}}\right] = -e\phi \tag{3.8}$$

Substituting in for T_1:

$$T_0\left(\frac{n_0+n_r}{n_0}\right)^{\gamma-1} \ln\left[\left(\frac{n_0}{n_0+n_r}\right)^{\frac{\gamma+1}{2}}\sqrt{\pi}\right] = -e\phi \tag{3.9}$$

Using our values of $T_0 = 2$ eV, $n_0 = 1.6$, $n_r = 5$, we expect to see a potential of 6.7 V appear along the gradient. That is remarkably less than one might expect from assuming an equilibrium Boltzmann distribution using the upper temperature. It also happens to be in line with the measurements in figure 3.7. The potential that appears in the foot is at most 10 V above the background. Our model takes the compression ratio of 6 seen and estimates 12 V.

This model doesn't yet explain the measured hollow profile of the potential, seen in figure 3.7. The features in the foot density profile however are well understood by the cylindrical geometry and the spacing of the coils.

3.10 Collisional Heating Between Specularly Reflected Ions and Foot electrons

The theta-pinch launches a beam of specularly reflected ions moving at twice the speed of the imploding current layer. The most obvious question to ask is, are their collisions with background electrons significant? We can use a standard background temperature and density of 2 eV and $1 \cdot 10^{18}$ m^{-3}, and look at a beam of ions traveling at 130 km/s. The NRL formulary provides that the energy transfer rate between species goes as $\nu_\epsilon = 2\nu_s - \nu_\perp - \nu_\parallel$. 2 eV electrons ($v_the = 880$ km/s) remain much faster than 130 km/s ions, so lets use the

limiting forms for the above expressions where the test particle α (protons) is much slower than the field particle β (electrons). This chugs out to:

$$\nu_{\epsilon}^{i/e} = 1.2 * 10^4 \ s^-1 \tag{3.10}$$

Correspondingly, the energy transfer time is 83 μs, giving a heating rate on the order of 1 eV/μs. This assumes equal densities of streaming ions and background electrons, which is roughly the case since the streaming ions exceed the background density by a fair amount. . To be honest, this isn't too far off: we see the temperature in the foot jump 3 eV in <1 μs. Let's assume for now that its a strange coincidence.

3.11 Collisionality of Electrons

For this plasma, the lowest electron Larmor period is 0.1 μs (ρ_e ~1 cm), which is the same as a standard electron collision time for 2 eV. Any heating of the electrons lengthens the collision time (0.4 μs at 5 eV, 1 μs at 10 eV), and any addition of magnetic field shortens the larmor period, such that the electrons become magnetized ($\omega_{ce} \gg \nu_e$), but not fully collisionless ($\tau_e < \tau_{exp}$).

3.12 Resistive Heating of Electrons in Current Layer

Next step is to look at the electron heating in the current layer. Let's calculate the transverse Spitzer resistivity again using the NRL formulary and our experimental measurements in the foot.

$$\eta_\perp = 1.03 \cdot 10^{-2} Z \ \ln\Lambda \ T^{-3/2} \ \Omega \text{ cm} = 9 \cdot 10^{-5} \ \Omega \text{ m} \tag{3.11}$$

In our current layer, we have a peak current density of 25 kA/m^2, which we can use to calculate either the toroidal voltage drop due to resistivity, or the resistive heating power.

$$E_\phi = \eta_\perp J_\phi = \left(9 \cdot 10^{-5} \ \Omega \text{ m}\right)\left(25 \text{ kA/m}^2\right) = 0.4 \text{ V/m} \tag{3.12}$$

This is a trivial voltage drop when compared to the inductive toroidal electric field of 100 V/m. The heating power at 10 W/L is also trivial, and for the densities in the layer of 10^{19} m^{-3} suggests a particle heating rate of $6 \cdot 10^{-3}$ eV/μs. This weak resistivity is what triggered the initial search for anomalous resistivity. In this experiment, electron drift speeds in the layer appear to be below the ion thermal speed, suggesting that no mechanism for such a turbulent resistivity exists here.

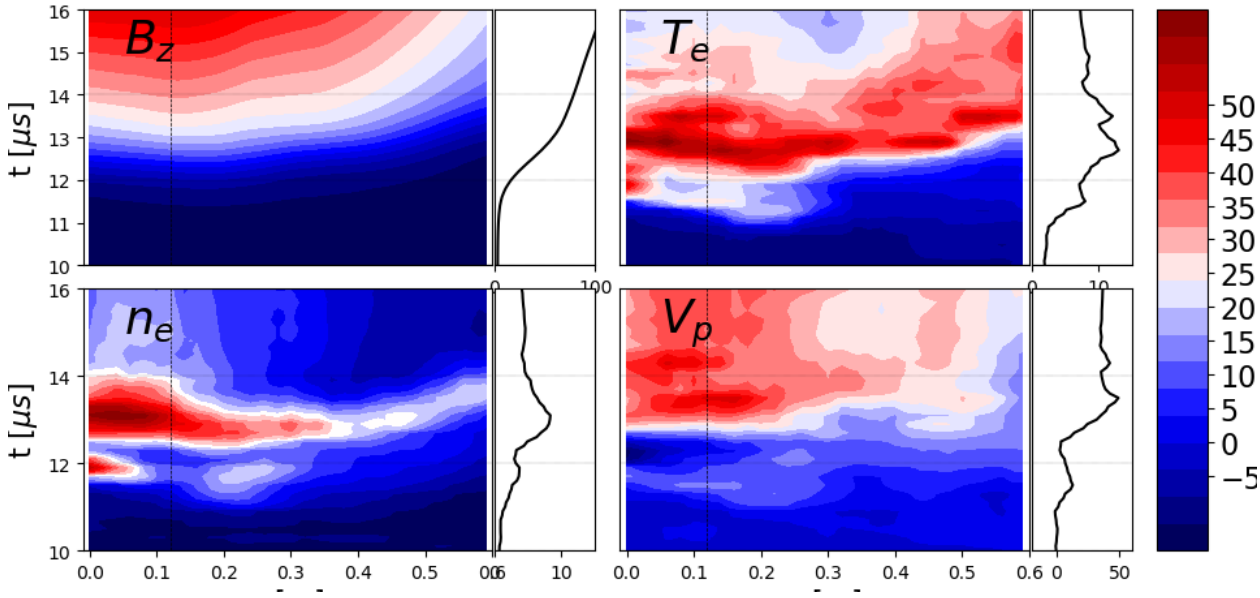

Figure 3.7: Results from a scan of the Langmuir probe in the axial direction for the standard theta pinch experiment, 0.5 mT at 4 kV drive voltage. The coils are at axial positions of 15 and 40 cm. The ripple in the drive due to the discrete coils is clearly seen by the enhanced reflected ion bunches at axial positions of 0 and 25 cm, centered between each pair of coils.

3.13 Ion Doppler Spectroscopy Measurements

This experiment benefited greatly from the extensive diagnostic expertise of the Madison Symmetric Torus (MST) experiment. Of particular help was D. Den Hartog, whose assistance enabled the use of ion doppler spectroscopy on the experiment. The IDS-1 system is a 1.0 M Czerny-Turner Duo-spectrometer long used on the MST [33]. As this thesis did not involve any substantial work to modify or improve this system, it will not be described here. Only the results of its use on the BRB will be presented.

It was hoped that spectroscopic observations of the reflected ion lines might provide a secondary confirmation of their existence. As ionized hydrogen has no emission lines, the operating gas was changed to Helium to observe the 4686 Åline. The results for a shot with a layer speed of 90 km/s is shown in Fig. 3.8.

The Duo-spectrometer takes two views through the plasma: one axial chord at R = 50 cm (left hand of Fig. 3.8) and one cylindrical radial chord at Z = 15 cm. The axial view begins showing emission as the layer crosses the view path. The radial view begins showing emission several microseconds earlier, as is expected. The radial view shows a hot Maxwellian distribution with $T_i = 180$ eV. This agrees well with the expected temperature of ions moving with the layer as they isotropize at the machine center, equivalent to a 92 km/s thermal speed.

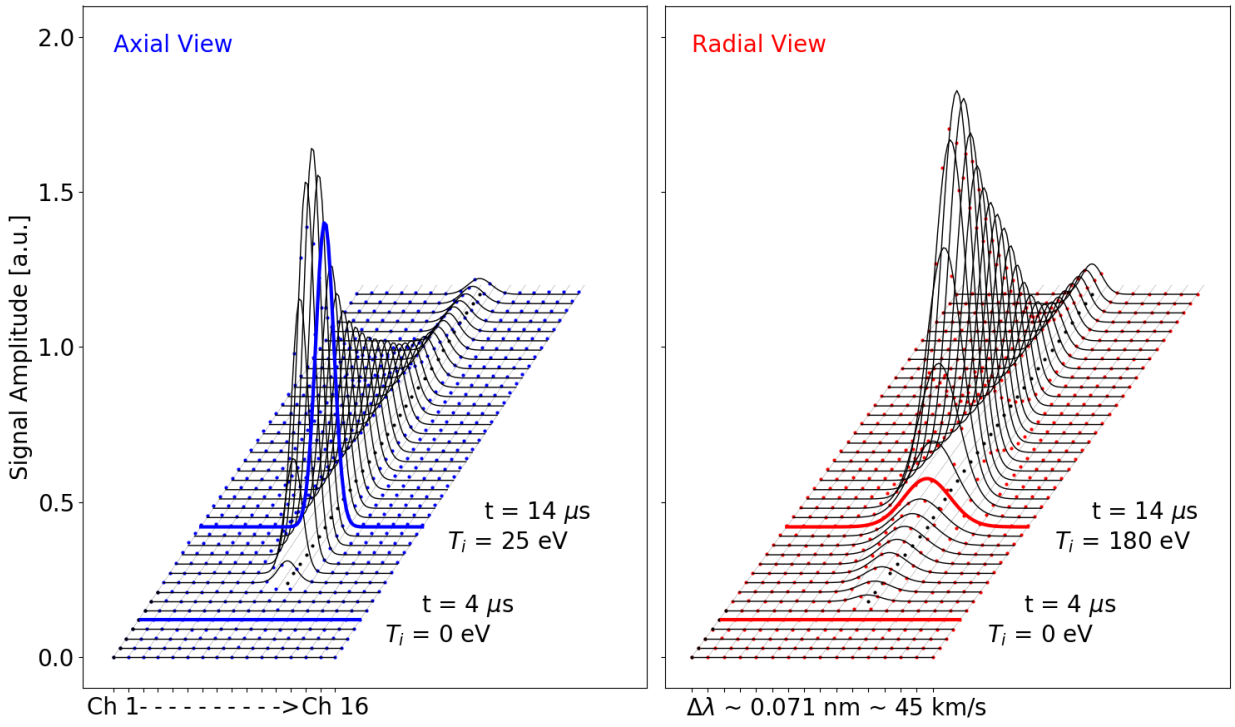

Figure 3.8: Ion Doppler Spectroscopy measurements of the experiment were made by examining the 4686 Åline from a Helium plasma. The axial view, left, was taken at R = 50 cm. It shows emission as the layer moves past the probe. The radial view at right shows an early hot temperature measurement before an extremely bright jump. The hot period is understood to be the layer penetrating inwards, while the brighter period is the stagnation at the center. The 180 eV temperature corresponds to the Helium layer speed, not the reflected ion foot. This is likely because the emission is dominated by the current layer region where the electrons are hottest.

It is believed that no reflected ions are observed here because the background electron temperature is too cold. Emission from the 4686 Åline requires hot electrons capable of exciting this state, generally visible after 12 eV. The background plasma, 2 - 5 eV, is far colder.

3.14 Background Field Measurements

It was a mistake in experimental design to not make Hall probe measurements of the target plasma magnetic field. The calculation of the target plasma magnetic field is the largest source of error in the experiment. To approximate the plasma diamagnetic effect and estimate a more accurate initial field, we will use the vacuum magnetic field and the Langmuir probe measurements.

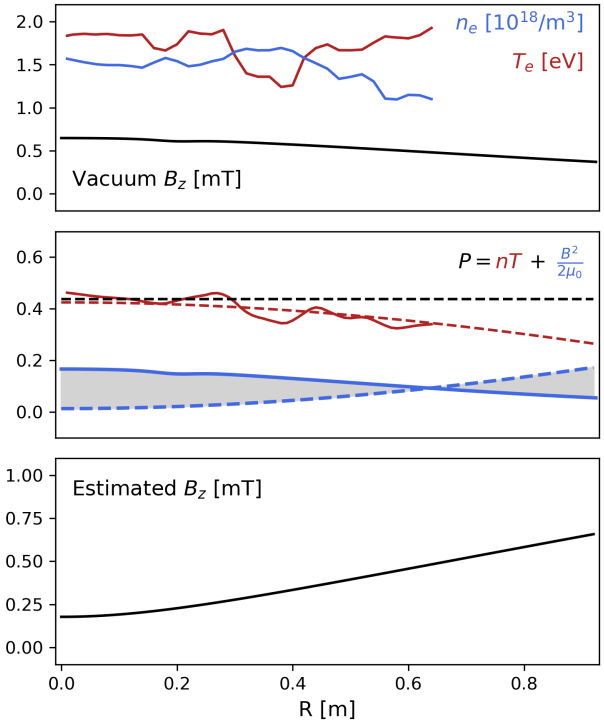

Figure 3.9: A demonstration of the naive compensation for lack of accurate magnetic field measurements. At top, Langmuir probe measurements of density and temperature next to vacuum magnetic field calculations, at z = 0.05 m. The middle plot uses those values to estimate a profile of electron plasma pressure (red dashed line). The solid blue line represents that vacuum magnetic energy density. The dashed blue line represents a solution to the equation $P = nT + B^2/2\mu_0 = \text{constant}$, under the constraint of conserved total magnetic flux. Here, the plasma diamagnetism rearranges magnetic pressure from the inner shaded region to the outer region. The estimated initial magnetic field at equilibrium is plotted at bottom.

Fig. 3.9 shows an attempt to estimate the initial field via pressure balance considerations. At the top, the initial measured profiles of density and temperature are shown. These are used to calculate the plasma pressure in the middle plot. The initial magnetic pressure using the vacuum fields from Fig. 3.18 is drawn with the blue line. The plasma pressure is balanced with the magnetic pressure under the constraint of constant total magnetic flux to produce a flat pressure profile, black dashed line. This yields the bottom plot, the estimated initial axial field, which is slightly reduced in the center from the 0.5 mT nominal value.

Collisionality Calculations

Up to this point, we have not shown conclusively that this is a collisionless shock. In this section I will outline how one estimates collisionality. The conclusion is that while the electrons are generally quite collisional, the reflected ions are solidly collisionless.

There is substantial recent experimental work on ion-ion interpenetration lengths in fast flowing jets. As done in Messer [82], Merritt [81], Byvank [17], we will calculate collisional slowing rates using the NRL formulary [64]. The slowing rate of species α on species β:

$$\nu_s^{\alpha/\beta} = \left(1 + \frac{m_\alpha}{m_\beta}\right)\psi(\chi^{\alpha/\beta})\nu_0^{\alpha/\beta} \tag{3.13}$$

Where the nominal slowing rate $\nu_0^{\alpha/\beta}$:

$$\nu_0^{\alpha/\beta} = 4\pi e_\alpha^2 e_\beta^2 \lambda_{\alpha\beta} \frac{n_\beta}{m_\alpha^2 v_\alpha^3} \tag{3.14}$$

and $\chi^{\alpha/\beta}$ is the normalized velocity:

$$\chi^{\alpha/\beta} = \frac{1/2 m_\beta v_\alpha^2}{k_b T_\beta} \tag{3.15}$$

Inserting the proton mass for m_β and 130 km/s for v_α yields $\chi = 44$, which is clearly in the fast test particle limit $\chi \gg 1$. Even for just particles moving at the layer speed, $\chi = 11 \gg 1$. Thus we use the fast limit slowing rate against background ions:

$$\nu_s^{i|i'} = n_{i'} Z^2 Z'^2 \lambda_{ii'} \left(9.0 \cdot 10^{-8}\right) \left(\frac{\mu + \mu'}{\mu\mu'}\right) \frac{\mu^{1/2}}{\epsilon^{3/2}} = \frac{2 n_{i'} \lambda_{ii'}}{\epsilon^{3/2}} \left(9.0 \cdot 10^{-8}\right) \tag{3.16}$$

This fast slowing rate can be used to find the stopping length L. From Eq. 19 in Messer [82]:

$$L = \int_0^u \frac{du'}{\nu_s^{ii'}(u')} = \frac{u_{rel}}{4\nu_s^{ii'}} \tag{3.17}$$

Where $\nu_s^{ii'}$ is the slowing rate in the fast limit given above, and the factor $1/4$ comes from integrating the u^{-3} dependence of $\nu_s^{i|i'}(u_{rel}) \propto \epsilon^{-3/2} = u_{rel}^{-3}$.

The slowing rate against background electrons (this time in the slow limit because the thermal electron speed far exceeds the relative flow speed, $v_{the} \sim 1000$km/s $\gg u_{rel} = 130$ km/s):

$$\nu_s^{i|e} = n_e Z^2 \lambda_{ie} \left(1.6 \cdot 10^{-9}\right) \mu^{-1} T_e^{-3/2} = n_e \lambda_{ie} \left(1.6 \cdot 10^{-9}\right) T_e^{-3/2} \tag{3.18}$$

Assuming ν_{ie} and $\nu_{ii'}$ are independent, they can be summed directly to give a total slowing rate and total stopping distance $L^* = u_{rel}/(\nu_s^{ie} + 4\nu_s^{ii'})$. We calculate the coulomb logarithm λ for the two cases above and find that λ_{ie} varies from 10 to 11 from the upstream to the layer, and $\lambda_{ii'}$ from 3.7 to 5.8 for ions streaming into the upstream, foot, and layer at 65 and 130 km/s. We will use the more conservative values for each.

In the following table we lay out more explicitly two cases. Here, n_i' is the density of the background/stationary ions only, while n_e is the total electron density in units of $10^{18}/m^3$.

Case	u_{rel}, km/s	n_i'	n_e	T_e, eV	$\nu_s^{ii'}$, kHz	ν_s^{ie}, kHz	L^*, m
1	130	1.0	6.1	5	1.3	10.	8.6
2	65	4.3	8.6	8	30	10.	0.5 m

Case 1 is relevant for the reflected ion beam slowing upon the background ions and

electrons. Case 2 is an upper estimate for ions in the layer, moving at the layer speed, assuming half of the background density is stationary. Case 2 is a crude and inaccurate assumption, but it demonstrates that even in the worst case, the ions can traverse the ~0.15 m layer without a collision.

Finally, the electron collision frequency is also higher than an inverse layer crossing time $\tau_l = d_i/v_{layer} = 450$ kHz. Estimating ν_e in the background, foot, and layer give values from 11 up to 15 MHz, which clearly satisfies $\nu_e \gg \tau_{cross}^{-1}$. The electron cyclotron frequency in the middle of the layer where $B = 2.5$ mT is far larger at $f_{ce} = 70$ MHz. The ordering for our electrons is then $\tau_{ce} \ll \tau_e \ll \tau_l$, and they are both magnetized and collisional on experimental scales.

Neutral Considerations

It is worth pausing to consider the role that neutrals might play in the experiment, and a zeroth order estimate of the electron-neutral collision frequency is a good starting point. Let's assume that we have a homogeneous background of neutrals, $n_0 \sim 1.6 \cdot 10^{18}$ m^{-3}, the same density as the on-axis density at the start of the experiment, or an ionization fraction of $1/2$. The approximate cross section of a neutral hydrogen atom is the cross sectional area of the Bohr radius, a_0. But in reality there is a temperature dependence to the cross section [41], which we will approximate as:

$$\sigma_s^{e/n} = 50(\pi a_0^2) \exp\left(-\frac{T_e}{2\ eV}\right) \tag{3.19}$$

Using the initial density and temperature, we can calculate the e-n scattering frequency:

$$\nu_{en} = n_n \sigma_s^{e/n} \left(\frac{T_e}{m_e}\right)^{1/2} 200 \text{ kHz} \tag{3.20}$$

Comparing to the plasma electron collision frequency (for stationary, quasi-neutral Maxwellian plasmas) [64]:

$$\nu_e = 2.9 \cdot 10^{-12}\ n_e\ \log\Lambda\ T_e^- 3/2 \simeq 16 \text{ MHz} \tag{3.21}$$

This is a comforting upper estimate for the electron-neutral collision frequency, as it remains far below the upstream ν_e. Given that the real ionization fraction is likely closer to 0.9 or greater, this suggests that neutral collisions might be safely ignored.

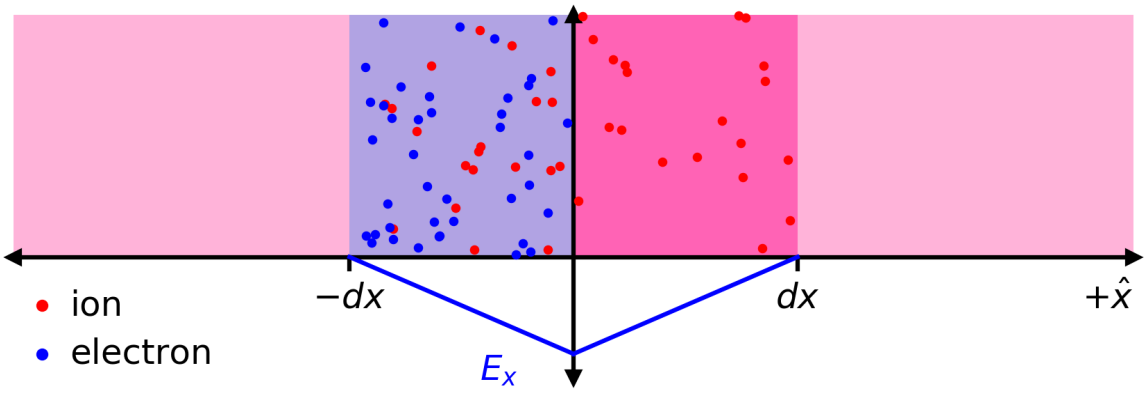

Figure 3.10: Cartoon representing the displacement of a slab of electrons of width dx and the resulting electric field.

Layer Thickness Theory

In hydromagnetic shock physics, there are three important dissipative scale lengths, as identified by Coroniti [26], which correspond to resistive (r_m), viscous (r_e), and thermal (r_t) length scales. The resistive and viscous dissipation lengths are defined as the lengths that make the magnetic and fluid Reynolds numbers equal to unity. Similarly, the thermal scale length is defined $r_t \equiv 1/\kappa_\perp u$, where $\kappa_\perp$ is the transverse thermal conductivity. We can estimate those lengths for nominal BRB pinch plasmas of $2.0{\cdot}10^{18}$ m^{-3}, 2 eV, 0.5 mT, and 6 cm/s flow speeds u. Beginning with the resistivity η, defined as the inverse of the conductivity σ:

$$\eta = \frac{1}{\mu_0 \sigma} = \frac{m_e \nu_e}{m u_0 n_e e^2} \nu_e = 2.91 \cdot 10^{-6}\, n_e \log \Lambda T^{-3/2} s^{-1} \tag{3.22}$$

And using a simple definition of the electron collision frequency:

$$\nu_e = 2.91 \cdot 10^{-6} n_e \ln \Lambda T_e^{-3/2}\ s^{-1} \tag{3.23}$$

We can make a quick estimate of the resistive dissipation scale length:

$$r_m = \frac{\eta_\perp}{u} = \frac{300\ m^2 s^{-1}}{6.0 \cdot 10^4 m s^{-1}} = 4.6\ mm \tag{3.24}$$

One way to interpret this result is that, were resistivity the dominant dissipation mechanism in the shock, the layer would thin down to 5 mm until the current density is large enough to provide the necessary dissipation.

The transverse ion viscosity η_0^i depends strongly upon the ion temperature, being propor-

tional to $T_i^{5/2}$:

$$\eta_0^i = 0.96 \cdot 10^{-6}\, n_i T_i \tau_i = 0.96 \cdot 10^{-6} n_i T_i \left(2.09 \cdot 10^{15} \frac{T_i^{3/2}}{n \ln \Lambda} \mu_i^{1/2}\right) \text{[s]} \tag{3.25}$$

In high Mach number plasmas, this approximation for the ion collision frequency and ion viscosity is not accurate. A better treatment assumes a hydrogen test particle with energy given by our layer speed ($\epsilon = \frac{1}{2}\, m_i\, (6.5\ \text{cm}/\mu\text{s})^2/ = 22$ eV), and background particles with the upstream temperature $T_i = 2$ eV. The slowing down rate for cases where $\epsilon \gg T_i$, given in [64]:

$$\nu_s^{i/i} = 9.0 \cdot 10^{-14}\, n_i \ln \Lambda \epsilon^{-3/2} = 2 \cdot 10^4\ \text{s}^{-1} \tag{3.26}$$

Where the Coulomb logarithm $\ln \Lambda$ uses the appropriate form for counterstreaming ions in hot electrons background ($T_e \sim 10$ eV) and is about 12. The viscous scale length then becomes:

$$r_e = \frac{\eta_0^i}{\rho u} = 0.96 \cdot 10^{-6} \frac{T_i \tau_i}{m_i u} = 0.1 - 1.5\ \mu\text{m} \tag{3.27}$$

where ρ has been added to convert from dynamic to kinematic viscosity and give units of diffusion, m^2/s. As in the resistive case, this says that the layer would have to thin down to $\tilde{1}$ μm until the velocity gradients were strong enough that ion viscosity could provide the shock dissipation. The conclusion for the transverse electron thermal conductivity is similar.

$$r_{th} = \sqrt{\frac{u}{\kappa_\perp}} = \frac{\omega_{ce}}{\nu_e} \sqrt{\frac{m_e \nu_e}{4.7 \cdot 10^{-6}\, n_e T_e u}} = 2.8\ \mu\text{m} \tag{3.28}$$

Where here the dissipation scale length has been squared on dimensional analysis considerations. But as Coroniti mentions, thermal dissipation can only be the primary dissipation mechanism in weak ($M\tilde{1}$) Fast or Slow mode MHD shocks. And so for the strong (M>2) Fast mode perpendicular shocks of the pinch, we don't expect to see this mechanism.

None of this is likely to be relevant in the experimental pinch, as a Hall physics solution to the continuity equations appears at ion skin depth scales, much larger than even the resistive scale length.

Let's review first the derivation of the electron plasma frequency, which imagines a slab of electrons of thickness dx being displaced a distance dx in an infinite homogenous plasma. The electrons leave a hole of positive charge behind, and an electric field that grows to a max value at the interface of the two slabs, and falls to zero at the edges:

$$E_x = \frac{-e n_e}{\epsilon_0} \left(dx - |x|\right) \tag{3.29}$$

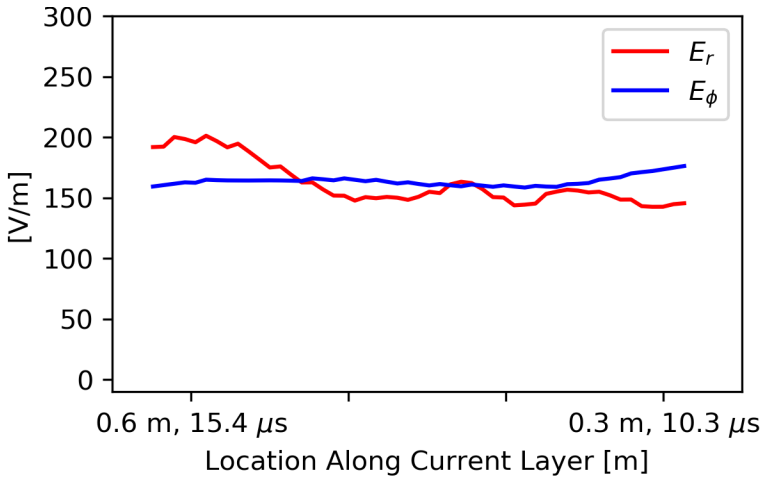

Figure 3.11: Experimentally measured values of the radial and toroidal electric fields measured along the peak of the theta pinch current layer. This was a surprising experimental result at the time, which in hindsight is a banal plasma response.

For an electron oscillating about the interface, we can set the acceleration equal to the Lorentz force per unit mass:

$$\ddot{x} = \frac{n_e e^2}{\epsilon_0 m_e} x \tag{3.30}$$

Which yields the harmonic oscillator solution of $\omega_{pe}^2 = \frac{n_e e^2}{\epsilon_0 m_e}$ and defines the electron plasma frequency ω_{pe} as well as the electron skin depth $d_e \equiv c/\omega_{pe}$.

Let's finally make an estimate of the actual current layer thickness. As shown earlier, the ram pressure balance with the magnetic field is what dictates the penetration speed of the current layer, with $2\rho u^2 = B^2/2\mu_0$. Using the estimate that $E_r \sim E_\phi$ (elaborated below), the radial component of the Lorentz force on an ion becomes:

$$m\ddot{x} = eE_r = eB_z u_r \tag{3.31}$$

$$\ddot{x} = 2e\sqrt{\mu_0 n_i m_i} u^2 = 2\frac{u^2}{c}\sqrt{\frac{n_i e^2}{m_i \epsilon_0}} = \frac{2}{d_i} u^2 \tag{3.32}$$

And so for a layer thickness of Δ, a moving ion entering the layer (or a stationary ion entering the moving layer) and experiencing constant acceleration will come to a halt when:

$$\Delta = \frac{u^2}{2a} = \frac{u^2}{2(\frac{2}{d_i} u^2)} = d_i \tag{3.33}$$

Thus for this pinch with unmagnetized ions and total ion reflection, we expect the current layer Δ to thin down to approximately the ion skin depth.

Why should the estimate of $E_r \sim E_\phi$ be a valid assumption? In ideal, collisionless electron MHD, $E = v_e \times B$. For cylindrical symmetry, the two components $\hat{r}$ and $\hat{\phi}$ depends on the same axial B_z and respective v_ϕ and v_r terms. While those terms refer to the drift

motion across field lines, they both are in the $\perp$-direction, and thus from a single particle perspective are equivalent. In the experiment, this turns out to be a rather fine assumption, as seen in Fig. 3.11. The radial electric field was calculated from the radial gradient of the measured plasma potential, while the toroidal inductive field was calculated from the loop voltage equal to the time derivative of the flux function, $d\Psi/dt/2\pi r$.

In the BRB theta pinch, no current layers thinner than $\sim 1 d_i$ were observed. This is in strong contrast to prior experiments that observed anomalous resistive current layers as thin as $3\, c/\omega_{pe}$. [] This is because they often had fully magnetized ions ($\rho_i \ll L_{exp}$), and were strongly driven, with large drift velocities that generated ion sound and lower hybrid turbulence. [] Here the current layer thickness is determined not just by the $E \times B$ drift and the ion inertia, but also by the electron pressure. Fig 3.4(b) reflects the fact that the grad-B single particle drift depends linearly on $T_{e\perp}$:

$$v_{\nabla B} = -\frac{T_{e\perp}}{q}\frac{\nabla B \times \hat{b}}{B^2} \tag{3.34}$$

3.15 Vector-Particle-In-Cell Simulation Work

Alongside the TREX collaboration with Bill Daughton's group at Los Alamos National Laboratory (LANL), I began simulating the theta pinch experiment. In 2017, Samuel Greess and I traveled to the lab for the first time to receive instructions from Adam Stanier in how to run a modified cylindrical version of VPIC, the Vector Particle In Cell code, on the LANL supercomputers. This work was successful in both replicating several experimental features, and in guiding the direction of the experimental work. While Sam productively continued the TREX simulations, after two years my theta pinch simulations were largely halted as experimental work on the BRB increased. The following gives a cursory overview of VPIC, meaningful results, and ways to progress further.

VPICs largest advantage over standard PIC simulations lies not in the algorithms which iterate over Maxwell's equations but in the computational architecture. VPIC scales to massive parallel computations, and its ingenuity lies in the "vector" structures that improve performance by minimizing manipulation of the data [9, 10]. Optimization of the code relies on balancing the demands on individual processors with the demands of passing information between processors: in short, one wants simulation domains to be small so that each processor has a reasonable and similar number of particles, but also needs domains to be large so that particles aren't often passed between processors. This passing of particles between domains can be particularly time intensive as those processors may be located far

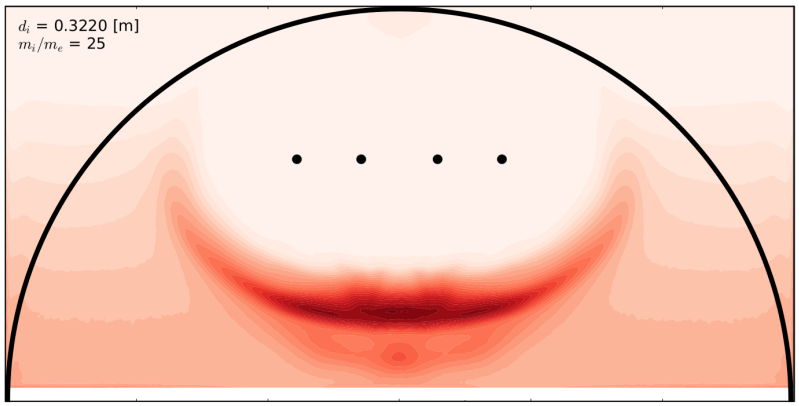

Figure 3.12: Plot from an early theta pinch simulation whose purpose was to initialize an MHD stable initial profile. This stability is necessary to prevent launching Alfvén waves as the simulation begins. The initial density profile satisfied $J \times B = \nabla P$, assuming constant $T_e = T_i = 5$ eV, a nominal density of $1 \cdot 10^{18}$ m^{-3} and field of 0.5 mT. The black line marks the edge of the BRB vessel, but was not used in the simulation. Later simulations did include a conducting shell.

away from each other in the physical architecture of the supercomputer.

The cylindrical-VPIC adds extra challenges to these two demands. Rather than all cells being equal size, cells with the same toroidal dimension ϕ at lower radii have a much smaller size. In order to properly resolve Maxwell's equations, the simulation timestep dt needs to be smaller than the smallest cell size $\delta = r\phi$ divided by the speed of light c. This is known generally as the Courant condition. Unfortunately, this requires that as the cylindrical radius goes to 0, so to does dt, and the computation expense increases drastically. The easiest solution is to simply cut your losses and limit the computational domain to some small but finite r. As seen in Fig. 3.12, for these simulations the lower bound was set at 5 cm.

Properly initializing the experiment is the next challenge for a VPIC user. It is important to begin with a configuration that it both MHD stable and experimentally relevant. If, for example, an initial density profile was chosen without regard for the magnetic field profile, strong Alfvén waves would be launched at the start of the simulation as the system begins relaxing towards an equilibrium state. Fig. 3.12 shows the electron density profile from an initial attempt. Here the domain is a rectangular torus shown, and the black line representing the BRB wall is added only for comparison. One can see that while the experiment is happening in the center, at the edges of the box there are Alfvén waves propagating inwards, visible as fluctuations in the density contours. For these strongly

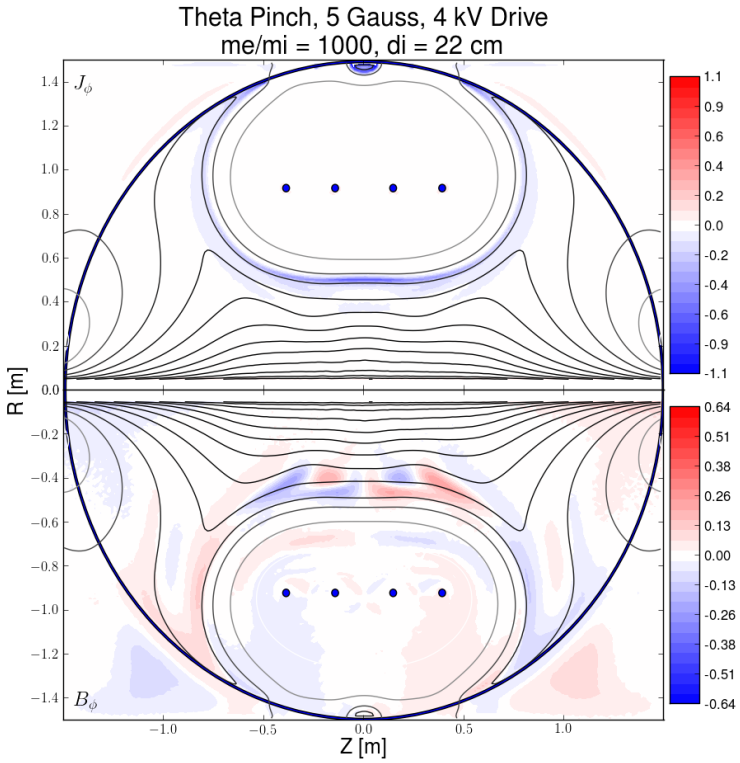

Figure 3.13: Results from a nearly realistic simulation, with initial density and mirror profile as in the experiment and an almost realistic mass ratios. Above shows the toroidal current while below shows the toroidal magnetic field. The current layer thickness (0.10 m) is somewhat thinner than in the actual experiment (0.20 m). The quadrupolar Hall magnetic field structure has more detail of the jets launched between the coils than could be resolved in the experiment.

super-Alfvénic shock experiments, the simulation can conclude before such waves reach the region of interest, and are thus relatively unimportant.

While such waves might not be important on experimental timescales, achieving an experimentally relevant configuration still is. Fig. 3.13 shows the results from a later experiment. Here, realistic fields from the mirror and Helmholtz coils are used. A conducting shell and particle sink boundary representing the vessel wall was used. The vessel magnetic cusp was not included. The simulation was initialized with an unrealistic but computationally simple radial density profile, and then run for several ω_{ci}^{-1} so that particles not trapped in the mirror were lost to the walls. When the profile reached a steady state that resembled the initial experimental configuration, that was then saved as a checkpoint to be used for the starting point of simulations with different drive voltages.

Fig. 3.13 shows the result near the end of the simulation of the current and magnetic fields for the most experimentally relevant parameters run. Note that the mass ratio of 1000 is a factor 2 away from the realistic mass ratio of 1836, but this is likely unimportant. Note also that again the domain only extends down to $r = 5$ cm, and once reflected ions reach this point the simulation is terminated.

In the bottom half of the figure, the quadrupolar magnetic field is visible in front of the imploding current layer. This field, as mentioned earlier, is from the reflected ion beam

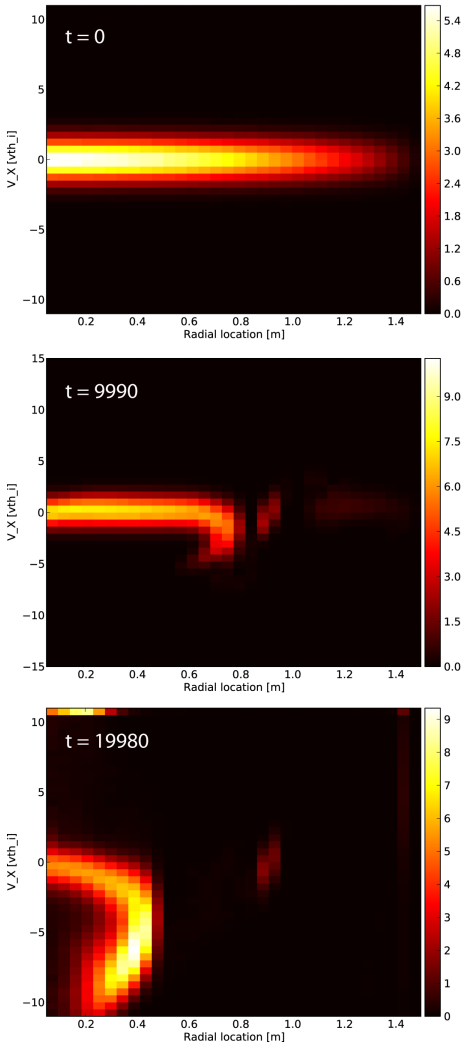

Figure 3.14: Three plots showing the velocity distributions along a radial slice at the midplane of the experiment. The timesteps are VPIC timesteps, which here are much less than the electron plasma period (and as in the experiment the entire compression last only a fraction of an ion cyclotron period). This simulation was scaled to experimental parameters, with a 0.5 mT nominal field strength, initial mirror field and drive current similar to the experiment. Note that the y-axes and colorbars are not identical. In the final plot, it is clear that the piston is moving approximately $4v_{\mathtt{thi}}$ and reflecting a population up to twice that, with an overall thickness ~0.2 m.

and the circulating magnetized electrons closing the current loop. However, superimposed on this are three other smaller quadrupolar signals centered between each pair of drive coils. These are the result of discrete exhaust jets of ions launched by the reconnection events between each pair of coils. This can also be seen in Fig. 3.7 as an axial variation in the density of the reflected ion foot.

The final result from the simulation work to be shown here are the velocity distribution plots in Fig. 3.14. These plots show the radial velocity distribution from a section of the experiment taken around $z = 0.15$ m. Note that the scales and colormaps are not identical between plots, and that the x-axis (radial dimension) extends from 0.05 to 1.5 m. While the initial plasma distribution is not realistic (the experimental density beyond the coils is likely smaller than the simulation), the final plot shows the reflected ion population clearly moving at around 8 $v_{\mathtt{thi}}$, twice the speed of the current layer. The thickness of the layer in that same plot, measured from where the initial velocity distribution begins deviating to

the vacuum region, is ~ 0.2 m or about one upstream ion skin depth. One can also note the small amount of plasma being injected near the coil boundary at 0.94 m, which attempted to improve the simulation by modeling ionization from the coil inductive electric fields.

3.16 Single Particle Qualitative Interpretation

The VPIC algorithm works by updating in turn the particle positions and then the electromagnetic fields. The "particle pusher", as its known, uses the Boris Method. This is a second order accurate, energy conserving algorithm for applying the Lorentz force to particles.

Here, the Boris method is used independently of the full PIC simulation: test particle positions are evolved in time along with the experimentally measured electromagnetic fields. More description of this algorithm is provided in Sec. 4.12. While this technique could be used to quantitatively compare with the experiment, here we will not be so rigorous as we seek only qualitative insight.

Shown in Fig. 3.15 is a cross sectional representation of the theta pinch experiment. The thick black line represents the drive coils at R = 0.92 m. The color contours in each quadrant are from the radial profile in Fig. 3.2 assuming toroidal symmetry. The only addition is E_ϕ, the inductive toroidal electric field from the change in magnetic flux.

Eight individual hydrogen ions are initialized at the same radial location, all with an initial velocity to the right with magnitude equal to the thermal speed ($v_i = 20$ km/s). This forms a representation of all particles with a perpendicular velocity less than one thermal speed. The particles positions are marked by the blue circles, and the trajectories of each by the colored paths. The timestep for the Boris algorithm is the 10 MHz experimental digitization frequency. This is much greater than the ion cylcotron frequency ($f = \omega_{ci}/2\pi =$ 7.6 kHz at 0.5 mT) and so is a reasonably accurate reconstruction.

There are two important results from this. Firstly, no reflected ions have a gyroradius less than the experiment radius. This can be seen in the bottom plot by looking at the radius of curvature of the line segment between the initial position and the closest approach to the axis. This confirms what we knew from earlier estimates that these particles are not magnetized enough to return to the layer before the layer has fully imploded.

The second result is that the reflected ions produce a net toroidal current at low radii. It can be seen from the lower plot that every trajectory has a positive angular velocity at the point of closest approach to the axis. A second simulation was performed where the initial field was reduced to zero, and in that case three of the eight particles had a negative

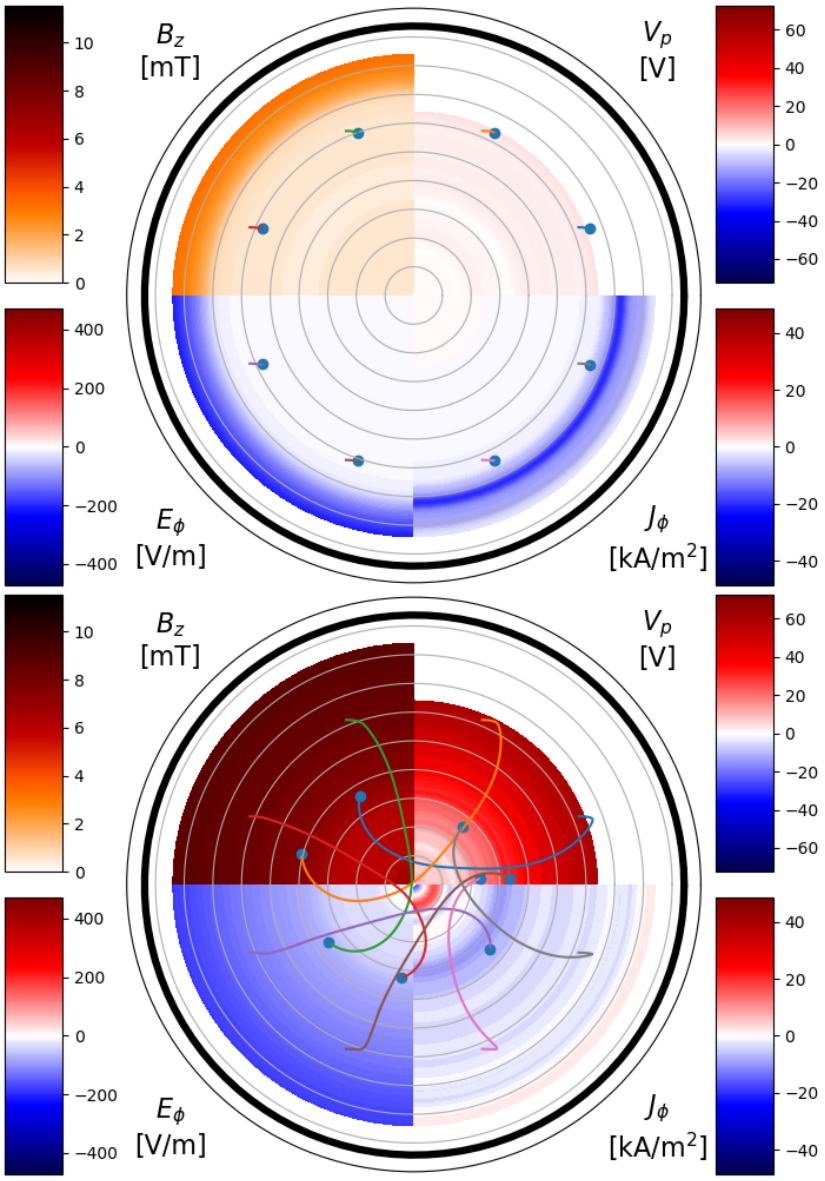

Figure 3.15: Two frames from a particle trajectory calculation using the experimentally measured electromagnetic fields and simulated test particles. 8 particles are initialized with the same speed moving to the right, giving them an approximately thermal range of cylindrical velocities. In the early time frame above, the particles (blue dots) sweep out paths (colored lines) based upon the Boris algorithm used in VPIC and other PIC simulations. In the later frame below, all of the particles pass to the right of the axis or in the positive toroidal direction. This net positive toroidal ion current is the mechanism behind the rise in the axial field ahead of the current layer, seen in Fig. 3.2. Note the very large radii of curvature before the ions reach their minimum radial distance, a result of the weak initial background magnetic field.

angular velocity. This is evidence for the earlier claim that the initial rise in the axial field beginning at 12 μs shown in Fig. 3.2 is an unusual ion current.

It is worth observing that, while this demonstrates that the ions are not magnetized, this still demonstrates the expected evolutionary behavior of the magnetized ion case. In the magnetized case, there would be a period lasting approximately one ion gyroperiod ω_{ci}^{-1} during which the foot extends a distance 0.68 u_{layer}/ω_{ci} ahead of the layer [123]. After this period, the gyrating ions would re-encounter the layer, increasing the upstream ram pressure. This would cause the layer to slow as a new pressure balance equilibrium is reached.

In the existing experiment, as the reflected ions re-encounter the layer, they cause it to

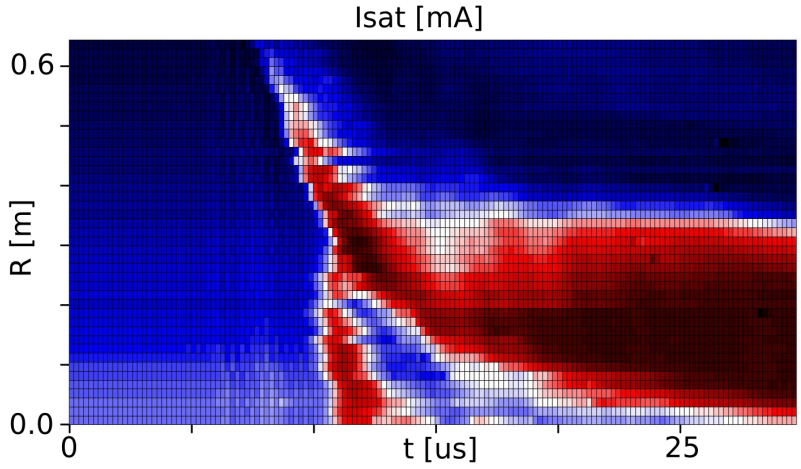

Figure 3.16: Results from a coarse scan performed at high field $B_z = 5.0$ mT. The unexpected shape, including low density on axis, reflects the intermittent shift off axis of the initial plasma due to the unstable mirror equilibirium, which is likely perturbed by the probe shaft.

briefly stagnate before it begins moving inwards again around 20 μs (Fig. 3.2).

3.17 High Magnetization Experiments

In 2019 the theta pinch experiment was rerun to both reconfirm prior results and to attempt to run the experiment at fields strong enough to magnetize the ions (such that $\rho = v_{layer}/\omega_{ci} < R_{exp}$). Several configurations were tested, and all failed to produce a repeatable experiment. Nonetheless, there were promising signs that the experiment had achieved the desired conditions. Future work is needed to produce a stable background plasma and rerun these experiments.

In the first configuration, 12 guns (6 on each pole) were used to produce the highest plasma pressure possible. A strong mirror ratio of 10 was used with a 3.0 mT Helmholtz field, chosen such that a proton traveling at 100 km/s would have a Larmor radius of ρ_i 0.35 m. If the ions were magnetized, we would see the reflected ion foot travel until it was 0.68 ρ_i ahead of the layer [123, 95], observe the layer speed change as the first ions have completed a gyration back to the layer, and perhaps even witness the development of a shocked downstream population.

Results from the first are show in Fig. 3.16. While the I_{sat} traces look suspiciously like what would be expected for the magnetized ion case, fast camera images of the events revealed this is a poor interpretation. Instead, the low-beta mirror configuration was subject to what appeared to be a strong $m = 1$ interchange instability: the entire plasma column on certain shots shifted off axis in the $+\hat{x}, -\hat{y}$ direction. This was observed for most for the shots where the Langmuir probe was at low radii. That probe was around $\theta = 2\pi/3$ away from the direction of the shift.

It was observed that the cusp configuration of the BRB is quite important for stability

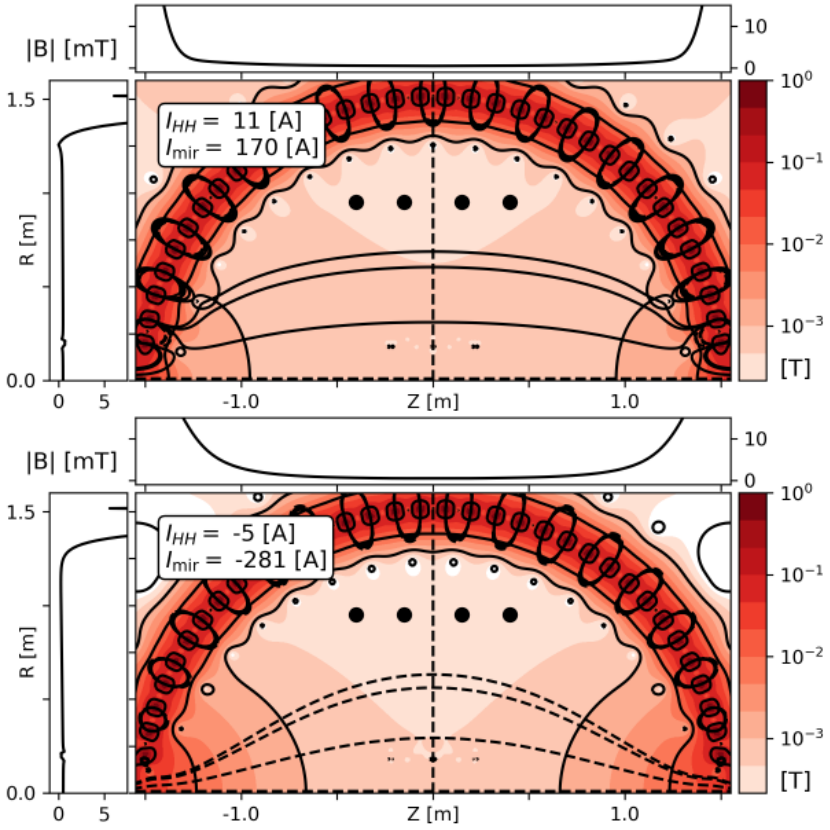

Figure 3.17: Two magnetic field geometries similar similar to those used for the high field theta pinch magnetization experiments. The southward pointing geometry (dashed lines) used for the theta pinch was unstable to some mirror instability, presumably an interchange type mode. The null points in the northward pointing geometry and the small regions of good curvature, may play an important role in stabilizing the geometry. The three field lines drawn extend from the locations of the three rings of the gun array.

of the target plasma. With the Helmholtz coils pointing in the North direction (as it is for the TREX experiments), at moderate field strengths a null point in the cusp magnetic field exists along the field lines extending from the gun array. If the Helmholtz coils are reversed, the geometry changes substantially, as shown in Fig. 3.17. This may explain the differences seen between the theta pinch and TREX experiments, where the direction of the Helmholtz field is reversed.

After the failure of the plasma gun array to produce a stable, large radius plasma at high field strength, a magnetized target plasma was attempted with the two Compact Toroid Injectors. Without the mirror coils, a simple axial field of 3.0 mT was applied, and two CTs were fired and collided in the center of the vessel. After enough time passed so that fluctuations decayed away, the theta pinch was fired.

Unfortunately, this was also unsuccessful. Waiting until the fluctuations were small enough that the experiment was repeatable also meant that the plasma radius had decreased to around 0.3 m. And the diamagnetism also introduced a substantial gradient at the edge.

Ultimately, a configuration where the field was strong enough to magnetized the ions and where the plasma was stable could not be found. The high-beta case was stable because the plasma diamagnetism hollowed out the field profile. Reversing the polarity of the drive coils (which was not possible at the time of the experiments) might enable

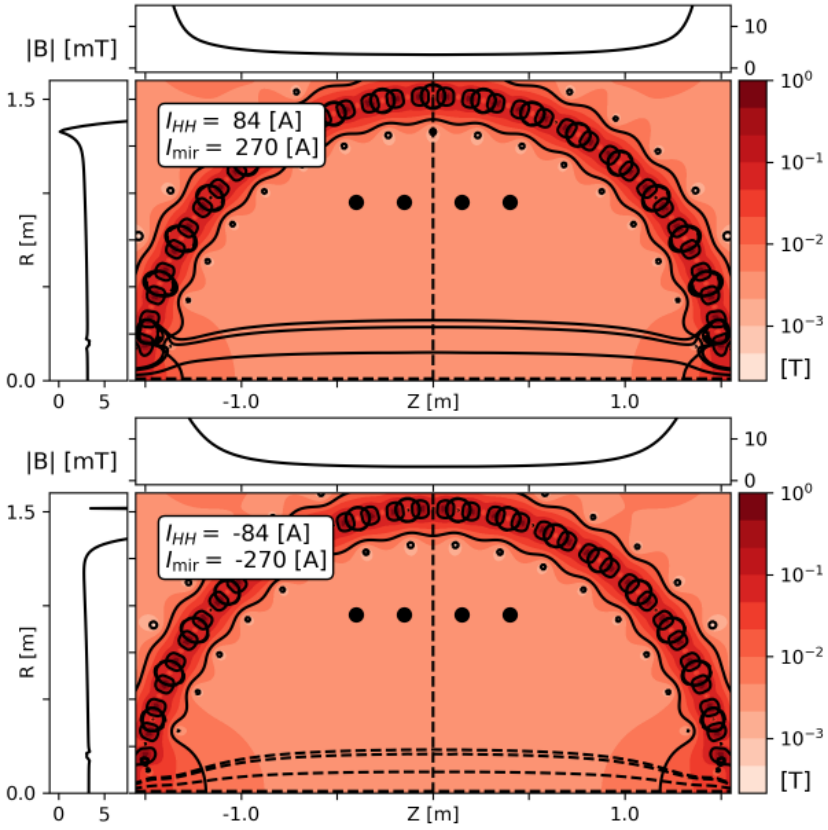

Figure 3.18: Plot of magnetic field strength and flux surfaces for two configurations similar to the theta pinch primary scan with identical mirror ratio $R_m = 100$ and nominal field of $B_z = 0.5$ mT. Dotted field lines are pointed South, while solid field lines point North. The strong difference between the two orientations is because of the residual field from the BRB cusp magnets, which is enhanced as the smallest pole rings have been removed. As before, the three field lines drawn extend from the locations of the three rings of the gun array.

the experiment to operate in a stable configuration. However, producing plasma at large enough radius such that $\rho_i \ll R_{exp}$ will remain a challenge. Possible solutions are proposed in the summary chapter.

4 PARALLEL SHOCK EXPERIMENTS

4.1 Intro

As in Chapter 3, the first part of this section has been neatly lifted from a *PRL* submission. The latter half is additional material supporting points casually mentioned or assumed in the paper.

4.2 Abstract

A flexible laboratory configuration on the Big Red Ball device has been created for studying parallel shocks by firing a coaxial plasma gun into a preexisting plasma. At Alfvén Mach numbers near $M_A \sim 2.4$, we observe the plasma piston both initiate a dispersive whistler pulse and reflect ions that are collisionless against the background. Shock reflected ions are focused into a beam by a concave-forward potential structure. This focusing, and the cyclotron resonance with leading whistler waves, are mechanisms for collisionless shock heating.

4.3 Motivation

How do collisionless shocks generate the dissipation necessary to satisfy mass, momentum, and energy continuity? For perpendicular shocks, ion reflection and gyration back to the layer is responsible for dissipation beyond resistive or anomalous heating [46, 70]. For quasi-parallel shocks, reflected or shock heated ions can escape upstream without gyrating back to the layer [35]. One theory has these counterstreaming ions steepening foreshock whistler waves until the waves are able to reflect upstream particles, effectively advancing the shock front forward [13, 87, 101, 23]. These steepened pulses merge into a dynamic and extended transition layer beyond which the magnetohydrodynamic continuity equations are ultimately satisfied [104, 102, 77]. This "pulsation shock" model of quasi-parallel shocks explains several features of spacecraft observations of the Earth's bow shock [15].

The substantial challenges to producing properly collisionless parallel shocks in the laboratory means that suitable platforms are scarce. Older pulsed power experiments, which used magnetic pistons with poor shot-to-shot variability, were solidly in the collisional regime [28]. Recently, laser platforms have had success in launching collisionless shocks [43], but at parameters where the background magnetic field is dynamically unimportant (i.e. $\beta \equiv P_{plasma}/P_{mag.} \gg 1$). Other laser plasma experiments have observed beam instabili-

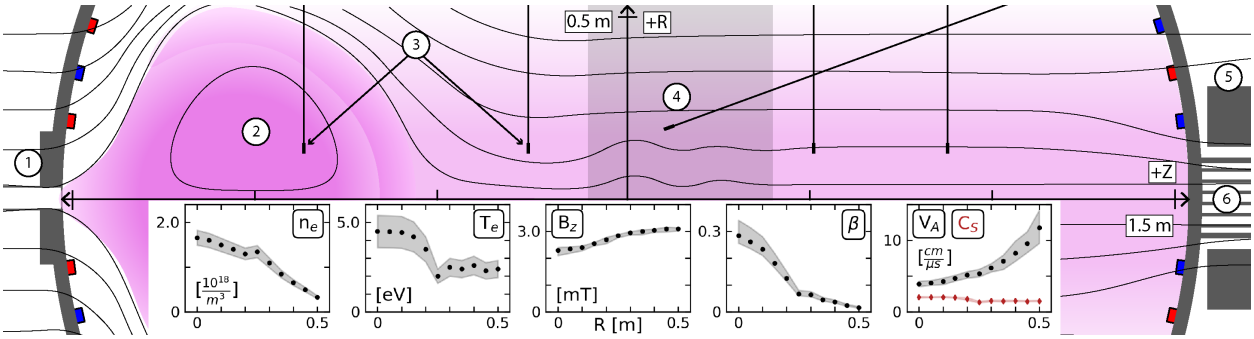

Figure 4.1: Diagram of the experimental setup during a shot. Guns at the North pole (6) produce the background plasma, which fills the field lines (black) produced with a Helmholtz coil pair (not shown) and a single mirror coil (5). The high-β piston (2) enters the vessel from the coaxial plasma gun barrel (1) and expands radially as it translates. The four hanging double probes (3) are shown at fixed locations of R=+0.15 and Z=-0.86,-0.25,+0.52,+0.88 m. The multi-tip Langmuir probe (4) can scan the shaded area. The five plots on the bottom show the initial parameters for the primary scan at 3.0 mT applied field.

ties important to quasi-parallel collisionless shocks, but have not observed compression or shock heating [114, 61]. The lack of platforms capable of producing large ($L_{exp} \gg c/\omega_{pi}$), magnetized ($L_{exp} \gg \rho_i$), collisionless (both $\omega_{ci} \gg \nu_i$ and $\tau_{exp} < \nu_i^{-1}$) plasmas along with a high Alfvén Mach number ($M_A \equiv u/v_A$) piston has led to a lack of experimental work that might corroborate the pulsation shock model.

We report a new laboratory configuration implemented on the Big Red Ball device in which parallel collisionless shocks are formed by a non-linear whistler wave. In the experiment, a high pressure piston collides super-Alfvènically with a stationary background target plasma. The piston plasma diamagnetism sharply bends upstream field lines and this magnetic kink disperses ahead as whistler waves. A concave forward potential extends from the piston leading edge that reflects and focuses an ion beam. Measured plasma parameters indicate that the ion beam is fully collisionless. Geometric considerations suggests that reflection off the V-shaped potential heats the ions, a collisionless dissipation mechanism distinct from the perpendicular case. While not observed directly, cyclotron resonance of the reflected ions with the whistlers may further scatter and thermalize these particles towards the well known Rankine-Hugoniot jump conditions. Although the experiment is too short to exhibit cyclic reformation, it demonstrates simultaneous production of two essential elements of the pulsation model: reflected ions and resonant whistler waves.

4.4 Experimental Design

To launch the high pressure piston, a coaxial plasma gun (modeled after one developed for the C2-U experiment [78]) is mounted on the South pole of the Big Red Ball (BRB) as shown in Fig 4.1 [44]. The gun is operated without poloidal bias flux, keeping its internal field low ($|B_{piston}| \leqslant 0.5$ mT at machine center), plasma beta high ($\beta_{piston} \gg 1$), and decreasing the shot-to-shot variability. The 70 μF capacitor bank is charged to 8-10 kV and discharges a primary current I_p of 120-150 kA with a rise time of $\tau_{1/4} \leqslant 5\mu s$. The speed of the piston varies from $u_p = 60 - 150$ km/s and is best controlled by adjusting the delay between the puff valve and main gun triggers, setting the total particle inventory and thus piston mass.

The target hydrogen plasma is produced with an array of washer guns mounted on the North pole, with adjustable total power up to 700 kW and density from $n_e = 0.0 - 2.0 \cdot 10^{18}/m^3$ [40]. Background neutrals are predominantly hydrogen with a density of $n_n \leqslant 1 \cdot 10^{17}/m^3$. The axial magnetic field B_z is produced with an external Helmholtz coil pair and can reach 9.0 mT. A weak mirror field around the washer guns (mirror ratio of 3) is used to increase the plasma radius while avoiding a strong axial gradient to the field.

With these three experimental knobs of u_p, n_e, and B_z, the plasma beta $\beta \equiv 2\mu_0 nT/B^2$ and Alfvén Mach number $M_A \equiv u_p/v_A$ can be controlled. This control is not fully independent, as for non-zero β the plasma diamagnetism weakens the field on axis (visible in center plot of Fig. 4.1). For low frequency whistlers ($\omega < \omega_{ce}/2$), such a configuration has long been known to duct waves via refraction [60, 109]. While we explore a wide range of Alfvén ($0 \leqslant M_A \leqslant \infty$) and sonic ($3 \leqslant M \leqslant 6$) Mach numbers, the particular density and magnetic field strength presented in this paper are chosen for their clear whistler signals. For a nominal piston speed of $u_p = 100$ km/s, the experiment has $M_A \sim 2.4$ on axis but becomes sub-Alfvénic for $R \geqslant 0.45$ m.

The experimental measurements come from four fixed hanging probes and a scanning probe shown in Fig. 4.1. The four hanging probes are located at $Z = -0.88, -0.26, +0.52, +0.88$ m and $R = 0.15$ m, with the first and second pairs offset in the toroidal direction by 60°. Each hanging probe has four planar tips operated as two double probes measuring ion saturation current I_{sat} and an orthogonal set of 3 $\dot{B}$-coils separated by 1 cm, all digitized at 10 MHz. Density measurements from the hanging probes are calibrated to the colder background plasma and thus overestimate n_e elsewhere. The Langmuir/T_e probe is a 16-tip probe with 3-axis $\dot{B}$-coil set capable of resolving the electron temperature and magnetic field at 5 MHz. That probe scans the shaded region in Fig. 4.1, from $Z = -0.1 - +0.4$ m and $R = 0.0 - 0.5$ m in 5 cm steps. Radial profiles of the target plasma for this primary scan are shown at the bottom of Fig. 4.1.

This experiment, like many pulsed power experiments, has relatively poor repeatibility that complicates the analysis. To complete a scan, shots are taken at each T_e probe location until a piston velocity of $u_p = 100 \pm 10$ km/s is observed, forming a data set of around 200 shots. While the target plasma and magnetic field are highly reproducible, variability in triggering of the high voltage switch and in the piston speed are significant. Aligning data between shots requires offsetting in time for shot-to-shot jitter, and in a few outlier cases also multiplying the time axis by a factor u_p/u_p^{mean} to correct for the speed.

4.5 Results and Analysis

To show the shock development as the piston traverses the vessel, in Fig. 4.2(a) we plot data from the hanging probes as well as the T_e probe. For this set of five shots, the piston speed is $u_p \sim 85$ km/s. The T_e probe is at the same radial location $R = 0.15$ m as the hanging probes and is moved in Z between shots. The piston enters from the machine South pole at $Z = -1.5$ m (top of plot) traveling towards the North wall at $Z = 1.5$ m (bottom). We identify the peak piston density in red and the axial field magnetic ramp in blue, which respectively mark the piston center and leading edge. The earliest rise in density (black) and the earliest coherent whistler signals (green) are both propagating faster than the piston. When the first whistler signals reach the far wall at $t = 12$ μs, the system has developed for 3 ω_{ci} and each front is separated by several $c/\omega_{pi} \sim 0.18$ m.

Fig. 4.3 shows the plasma potential, magnetic field, and density from a radial scan of 11 shots. The time axis is reversed so that the structure resembles the cartoon in Fig. 4.1. At top, a large V-shaped potential is marked with dashed lines, and a second, smaller potential can be seen on axis 5 μs ahead. In the center, the toroidal magnetic field B_ϕ is plotted with poloidal field lines in black, and waves of decreasing frequency in time are visible. At bottom, the high density piston collides with the target and produces a focused ion beam, visible from 6 to 11 μs and extending out to $R \sim 0.2$ m.

We unambiguously identify these early waves as whistlers from their right-handed polarization, agreement with the R-wave dispersion relation, and the factor 2 difference between the peak phase and group velocities [21]. In Fig. 4.4(b), we calculate the group velocity from the earliest coherent circularly polarized signals in the $\dot{B}$ data. The dot-dash line intersects the vessel wall at the same time as the piston enters. From this we infer that the whistler pulse is initiated as the very high-β piston bursts into the vessel and bends the upstream field lines. This strong initial perturbation can be interpreted as a large amplitude nonlinear whistler wave [72] that disperses into the upstream. That the highest measured wavenumbers in Fig. 4.4(c) approach $2\pi c/\omega_{pi}$ suggests that the initial thickness of this

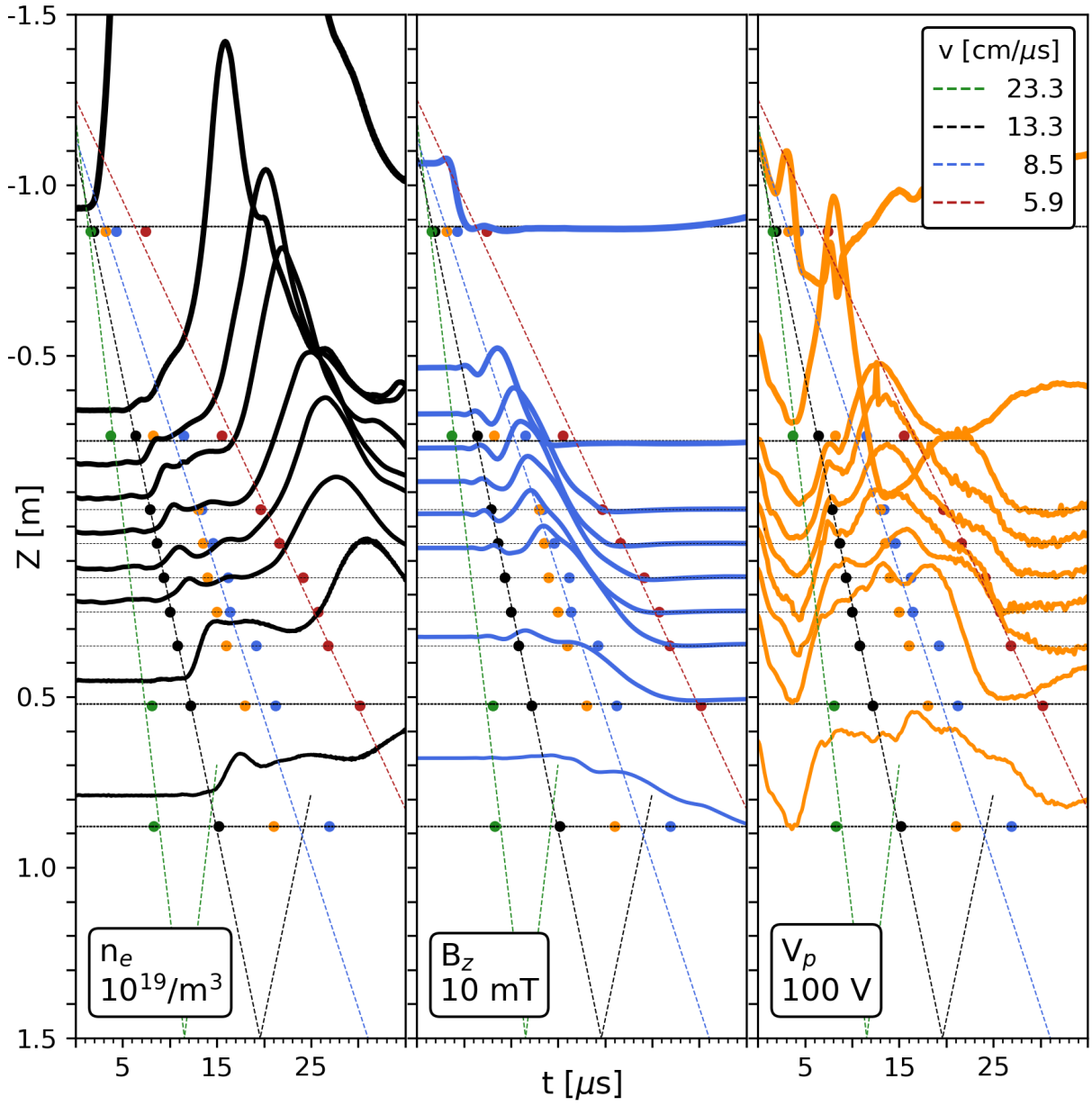

Figure 4.2: Measurements of density n_e and axial magnetic field B_z, taken at $R = 0.15$ m and offset in Z. The four color points (red, blue, black, and green) represent locations of peak density (piston center), magnetic ramp (piston front), earliest density increase (ion beam front), and earliest coherent polarized signals (whistler front), with speeds shown in the upper right. At $t = 12$ μs there is separation of multiple c/ω_{pi} between each.

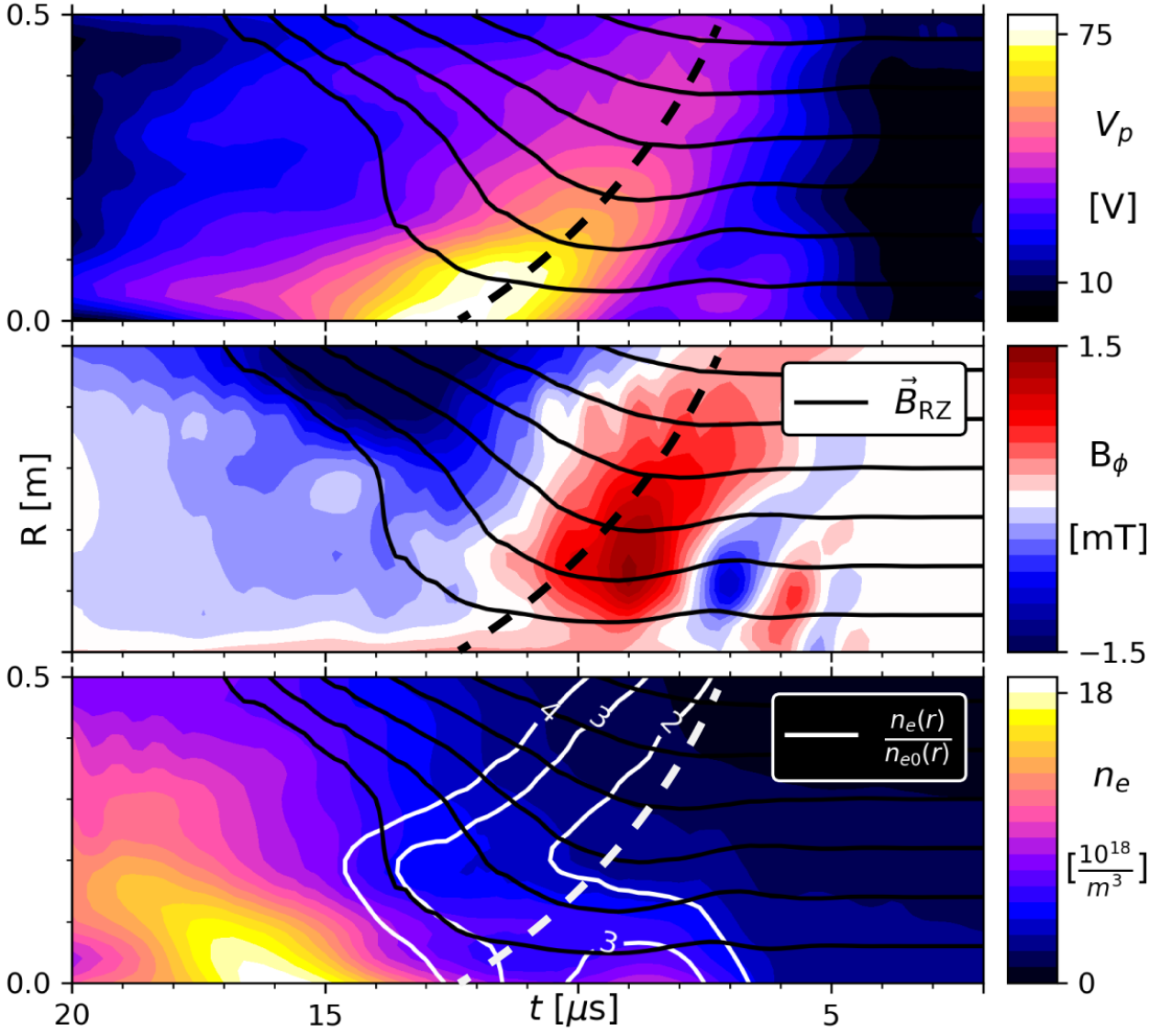

Figure 4.3: Using data from a single radial scan at Z = −0.1 m, 2-D time profiles of plasma potential V_p, toroidal magnetic field B_ϕ, and n_e. Black contours are poloidal magnetic field lines. The dashed line follows the V_p peak and forms half of the V-shaped potential. In the center, the highest frequencies of the whistler pulse arrive at 4 μs. White contours on the bottom plot track where n_e is 2, 3, and 4 times the initial radial value. The ion beam that arrives at 6 μs and R < 0.2 m is from focusing of reflected ions towards the axis.

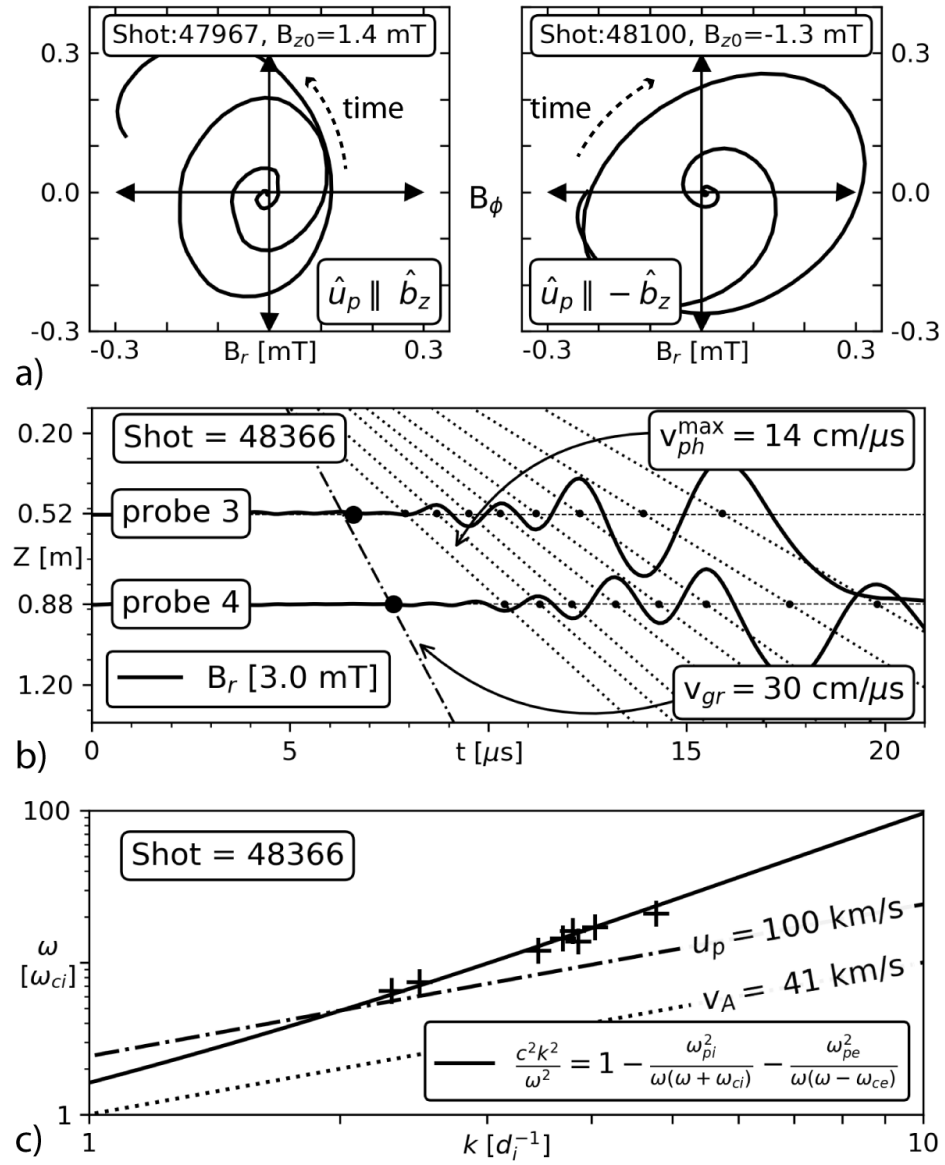

Figure 4.4: (a) Hodograms from the Z=0.52 m probe for two shots with the Helmholtz field direction flipped. The wave remains right hand circularly polarized w.r.t. the field direction. Peak frequencies are above 20 ω_{ci}. In (b), B_r traces from the Z=0.52 and 0.88 m probes. The dotted lines estimate the phase velocity v_{ph} while the dash-dotted line estimates the group velocity v_{gr} from the earliest coherent polarized $r\phi$-signal, which is close to the expected $2v_{ph}$. (c) The R-wave dispersion relation for $B_z = 2.4$ mT and $n_e = 1.6 \cdot 10^{18}/m^{-3}$. Crosses are values of ω and $k_{||}$ measured from (b), with the Alfvén and piston speeds for reference.

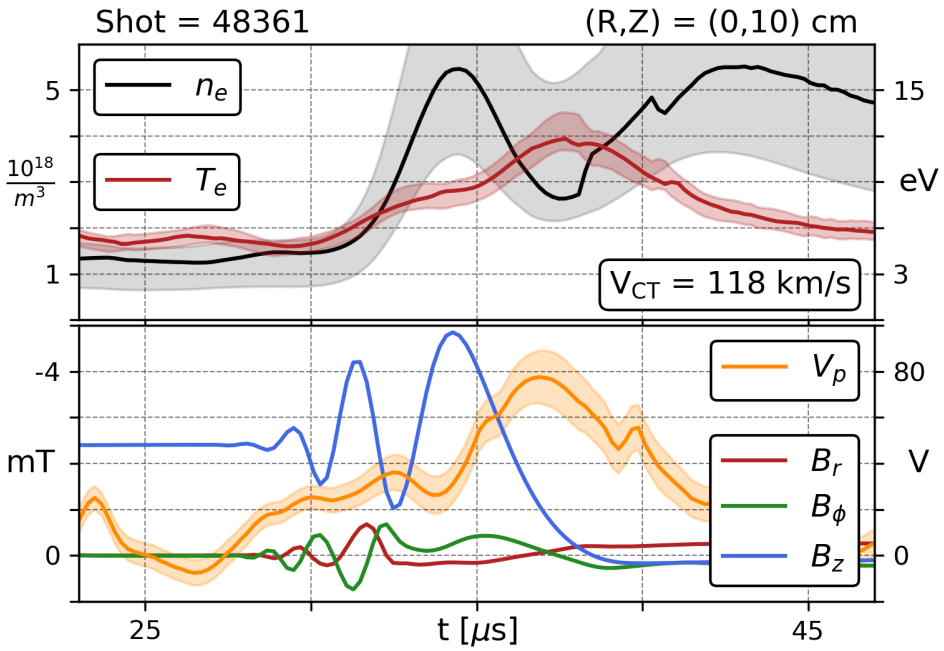

Figure 4.5: T_e probe time histories of density, temperature, plasma potential, and magnetic field. These measurements are taken on the axis, but +20 cm further in Z from the data in Fig. 4.3(b). The error bars are estimates of the total systematic error including the Langmuir fitting routine, and not the much smaller standard deviation of statistical noise. The potential fluctuations from 23 to 27 μs are global ($dV_p/dz = 0$), while the later fluctuation do indicate local electric fields.

magnetic kink is close to the target plasma ion skin depth.

More magnetic signals, here taken on axis, can be seen in Fig. 4.5 which shows time histories from the T_e probe for a representative shot. The substantial B_z fluctuations are not indicative of oblique propagation but are instead a feature of the wave solution to the cylindrical boundary conditions, akin to an $m = 0$ Helicon mode shown in Fig. 4.10 [20]. The small B_r and B_ϕ signals are either due to probe misalignment or perhaps to contributions from $m \geqslant 1$ modes from a non-axisymmetric initial piston, a feature that is sometimes seen in fast camera images.

While the experiment's large electron collisionality ($\nu_{e0} \sim 5 \cdot 10^6\ s^{-1} \gg \tau_{exp}^{-1}$) is typical of laboratory plasmas, a high thermal electron collisionality doesn't preclude collisionless ion behavior or even acceleration of energetic electrons [89, 43]. We calculate ion interpenetration lengths L_i^* following laboratory plasma jet experiment convention [81, 82]:

$$L_i^* = \frac{u_p}{4\nu_s^{ii'} + \nu_s^{ie'}} \tag{4.1}$$

where the ν_s terms are the slowing rates as described in [64]. As shown in Table 4.1, we

	n_e, $10^{18}/m^3$	T_e, eV	B_z, mT	u_p, cm/μs	β_e	β_{ram}
target	1.6	5	2.6	0	0.3	
ion beam	3.5	8	3.5	10	0.9	12

	f_{ci}, kHz	$\nu^s_{ii'}$, kHz	$\rho_i \equiv \frac{c_s}{\omega_{ci}}$, m	d_i, m	L^*_i, m
target	40		0.13	0.18	
ion beam	53	4.7	0.16	0.12	5.3

Table 4.1: Plasma parameters on axis, and estimates of relevant frequencies and lengths. The ion interpenetration length L^*_i is calculated as described by Eq. 4.1.

estimate L^*_i for an upstream particle colliding with the beam to be 5.3 m, which is much greater than the thickness of the beam. While the ions are effectively collisionless, the electrons are everywhere collisional but still magnetized ($\omega_{ce} \gg \nu_e \gg \tau^{-1}_{exp}$). This limits comparison with astrophysical plasmas.

The concave forward potential structure reflects ions in an on-axis beam which is visible in Fig. 4.3(b) from 6 to 11 μs and $R \leqslant 0.2$ m. This moving potential jump is larger than the relative ion kinetic energy $K_i = 1/2 m_i u_p^2 = 52$ eV for $u_p = 100$ km/s and so can reflect ions. That the beam travels slower than $2u_p$ and that the density increase exceeds two suggests this is not perfect specular reflection. To investigate this further, we use the phase velocities to reconstruct the fields via the Taylor hypothesis. The resultant static electric and magnetic field structure is used to simulate the trajectories of 10^5 ions with an initial 2 eV thermal distribution impinging at 100 km/s. While this model ignores the time evolution of the structure, it reproduces the factor 3 compression in the density and shows a perpendicular ion beam temperature of $T_\perp \sim 8.6$ eV.

The leading edge of the reflected ion beam satisfies the cyclotron resonance condition [47]:

$$\omega - \mathbf{k} \cdot \mathbf{v}_{beam} \pm m\omega_{ci} = 0 \tag{4.2}$$

where m is the harmonic number. Using the wavelength λ at the leading edge of the beam measured from the B_r signals in Fig. 4.4, we find for $m = 1$ that $(\omega - m\omega_{ci})/k = 11 \pm 1$ cm/μs. This is resonant with the beam velocity $v_{beam} = 13.3$ cm/μs within a thermal speed ($c_s = 2.0$ cm/μs at 2 eV). However, the ion beam is well-separated from the piston for only 5 μs$\sim \omega^{-1}_{ci}$, which is likely too short for substantial beam-wave coupling [86]. In Fig. 4.5, the smaller potential hump visible in Fig. 4.3 appears at the next rarefaction of the axial field at 32 μs. Because of the short duration, we do not observe growth of this smaller potential and can not definitively claim that the wave gains energy from or helps scatter the ion beam.

4.6 Discussion

To summarize, we observe the formation of a parallel shock mediated by a non-linear whistler structure. The concave forward structure of the potential focuses reflected ions towards the axis. The speed of the ion beam, the compression ratio, and single particle calculations suggest that the beam has been heated well above the target plasma temperature. This focused ion reflection is a collisionless dissipation mechanism distinct from the reflection and gyration characteristic of perpendicular shocks, but is likely particular to the specific cylindrical experimental geometry.

The simultaneous production of reflected ions and resonant whistler waves in this parallel configuration is reasonable evidence for the pulsation shock model. An unambiguous laboratory demonstration would see the leading potential structure grow until it was able to independently reflect ions, at which point the shock would have advanced forward and be "detached" from the piston. To be able to observe wave growth, simulations suggest tens of ion cyclotron periods are needed [86]. Experimentally, this would mean increasing the magnetic field to extend the effective duration of the experiment such that $L_{exp}/u_p \gg \omega_{ci}^{-1}$. To do so would also require quadratic increases in the background density and piston ram pressure to keep β and M_A constant. This is not currently achievable at the Big Red Ball but may be possible on other facilities, although maintaining collisionless ions would be difficult regardless.

4.7 Null Case Comparison

One difficulty in identifying a shock in data is that any generic ramp looks like a discontinuity when viewed from enough distance. To avoid misidentification, it was necessary to characterize the "null hypothesis," that is what exactly does the piston look like absent upstream plasma? This vacuum configuration is depicted in Fig. 4.6 alongside a plasma background for comparison.

An important difference between the two is the relationship between the radial and axial fields. As the piston drives inwards and displaces field lines in the vacuum case, the cylindrical geometry means that the radial and axial fields are inextricably linked: for the axial field to decrease, the radial field gain some non-zero value, here negative since the initial field points North. This relationship is clear in Fig. 4.6. However, at 25 μs a small toroidal component appears. This is likely not from Whistler wave dynamics in at the edge as the phase between the r and ϕ components is clearly different from the plasma case. Instead, this is likely the internal fields of the piston, which by this point in its expansion

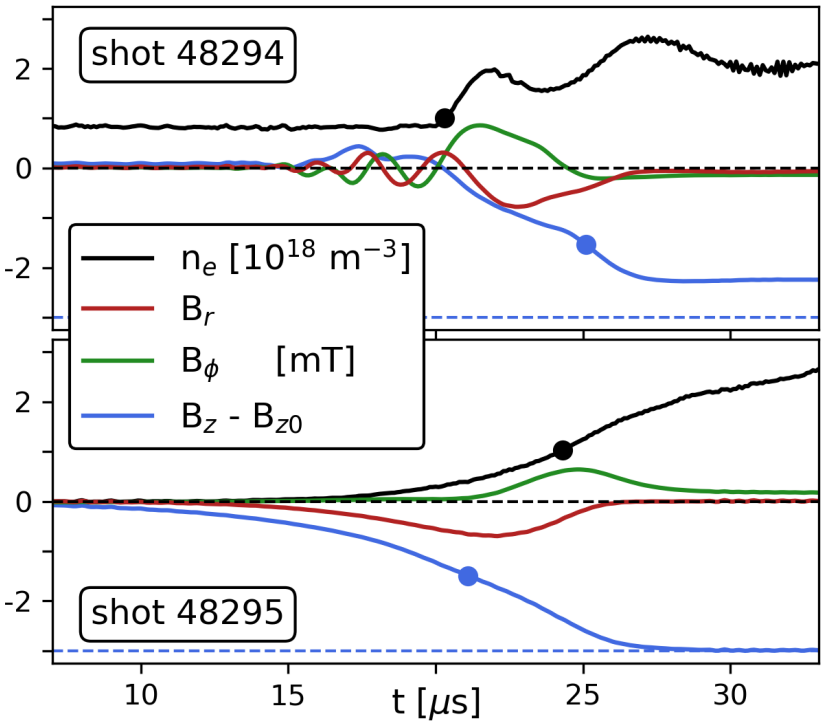

Figure 4.6: 1D profiles showing the difference between the vacuum and plasma background cases. The black and blue dots mark the points when the respective parameters cross the same threshold. The vacuum case exhibits a slow turn-on of both the density and the magnetic field. The plasma case shows a sharp increase in the density ($dt \sim 2\mu s$), with whistler waves both ahead and behind. Note the decrease in the total B_z jump, reflecting the background plasma diamagnetism.

and weakening is just slightly over 0.5 mT.

4.8 Radial Profile

In addition to Fig. 4.3, we can look at the radial magnetic dynamics in Fig. 4.7. Here, as in Fig. 4.3, it is clear that the Whistlers are limited to the lower radii. It is also obvious that the total field strength $|B|$ has significant fluctuations throughout the whistlers. These compressions approach the large amplitude $\delta B/B_0 \sim 2$ compressions often seen upstream of heliospheric shocks [118]. At larger radii, the total field strength is nearly constant up until the magnetic ramp. This is consistent with the transition to a sub-Alfvénic regime and a Shear Alfvén wave able to advect plasma out of the way of the oncoming piston. The piston internal magnetic fields, which vary substantially shot to shot, can be seen particularly at the R = 0.3 m trace around 18 μs as a second hump in the B_ϕ component.

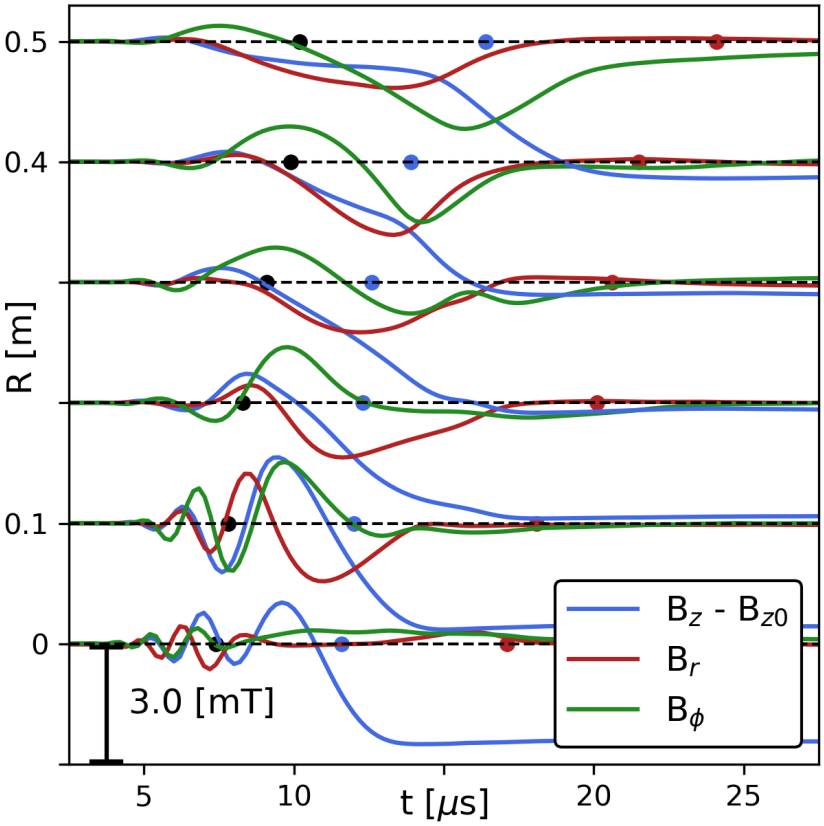

Figure 4.7: Radial scan of the T_e probe showing the variation of the magnetic signals from the super-Alfvénic core to the sub-Alfvénic edge. As before, the black, blue, and red dots respectively mark the locations of the earliest rise in density, the magnetic ramp, and the peak piston density. At $R = 0.5$ m, the total magnetic field $|B|$ stays approximately constant until the ramp. This is not the case at low radii. The jump in B_z increases from the center to the outside, showing that the initial plasma diamagnetism rearranges magnetic flux.

4.9 Whistler Dispersion Relation

Building on Fig. 4.4, the complete dispersion relation for an R-wave propagating parallel to the magnetic field [111]:

$$\frac{c^2k^2}{\omega^2} = 1 - \frac{\omega_{pi}^2}{\omega(\omega + \omega_{ci})} - \frac{\omega_{pe}^2}{\omega(\omega - \omega_{ce})} \tag{4.3}$$

is plotted in Fig. 4.8. There are several points worth mentioning.

Firstly, in order to estimate the wavenumbers in Fig. 4.4(b), we assumed that $k \sim k_{\parallel}$. The collimated plasma with higher density and lower field inside has phase velocity that increases with k. As a wave moves outward in radius, the same sized perturbation becomes a larger wavenumber because of the decreasing density. The increasing phase velocity refracts the wave inwards and collimates it. Clearly, this reverses for $\omega > \omega_{ce}/2$, and now hollow profiles duct the whistler waves [108]. There are substantial caveats for situations like this one where $k \ll R$, but I will not explore those here.

Secondly, as is obvious from Fig. 4.8 there is a maximum group velocity for whistler waves. This leads directly to the theorized Whistler critical Mach number M_c^{wh}. For a dispersion limited shock with an upstream standing whistler wave, if the flow velocity

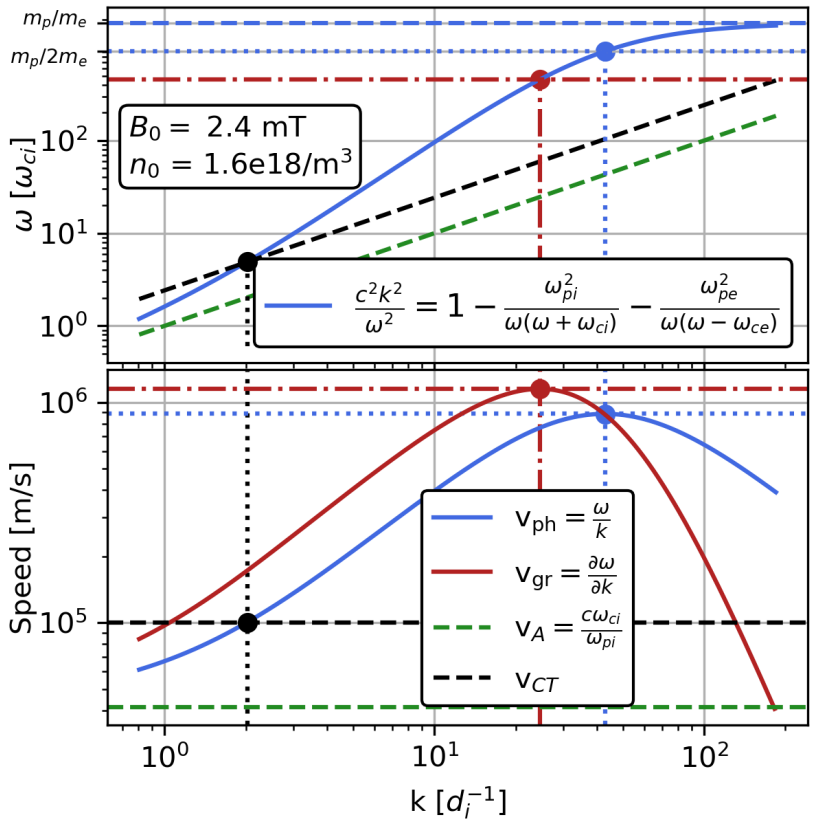

Figure 4.8: Full whistler dispersion relation for realistic plasma parameters. In the bottom plot, over the region from $k = 2 \sim 20$, the group velocity is roughly twice the phase velocity. The maximum group velocity is around $v_{gr} \sim 27\, v_A$. For a flow with velocity $u > v_{gr}^{max} \cos\theta_{bn}$, whistlers can no longer propagate ahead of the shock. This introduces yet another critical Mach number, the Whistler Critical Mach number, which depends on θ_{bn}.

exceeds $\sim 23 v_A$ the wave can no longer stand in the flow. The same principal as in the Friedrich diagram applies here, and this whistler critical Mach number gains a $\cos\theta_{bn}$ dependence: $M_c^{wh} = v_{ph}^{max} \cos\theta_{bn}$.

Thirdly, by definition a super Alfvénic perturbation will have either ω or k numbers that overlap with the whistler branch. This is obviously visible in Fig. 4.8 by the fact that anything super Alfvénic exists above the green dashed line. We can rewrite the definition of the Alfvén Mach number

$$M_A = \frac{u_p}{v_A} = \frac{u_p \omega_{ci}}{d_i} \tag{4.4}$$

in terms of the distance traveled by the piston in one ion cyclotron period compared to the ion skin depth. I raise this point only to reinforce the fact that, for a piston initiated flow, whistler waves should always be expected.

The second point here about the Whistler critical Mach number, is misleading in the experimental case. In fact, it appears (as will be discussed later) that the actual critical Mach number is much lower than v_{ph}^{max}/v_A. For a piston driven system, producing pertubations with wavenumbers higher than $2\pi d_i$ may actually be quite challenging. Fig. 4.9 shows a cartoon representation of the magnetic field lines as the piston is exploding into the vessel. In this drawing, the piston has reached radial pressure balance with the background field

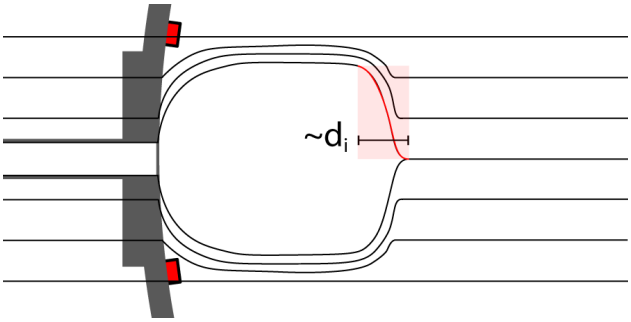

Figure 4.9: An only partially realistic cartoon of magnetic flux lines as the high pressure piston expands and translates into the vessel. The red highlighted line shows an interpretation of the jump as a smoothed step function of width c/ω_{pi}. The upper limit of the whistler wavenumbers at just below $k = 2\pi$ suggests this interpretation is reasonable.

(visible by the increased flux line density) but continues expanding axially. For the skeptic, feel free to imagine the leading edge inside the gun barrel and you can convince yourself that the same Y-point geometry must be present.

The radial component of the field lines at the leading edge of the piston, particularly the one highlighted in red, we can treat as a delta function but with a finite width of order c/ω_{pi}. This corresponding step function jump in the axial field can be seen in the top trace of the middle plot of Fig. 4.2. Its well known for a delta function that the Fourier transformation goes as $e^{-2\pi ikz}/ik$. As this isn't a perfect δ function, this extends only up to the highest wavenumbers present in the initial smooth ramp, beyond which it is 0. This then provides a fairly strict limit on the production of whistler waves in a piston driven experiment: if the ramp thickness is limited by the ion skin depth, than waves above $k = 2\pi d_i^{-1}$ might not be generated.

This is supported by Fig. 4.16, which shows that the whistler wave amplitude has vastly decreased even before $k = 2\pi$. As discussed at length in the following sections, the substantial error in the axial magnetic field measurements (and thus also the Alfvén Mach number) makes this plot far less accurate than ideal. Because of this error, the whistler waves observed at $M_A = 4$ could actually be at a much larger Mach number (e.g., 6.28), and thus might agree with the above prediction.

Is it possible instead that we just aren't properly resolving the highest frequency waves? Elsewhere, we've identified the group velocity by the first coherent circularly polarized wave. The Nyquist frequency to identify two waves 90° out of phase is twice as strict and so approximately 2.5 MHz. For the nominal case ($B_z = 2.4$ mT, $n_e = 1.6 \cdot 10^18/m^3$), the highest frequencies we observe are around $20\omega_{ci} \sim 700$kHz, which is well within our capacity to detect.

Instead perhaps there is not enough time for the highest frequencies to separate and be resolved? Or that the factor $1/i\omega$ from the corresponding frequency space Fourier transform weakens the signal too much to observe? Both of these are possibilities. However, were this the case then Fig. 4.2 might observe an obvious slowing of the group velocity

(green points and dashed line) which is just not seen.

Applying this to astrophysical situations, ramps are often seen to thin below an ion skin depth [63]. In our experiment because of the perfectly parallel geometry, whistlers are constrained to be perfectly parallel. In astrophysical plasmas they are not, and it appears that oblique whistler waves explain observations of thinning of the shock ramp width below an ion skin depth [72].

4.10 Helicon Physics

Helicon waves are solutions to the whistler wave dispersion relation in a bounded cylinder [20]. In this experiment, the collimated background plasma is akin to the bounded plasmas of helicons, except with an open boundary condition, rather than a conducting or insulating cylinder. The waves ahead of the CT piston are analogous to Helicon waves, as can be seen by comparing the ramp profile in Fig. 4.9 with Fig. 4.10a, whose first frame shows the nearly pure radial configuration superimposed on an axial background field.

The on axis magnetic signals in Fig. 4.5 and Fig. 4.7 both show clear whistler signals. If the $m = 0$ Helicon mode was a complete description of the system, these components should be consistently zero. As mentioned earlier, the $m = 1$ mode provides a possible explanation of the signals: the non-axisymmetric injection of the piston launches both $m = 0$ and $m = 1$ mode helicon waves. Evidence for non-axisymmetry is shown in Fig. 4.12. Fast camera images routinely show features like these, particularly when a large poloidal bias flux is used in the coaxial plasma gun.

4.11 Lessons Learned in Experimental Design

Not including a Hall probe to measure the initial magnetic field was a mistake. The relatively slow plasma turn on (~ 1 ms) and small change in field (~ 1 mT) makes measuring the initial plasma β challenging with integrated $\dot{B}$ probes. Compensating for the plasma diamagnetism becomes a somewhat painful procedure that is documented here. This section is a warning to others not to repeat these mistakes.

Fig. 4.13 shows the parameter space explored via the three control knobs of applied magnetic field, plasma heating power, and piston speed. While this is useful for demonstrating the remarkable versatility of the experiment, its not very helpful for understanding the dimensionless parameters (β, M_A) that actually matter. Without a direct measurement of the initial plasma axial field (a measurement that could be made with a Hall probe), we rely on the very high piston pressure to properly expel all of the field. Fig. 4.6 shows

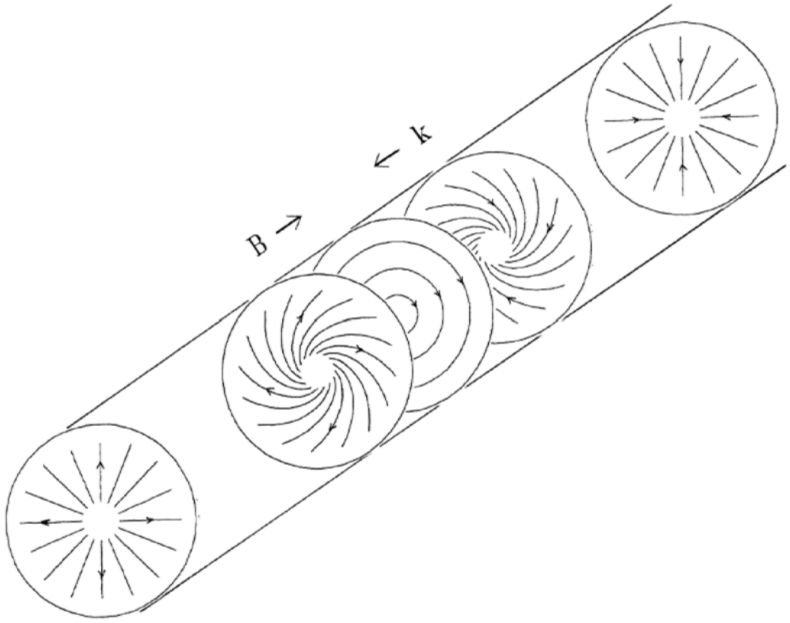

(a) m = 0

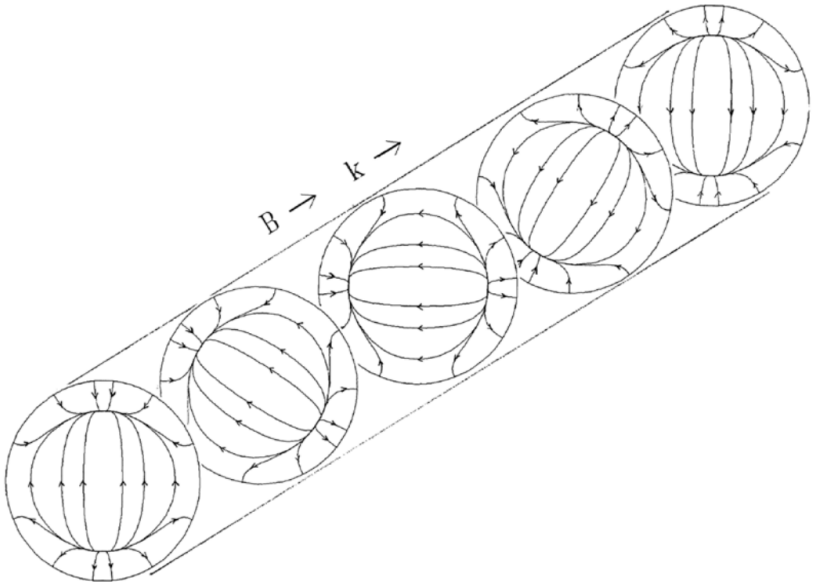

(b) m = 1

Figure 4.10: (a) The radial structure of the m=0 Helicon mode, taken from [20]. In a typical Helicon plasma, there is no or is only a very slight radial gradient, a consequence of the higher magnetic field and weaker plasma β. While on axis this is clearly the structure of the whistler wave packet observed in the experiment, the full solution merges with the Alfvénic eigenmode solution at large radii. (b) the m = 1 Helicon mode structure. Note that magnetic field on axis osciallates between $\hat{r}$ and $\hat{phi}$ directions, while the m = 0 case has only axially directed field on the axis. This could explain the small signals in Fig. 4.5, which is measured at R = 0.

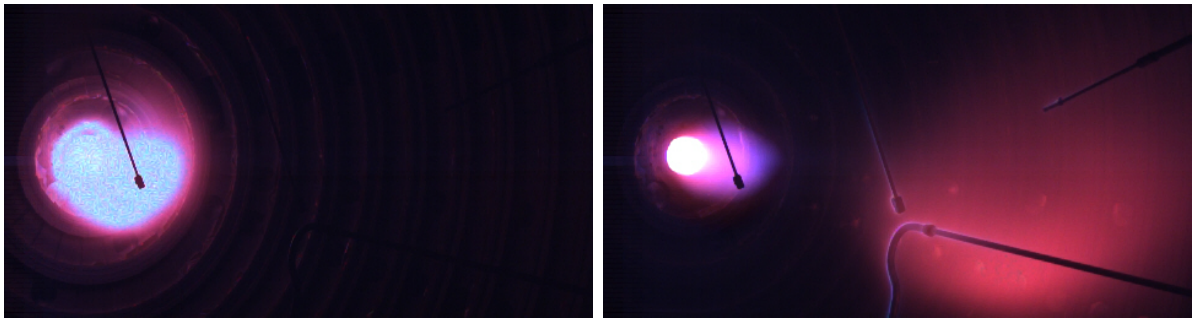

Figure 4.11: Two visible light images with ~ 1 μs exposure taken 20 μs apart showing neutral hydrogen emission from a piston as it enters the vessel in Shot 48129. Background plasma is present but invisible because of the short exposure. While this is a relatively axisymmetric case, it still is brightest to the lower left.

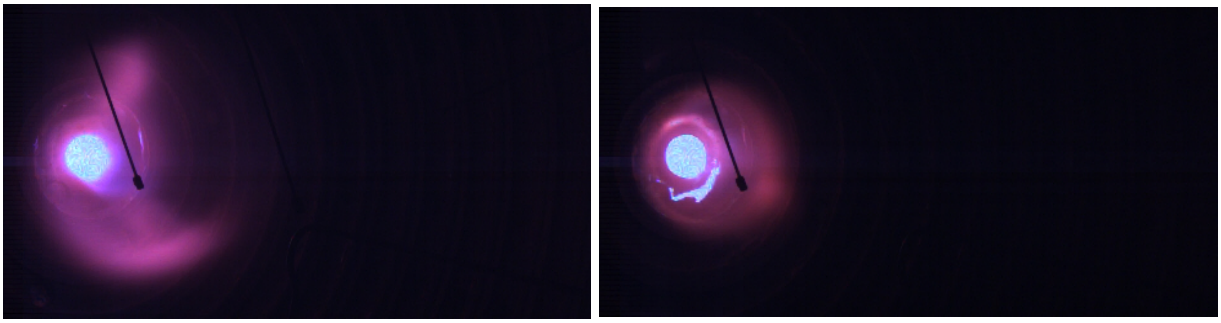

Figure 4.12: Two fast camera images from separate shots showing the variability of the plasma piston as it enters the machine. This variability is vastly reduced when the gun is operated with no poloidal bias field. The second image shows a kink like structure, which could be the primary current filament extending into the vessel.

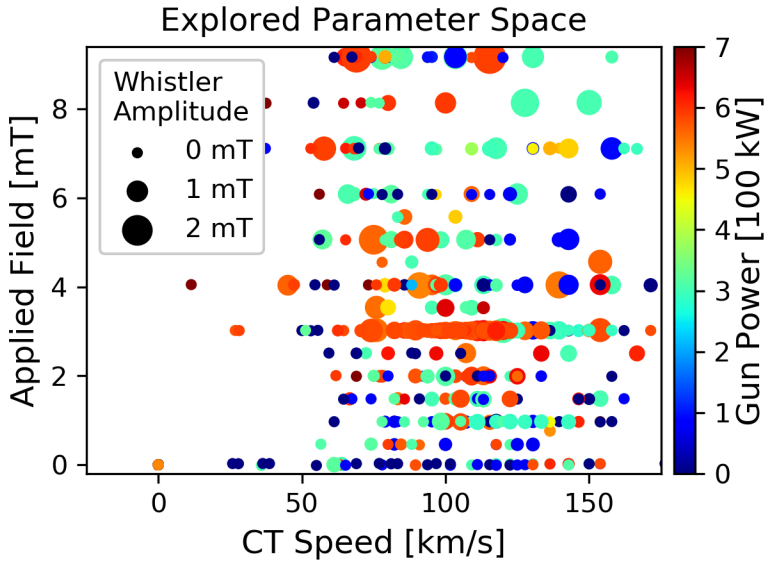

Figure 4.13: Parameter space explored in the parallel shock experiments. The axes and colors represent the controllable experimental knobs. To convert these into useful dimensionless (M_A, β) parameters, a substantial amount of work is needed.

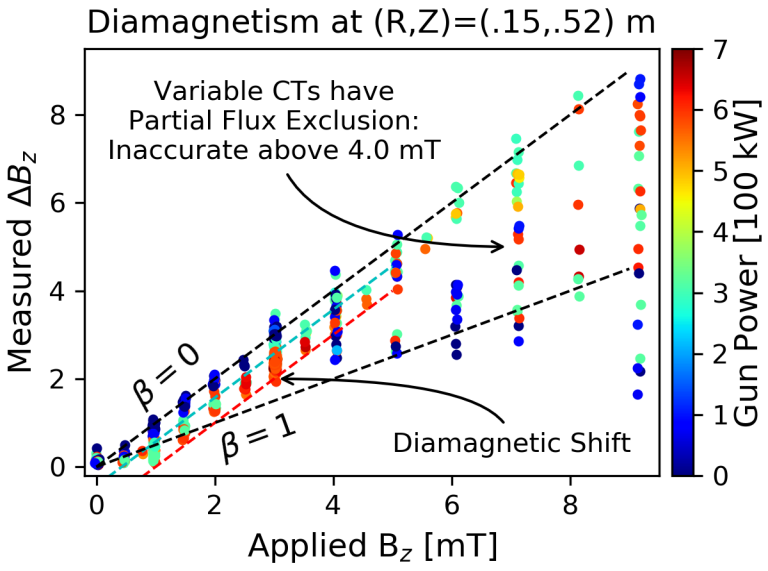

Figure 4.14: Diamagnetic effect of the plasma. In an attempt to measure the actual magnetic field in the initial plasma without a Hall probe, the jump in axial field ΔB_z as the piston translates past the probe can be used. At low applied field, a substantial shift due to diamagnetism is seen. At high field this technique fails because the piston internal pressure does not exceed the background magnetic pressure.

clearly the difference in the axial field between two consecutive shots, one with plasma and the other without. The applied field of 3.0 mT is measured in the vacuum case as the piston crosses the probe and nearly completely expels the flux. For the plasma shot, the initial field can be measured as the integrated jump in field, close to 2.4 mT.

While this procedure appears simple, there are many ways that an algorithm measuring this might fail. Most commonly, at higher fields the piston may not have enough pressure to fully expel the fields. This leads to an underestimation of the initial field, and an overestimation of the initial β and M_A number. Fig. 4.14 shows exactly this source of error. As the field exceeds 4 mT, the standard deviation in the measured ΔB_z explodes; the piston is not fully expelling the field, either due to not enough internal pressure or an off-axis trajectory. One would expect that for all the black points in Fig. 4.14 (the 0 gun power or vacuum background case), the applied and measured B_z should follow exactly the $\beta = 0$ dashed line.

To compensate for this diamagnetism, in Fig. 4.15 we scatter plot all the applied field and measured densities, with again plasma fueling depicted by the color. The relationship between the density and applied field is expressed via the dashed lines, which do a reasonable job fitting the data except at the lowest applied fields. To the left of the line, where $\beta \geqslant 1$, the plasma can significantly expand the plasma radius and cause the density to fall further. To produce Fig. 4.16, the trends from Fig. 4.14 and Fig. 4.15 are used rather than the measured n_e and ΔB_z, which both exhibit significant variability.

These techniques are used to avoid manually examining each of the many hundreds of shots taken in this run campaign. Not present in Fig. 4.16 are the tremendous error bars in both M_A and B_z. These plots are only produced here to show the general trends observed:

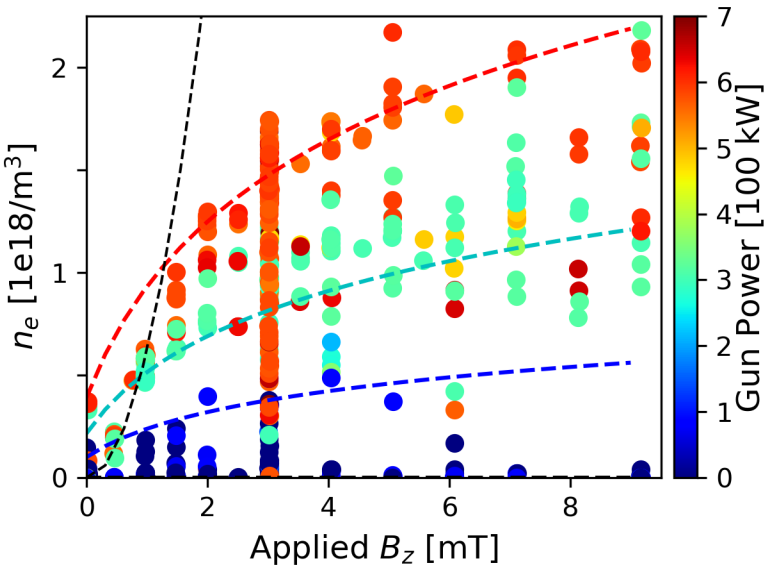

Figure 4.15: Further evidence of the plasma diamagnetism, from the relationship between the measured density and the applied magnetic field. While the variability is pretty large, it does expose trends in the relationship between the two. The black dashed line is a $\beta = 1$ line for constant temperature $T_e = 2$ eV, and to the left of the line ($\beta > 1$) the points deviate from the dashed trend lines..

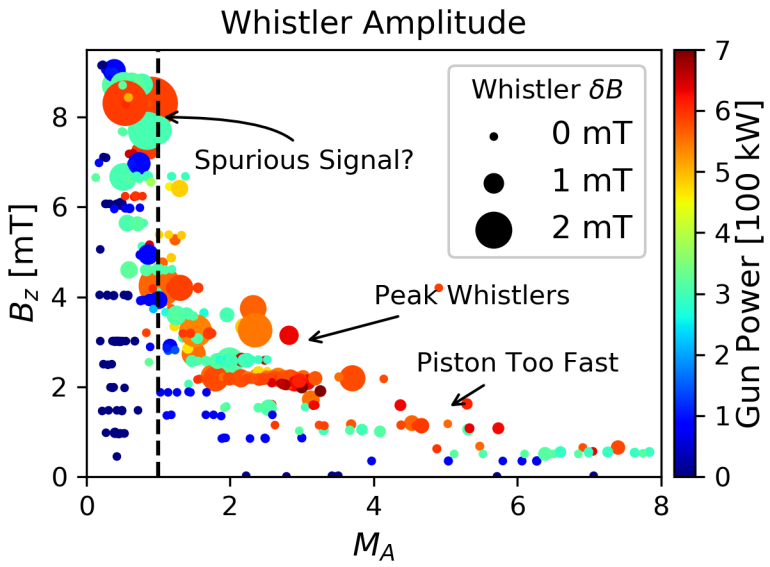

Figure 4.16: The measured plasma B_z and M_A and their relationship to the observed whistler signals, after correcting for the plasma diamagnetism. At high $M_A > 5-6$, whistler signals are not observed. This can perhaps be explained by the wave launching mechanism, which is caused by charge separation on the ion skin depth scale. The group velocity of whistlers at $k = 2\pi d_i^{-1}$ is likely slower than the piston velocity, hence no whistlers are observed.

whistlers don't appear when the piston is sub-Alfvénic, they peak in relative amplitude around $M_A \sim 2-3$, and disappear again at high M_A.

4.12 Single Particle Tracking: Boris Algorithm

Developed in 1970, the Boris algorithm is a second-order-accurate time-leapfrog scheme for advancing particle positions in a electromagnetic fields [6]. This algorithm is implemented in many PIC codes, including VPIC, as the particle pusher [8]. "Second order accurate" effectively means a small time resolution is required to accurately simulate particle trajectories, which for fast electrons (i.e. $\Delta t \ll \omega_{pe}^{-1}$) can be computationally expensive. The

"time-leapfrog" technique implies that the particle velocities are evaluated at half timesteps relative to the particle positions. In this way, the algorithm is very nearly energy conserving [57].

Here we are using it in a qualitative way to understand the behavior of background particles impinging on the concave forward potential observed in the experiment. This method is briefly described in the Results and Analysis section in this chapter and is elaborated below.

In Fig. 4.17, the color contours represent the plasma potential with scale identical to Fig. 4.3, but now plotted above and below the axis. The horizontal axis has been transformed into real space with a Taylor hypothesis using the phase velocities measured from Fig. 4.2. This procedure importantly fails while the global plasma potential is fluctuating, as those fluctuations don't have a spatial gradient and shouldn't lead to electric fields. As the fluctuation is much smaller than the main V potential, it can be ignored for the purposes of this qualitative exercise.

In the upper half of Fig. 4.17, 10 particles are initialized at different radii with the same axial velocity, $v_0 = 100$ km/s. In the lower half, 10 particles are instantiated at the same radial location, but with an approximately thermal spread. From the lower plot, its apparent that thermal velocity plays an important role in which particles can cross the potential barrier. This plot counteracts the somewhat misleading upper plot which makes it appear as if all particles are deflected around the piston.

A much larger simulation with 10^5 total particles and a timestep of $1/100\omega_{ci}^{-1}$ can be quickly run to understand the phase space distributions. The result is plotted in Fig. 4.18. The red dashed lines from 1.45 to 1.65 m are approximately the region of the ion beam between the large and smaller potential peaks, where near the axis the electric field is close to 0. In between those lines, the total particle density exceeds 2.4 times the upstream density (average over all radii). Both the parallel and perpendicular temperatures show a strongly heated distribution, but still far below what's expected for a Hydro shock. We can estimate that with the fast shock condition that the downstream sound speed exceed the downstream flow speed, i.e. $v_{thi} \sim (u_{beam} - u_{piston}) \sim 48$ km/s in the lab frame, measured from Fig. 4.2. This predicts a downstream temperature of around 12 eV.

One important effect this qualitative study misses is the cyclotron resonant interaction between the reflected ions and the adjacent whistler waves, as this is an electromagnetic effect and this is a static simulation. The few particles that do exhibit reflection and reach $v_z = -u_p$ are precisely those most likely to resonate. The formation of "phase space vortices" from resonant interaction has been repeatedly observed in simulation, first by Biskamp [4] and nicely by Pantellini [87]. Given sufficient time, the growth of the leading

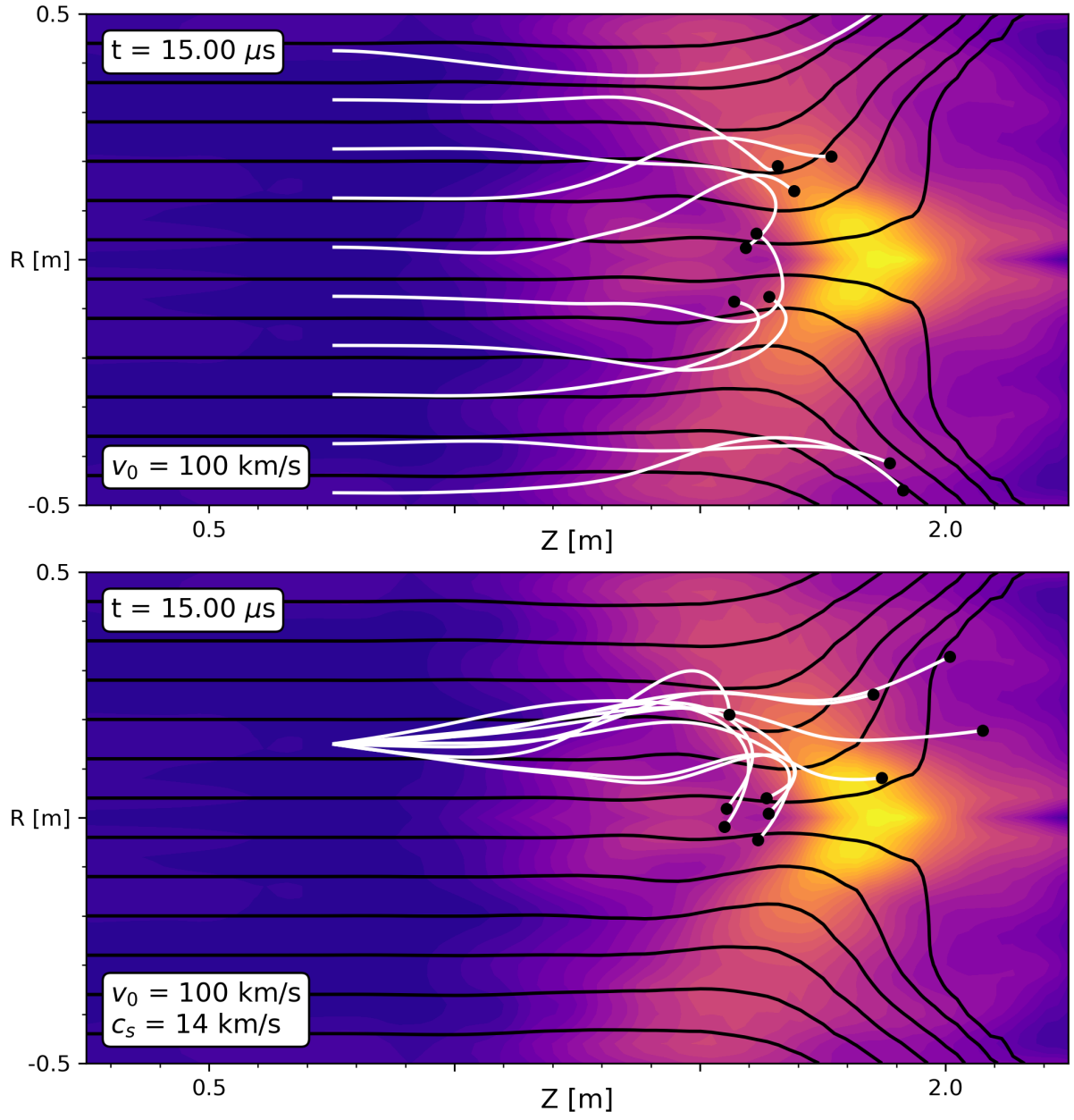

Figure 4.17: Above: Calculation of single particle trajectories given the measured electric and magnetic fields, in the reference frame of the piston. This assumes that the piston has a stationary shape for the duration, which we know to be true for only a short time. These particles are initialized with $\mathbf{fv} = 100\hat{z}$ km/s and varying initial radii. Note that at large radii, particles are deflected out of the way of the oncoming piston, while at lower radii particles are focused onto the axis. Below: to counteract the somewhat misleading nature of the upper plot, 10 particles with random initial thermal velocities are instantiated at the same radial location. Not all are reflected, which emphasizes the importance of gyrophase and thermal speeds to the reflection process.

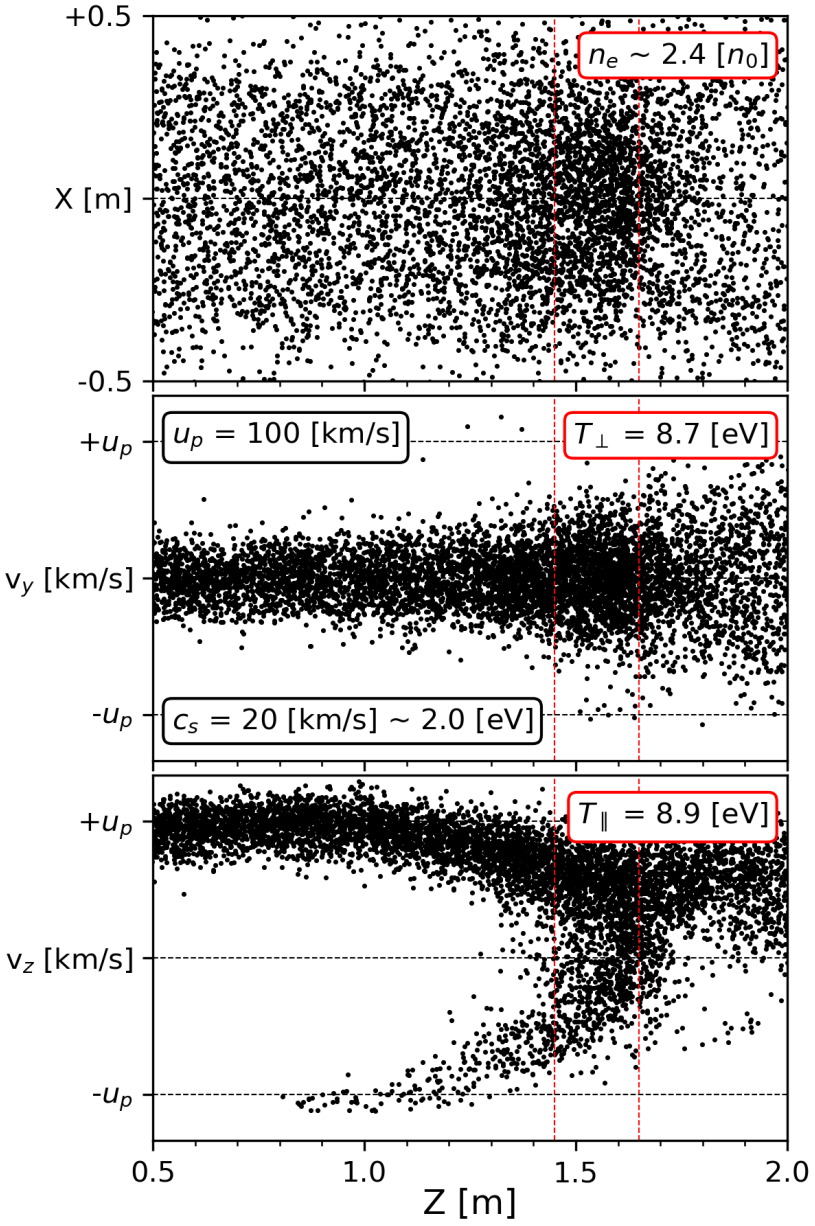

Figure 4.18: 1e5 particles are initialized with a radial and thermal distribution similar to the experiment but with an axial velocity at the piston speed (bottom) and then interact with the field profiles in Fig. 4.17. The top plot shows the focusing onto the axis and increased density, which within the red lines is 2.4 times the upstream density (and higher close to the axis). The middle and bottom plots show the perpendicular and parallel temperature of the beam between the red lines. While this is clearly heated above the 2 eV initial distribution, it remains far below the streaming kinetic energy (52 eV) of the 100 km/s ions.

whistler potential could do the same in the experiment.

5 SUMMARY AND CONCLUSIONS

The two shock experiments presented here cover the full range of parallel to perpendicular shocks, and the edges of the experiments provide opportunities to study the oblique and quasi-perp/par regimes. However, this work only investigates a relatively small region of Mach numbers, plasma betas, and collisionalities. Nonetheless, these are reasonable first attempts at producing collisionless shocks on the Big Red Ball vessel. These results should be used by a potential user of the WiPPL facility to understand what are the current capabilities of the BRB with respect to pulsed power shock experiments.

This final chapter has several goals. First, a comparison to more recent heliospheric shock observations will be made to emphasize the importance and limitations of these experimental results. The second section will outline a path towards producing magnetized perpendicular shocks, which were perhaps seen in Chapter 3 but obscured by an irreproducible target plasma. The final section asks what would it take to produce a fully collisionless laboratory plasma on the BRB.

5.1 Limitations of Comparisons to Heliospheric Shocks

In the introductory chapter, we discussed at length two mechanisms for collisionless dissipation of kinetic energy: ion reflection and dispersive electromagnetic whistler waves. Both of these dynamics were observed in each experiment. They are both also universally observed in heliospheric shocks: even at low Mach numbers, reflected ions [55, 49, 39] and dispersive whistler waves [119, 7] appear. It is not altogether surprising that they appear in our experimental work, too.

Reflection and dispersion are not the only dissipation mechanisms available to collisionless shocks: the de Hoffman-Teller frame cross shock potential [107], high frequency electric stochastic fields that demagnetize electrons [1, 117], and whistler associated electric fields [22] are other observed mechanisms specific to electron heating. Understanding these electron heating mechanisms is critical to understanding shock energy partition between species. However, both producing collisionless electrons and also measuring their distribution functions is a much more difficult challenge in the laboratory than in space.

The proposed avenues for further exploration, magnetizing the reflected ions and making the electrons collisionless, would both greatly increase the relevance of these experiments to naturally occuring collisionless shocks.

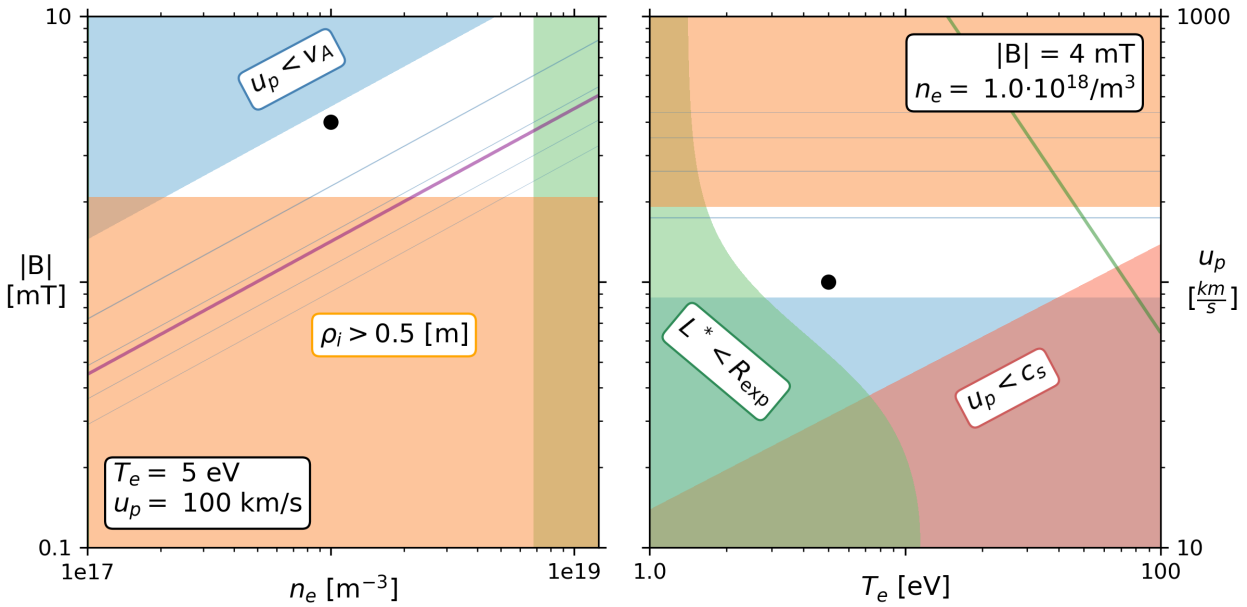

Figure 5.1: Magnetized Shock Experiment Parameter Space. The four parameters of density, magnetic field strength, temperature, and piston velocity make the 4D parameter space. Each plot is formed by fixing two of the parameters, as shown in the black text boxes and represented by the points on the opposite plot. The colored regions are the same between the two plots, and are explained in detail in the text.

5.2 Magnetized Perpendicular Shock Experiments

The features observed in the Theta Pinch experiments presented earlier were possible because of the weak ion magnetization, with ion Larmor radii larger than the experiment radius. Decreasing the Larmor radius such that $\rho_i \ll R_{exp}$ may allow a shock to form ahead of the piston. Being able to scan the Alfvén Mach number could allow investigation of the stability of collisionless perpendicular shocks, a subject still of great interest [72, 110, 67, 52, 58].

In the BRB experimental geometry, this is a difficult challenge. For a reflected ion speed of 130 km/s, a field of 4.0 mT is required to reduce the Larmor radius to 0.34 m, an arbitrary but reasonable value. While the BRB Helmholtz and mirror coils are capable of providing a background field of 6.8 mT with a mirror ratio $R_m = 10$, there are two problems: first, this is now a low-β mirror and is unstable to interchange mode, as has been discussed in Chapter 2, Section 3.17. Second, the Alfvén speed is now 87 km/s given a $1 \cdot 10^{18}$ m^{-3} density hydrogen plasma. That means that to drive a super-Alfvénic flow, our coils will need to produce >6.8 mT (1.1 kA in the drive coils) with a rise time much less than the Alfvén crossing time, $\tau_{rise} \ll R/v_A \sim 0.6$ μs. Our drive coils, with total inductance L~ 20 μH, would require a drive voltage of $V \gg L \cdot dI/dt \sim 20\mu H \cdot 1.1kA/0.6\mu s = 37$ kV. This is

beyond the BRB capabilities.

Of course, games can be played with increasing the plasma density and decreasing the Alfvén speed. Fig. 5.1 shows an exploration of the parameter space in density, temperature, magnetic field, and piston velocity. As this is a 4-D space, 2 parameters are held fixed for each plot; these are given in the black boxes and also by the black dots in the opposite plot. The white region in the center represents the area where all conditions necessary for a successful shock experiment are met. Substantial approximations have been made in order to make this plot, and it should be used pedagogically and not rigorously.

To examine this more carefully, the colored regions represent the same conditions for both plots. The blue region is where the piston velocity is sub-Alfvenic and thus no shock should form. The thin blue lines parallel to the edge of this region represent the $M_A = 2$, 3, 4, and 5 surfaces. Similarly, the red region represents where the piston is subsonic. Clearly, meeting this condition is much easier, as only for $T_e \sim 40$ eV does the sound speed exceed the Alfvén speed.

The final two regions are particular to the BRB experiments. The orange space represents convected ions with gyro-orbits too large to fit in the vessel:

$$\rho_i \equiv \frac{u_p}{\omega_{ci}} > 0.5 \text{ m} \tag{5.1}$$

With 0.5 m chosen such that $\rho_i \ll R_{exp}$. This is actually underestimating by a factor of 2, as the reflected ions also need to be magnetized. Properly calculating this moves the orange regions almost to the black dots. The green space represents the region where an ion stopping length is less than the BRB radius, and thus where collisional effects with the ions will be important. This has been calculated as described in Chapter 2.

The left hand plot also includes a single purple line which represents the $\beta = 1$ surface. Above this line plasmas are unstable to interchange, while below the line the plasma diamagnetically rearranges the field to reach a stable configuration. The successful theta pinch experiments were below this line in the orange region with gyroradii larger than the vessel.

Reaching the parameters chosen in Fig. 5.1 with current BRB equipment is not possible. While the plasma guns can reach high density, the high field collimates the plasma on axis, reducing the system size. Presented below are two ideas for reaching this higher magnetization state. The first is a new cold cathode system designed around the ring cusp system. The second is to optimize the existing ECRH heating for the vessel geometry, and is presented in the next section as it is critical to producing collisionless electrons.

BRB Helicity Injection Experiments

The problem with the current plasma gun injectors is that the on axis plasma source limits the radial extent of the experiment. One alternative scheme to produce a high density but low-β plasma is similar to an experiment long proposed for PCX and the BRB. Using paired rings of cold cathodes on adjacent magnet ring surfaces, a large current could be driven from ring to ring, producing a plasma that expands inwards and burps off plasmoids, similar to Peterson 2021 [94]. This has been termed Helicity Injection, as the helicity $\mathbf{J} \cdot \mathbf{B}$ can be easily controlled by swapping the direction of injected current. At lower currents where the detachment of plasmoids doesn't occur, this could still be a substantial source of plasma.

Prior experiments, particularly the dipole solar wind experiments run with E. Peterson mentioned above, have given lots of experience with discharges between cold electrodes in ambient plasma. Fig. 5.2 shows an image of the dipole magnet used for the solar wind experiments undergoing a high voltage test at atmosphere. Obvious "hot spots" lead to discrete structures of increased current density. When pulsed in a background plasma, such structures can be smeared out.

Such experience gives a level of confidence that a cold electrode discharge might prove tenable. Driving a discharge using a single PFN (or multiple in parallel) is trivial. The current densities for a mid latitude ring:

$$J = \frac{I}{2\pi R dr} = \frac{1\text{ kA}}{2\pi\ 0.5\text{ m}\ 1\text{ mm}} \sim 15\text{ A/cm}^2 \tag{5.2}$$

are a factor 50 greater than J_{sat}:

$$J_{sat} = n_i c_s = (10^{18}/\text{m}^3)(20\text{ km/s}) = 0.32\text{ A/cm}^2 \tag{5.3}$$

While this seems extreme, the current densities for the dipole experiment reached 150 kA/cm^2, and the hotspot density was likely an order of magnitude greater.

A possible design for the electrodes is shown in Fig. 5.3. The simplicity of such a plasma source in the BRB geometry is attractive. Using standard vessel ports, a simple high voltage isolating flange with a dual feedthrough would electrically connect the PFN outputs to electrodes on two adjacent magnet rings. The actual electrodes could be made of 304 Stainless steel or some similar alloy that is magnetic enough to be held in place by the magnets themselves. The much lower current densities suggest that stainless would last just fine.

The dipole configuration is also magnetically similar to the BRB cusp, with each elec-

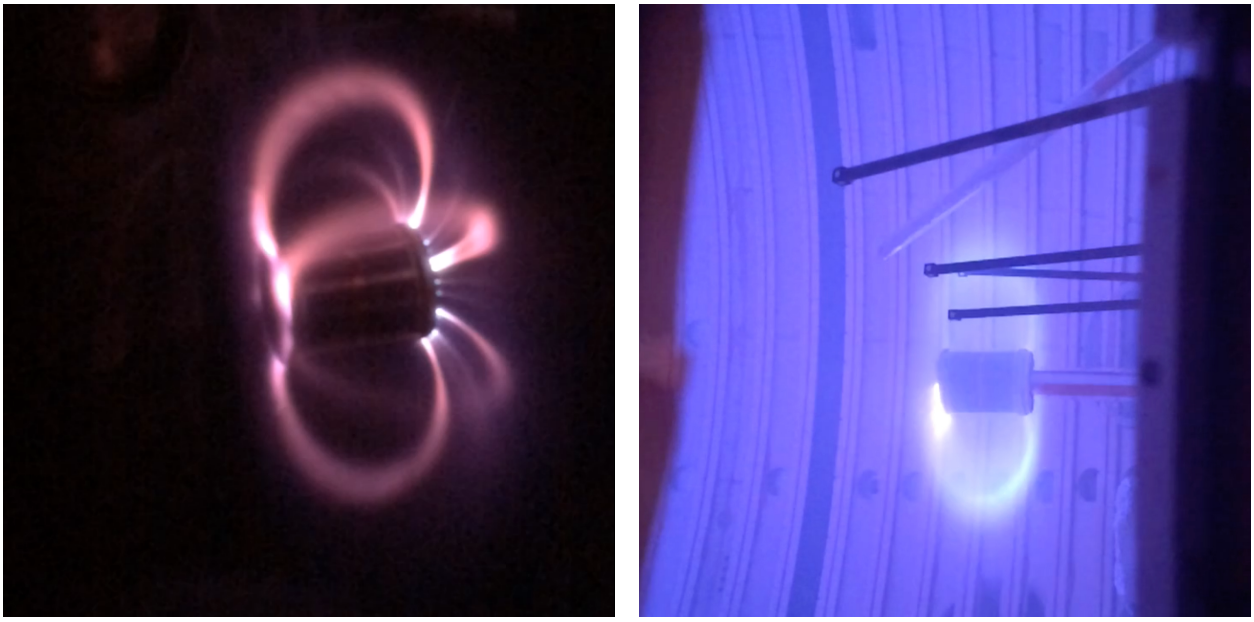

Figure 5.2: At left, image of a high voltage test of the BRB dipole magnet at low vacuum, 10 mTorr. The cylindrical samarium cobalt magnet at the center has two cold electrode rings on either pole. Here they are being energized with a 10 kV, low capacitance discharge. The image is visible emission taken with a cellphone camera, and the colors reflect the predominantly nitrogen atmosphere. Note the hot spots or arcs are discrete at one end (the negative polarity, electron emitting terminal) and more diffuse at the other (positive, electron collecting). At right, the BRB dipole magnet during a pulse. The dense background plasma was made with a LaB_6 cathode. Note how the hotspot is now smeared toroidally. In this configuration, both electrodes are raised to the same potential and biased to the grounded anodes elsewhere in the plasma. This causes strong $E \times B$ rotation of the arcs, smoothing them out.

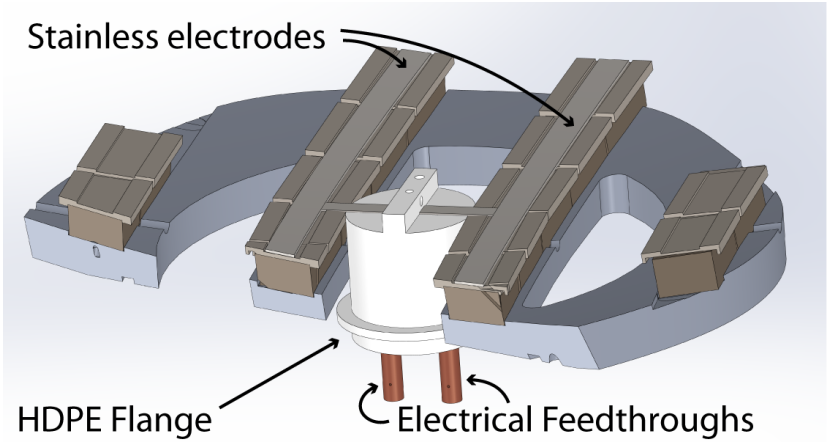

Figure 5.3: Possible design for a plasma source capable of more evenly fueling the BRB at large radii and high fields. Localized gas injection might be needed, instead of a uniform vessel fill, as neutral collisions could become significant.

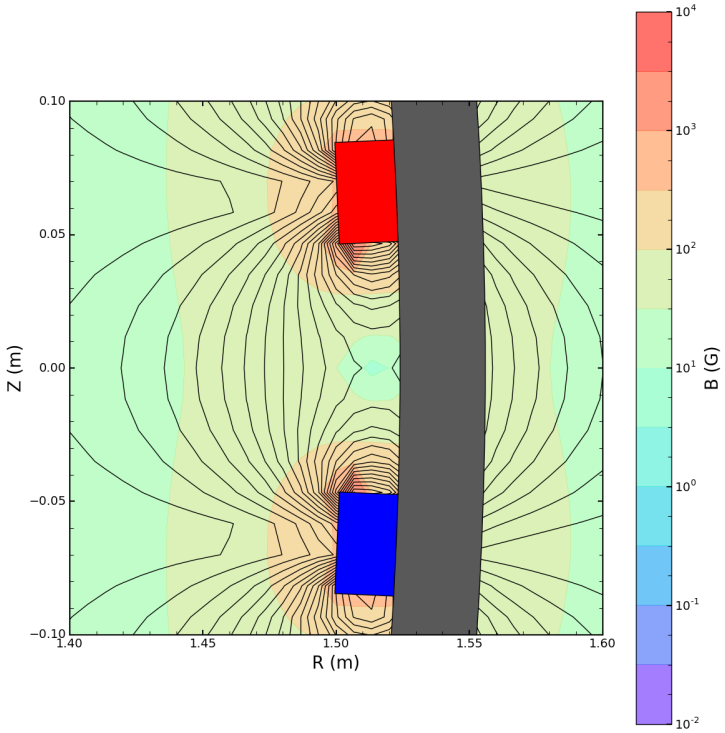

Figure 5.4: Cross section of the BRB magnetic cusp field. While the highest density plasma sits on the normal line centered on the magnet face, the shortest field lines connecting the magnets is close to the null between magnets. It's possible that a discharge might arc to the wall rather than following the plasma boundary.

trode located at the throat of a strong mirror field. However, as can be seen in Fig. 5.4, the geometry is different in that the shortest field lines between the two magnets actually pass near a magnetic null point. It may be necessary to have the conductor more carefully centered on the magnet surface than is depicted in Fig. 5.3 so that the breakdown along these field lines isn't possible. Or instead an insulating obstacle could be used.

The operating procedure for such an experiment should be simple: First, fill the vessel with sufficient neutral particles. Then, initiate a underdense plasma with a low power RF source. Once a plasma of reasonable density connects each electrode, pulse the PFNs. With an arrangement of PFNs as shown, the power density is roughly equally distributed between cylindrical shells. With 18 PFNs, the total power density is comparable to on axis experiments with 3 guns, and so similar densities (above $1 \cdot 10^{18}/\mathrm{m}^3$) could be possible.

5.3 Laboratory Shocks with Collisionless Electrons

The argument has been made by experimentalists that laboratory experiments can still be relevant even with high electron collisionality [89, 43]. However, for understanding how astrophysical collisionless shocks partition energy between species, having fully collisionless electrons is important so that collisions don't rapidly equilibrate the two species. The solar wind electron distribution function in particular can be categorized by a

thermal core, a hot halo, and a beam strahl, and the response of each of these populations to a shock layer need not be identical [117].

A recent review paper by Wilson, Chen, and Roytershteyn discusses the limitations of computational simulations in observing high frequency electrostatic waves in shocks [121]. Such electrostatic waves have, in recent decades, been recognized as being very important to controlling the electron heating in the shock layer [120, 22, 54]. A few of the earliest theta pinch experiments had success in observing high-frequency current driven electrostatic fluctuations [30, 69]. Those experiments, while dense, observed very hot electron temperatures and may have been properly collisionless. This past experimental work, combined with the motivation to support spacecraft observations, suggests that this may be a worthwhile pursuit.

Returning to Fig. 5.1, the single green line on the right hand plot shows the temperature and flow velocity necessary such that the electrons also are collisionless, i.e. $R_{exp}/u_p > \nu_e^{-1}$, or the electrons undergo only one collision in the experiment crossing time. This is more severe than is perhaps necessary. The electrons could be considered "collisionless" if they cross the shock layer in less than one collision time. Such a line is not included on the left plot, but would be a vertical line near $1.0 \cdot 10^{16}/m^3$. These two lines demonstrate just how difficult it is to produce a laboratory shock experiment with collisionless electrons.

The conditions are replotted in Fig. 5.5 for a different set of achievable plasma parameters. The colored regions are the same as before. While the location of the black dot is solidly within the orange region indicated unmagnetized ions, it remains supersonic and superAlfvénic with collisionless ions.

This choice of parameters of a $1 \cdot 10^{17}/m^3$ hydrogen plasma with a 15 eV electron temperature is the target. While hot, this is not an unreasonable target.

Upgraded ECRH

The BRB currently has four 2.45 GHz ECRH gyrotrons that could be installed on the vessel. Previous microwave experiments made a low density plasma that volumetrically fills the BRB even at high field. Above a density of $0.75 \cdot 10^{17}/m^3$, however, the plasma is overdense and the 2.45 GHz microwaves are directly reflected back into the waveguide. The lowest base pressure seen on the BRB in recent years was $7e-7$ torr, which at 25°C corresponds to a neutral particle density of $0.2 \cdot 10^{17}/m^3$. It would take some effort of conditioning to lower this density enough that a hydrogen plasma near the overdense threshold is not swamped with impurities.

J. Anderson's suggestion of launching the microwaves toroidally so that reflections

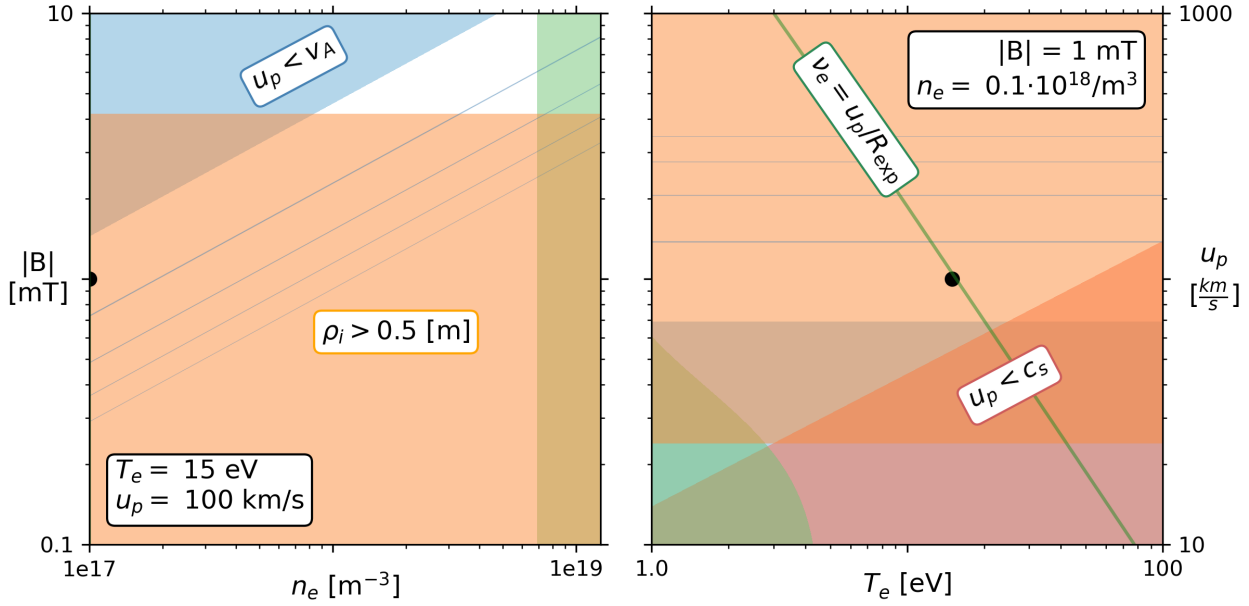

Figure 5.5: Similar to Fig. 5.1, these two plots show an attempt to make the electrons truly collisionless. Much hotter electron temperatures and much less dense plasmas make this technically possible. Unfortunately, at these densities the ion skin depth is 0.72 m. Since this scale sets the thickness of the ion reflection, the experiment will be very limited by the machine size. While it may be possible to achieve collisionless electrons, it likely won't happen simulatenously with magnetized ions (outstide of the orange region).

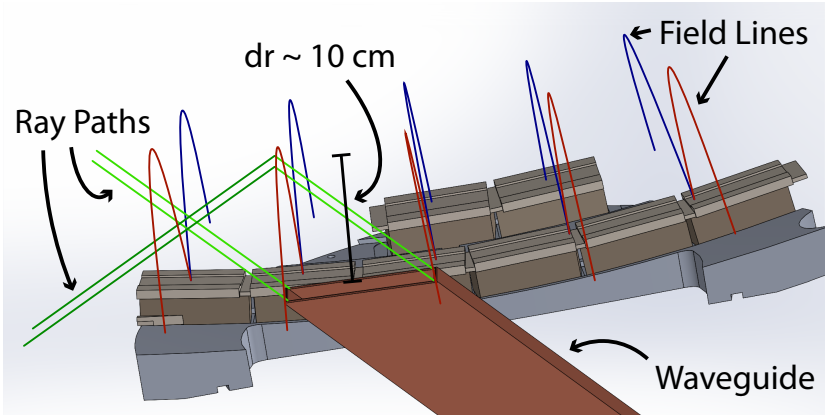

Figure 5.6: Proposed improvements to the ECRH system for BRB plasmas. A more tangential entrance angle will reduce reflections into the waveguide. It is expected that microwaves will bounce between the vessel wall and the cusp many times, before being absorbed by the plasma. As with all high power RF work, it is also possible that the strong microwaves in the gap between magnet rings will lead to unexpected arcing that makes implementation much more complicated.

bounce repeatedly between the plasma and the wall until they are eventually absorbed by the plasma may solve this problem. As the power supplies for the four gyrotrons exist, the largest barrier to implementing this is in manufacturing a horn capable of launching microwaves toroidally. This could be achieved either by physically tilting the waveguide through the a 16" flange, or by use of a dielectric with an angled exit and appropriate index of refraction. This concept is shown in Fig. 5.6.

Implementing this is a substantial amount of work. But, given a user with a strong scientific motivation to pursue shocks with collisionless electrons, it appears achievable.

A DERIVATION OF THE MHD RANKINE HUGONIOT SHOCK ADIABATIC

A.1 Motivation

This derivation of the shock adiabatic equation from the MHD Rankine-Hugoniot jump conditions is performed differently in many texts and resources [97, 42]. However, in none of those resources do they explicitly work out the derivation. I do so here partly for myself and partly as an aid to the future graduate student who wants to fully understand the problem. I hope one day it helps someone else, as a transcription error in writing the momentum equation made this take much longer than anticipated. Needless to say, I will never again mistake ram pressure ρv^2 in the momentum equation for flow energy $1/2 m v^2$.

A.2 Derivation

Let's begin by restating the problem: We seek a time-stationary solution to the MHD shock continuity equations across a discontinuity.

As before, suppose an infinite planar shock with shock normal $\hat{n}$ in the $\hat{x}$ direction. The upstream and downstream are homogeneous in the $\hat{y}$ and $\hat{z}$ directions. Let's also demand that both that $\hat{v}$ and $\hat{b}$ lie in a normal-transverse nt-plane, reducing our problem to 2.5 D. This will serve our goal of understanding the constraints imposed by conservation of mass, momentum, and energy, without wasting effort on a problem that is ultimately limited by the reliance on fluid closure.

Standing on the shoulders of giants as we are, we see that there exists a convenient reference frame in which to operate. Let's transform into a coordinate system moving at u_t along the $\hat{t}$ tangential direction such that the upstream $\hat{b}$ and $\hat{v}$ vectors are aligned:

$$\tan\theta_{bn} = \left(\frac{v_t + u_t}{v_n}\right) \tag{A.1}$$

This coordinate system, in which $\hat{v} \times \hat{b} = 0$ is known as the de Hoffman-Teller (dHT) frame. Transformations into this frame are routinely done in the analysis of spacecraft data. Note that, when $\theta_{bn} = \pi/2$, transforming into the dHT frame is impossible, as $\tan\theta_{bn} = \infty$. This is important to the theta-pinch, as at the experiment midplane θ is indeed $\pi/2$.

Now that we've defined our coordinate system, let's write out the equations we'll need.

Begin with Maxwell's equations:

$$\nabla \cdot \mathbf{E} = -\frac{\rho_q}{\epsilon_0} \qquad \nabla \times \mathbf{E} = -\frac{\partial \mathbf{B}}{\partial t} \tag{A.2}$$

$$\nabla \cdot \mathbf{B} = 0 \qquad \nabla \times \mathbf{B} = \mu_0 \mathbf{J} + \frac{1}{c^2}\frac{\partial \mathbf{E}}{\partial t} \tag{A.3}$$

Add the Ideal Ohm's Law equation:

$$\mathbf{E} + \boldsymbol{v} \times \mathbf{B} = 0 \tag{A.4}$$

Combine with Faraday's law A.2 above to yield the induction equation:

$$\nabla \times \boldsymbol{v} \times \mathbf{B} = \frac{\partial \mathbf{B}}{\partial t} \tag{A.5}$$

Restate the continuity equations for mass, momentum, and energy:

$$\frac{\partial \rho}{\partial t} + \nabla \cdot \rho \boldsymbol{v} = 0 \tag{A.6}$$

$$\frac{\partial \rho \boldsymbol{v}}{\partial t} + \nabla \cdot \mathbb{T} = 0 \tag{A.7}$$

$$\frac{\partial \mathcal{E}}{\partial t} + \nabla \cdot \mathbf{Q} = 0 \tag{A.8}$$

But now, unlike the simpler fluid case in Chapter 1, include the electromagnetic contributions in the definitions:

$$\rho = m n \tag{A.9}$$

$$P = n T \tag{A.10}$$

$$\mathbb{T} = \left(P + \frac{B^2}{2\mu_0}\right)\mathbb{1} + \frac{\rho \boldsymbol{v}\boldsymbol{v}}{2} - \frac{\mathbf{B}\mathbf{B}}{\mu_0} \tag{A.11}$$

$$\mathcal{E} = \frac{\rho v^2}{2} + \frac{P}{\gamma - 1} + \frac{B^2}{2\mu_0} \tag{A.12}$$

$$\mathbf{Q} = \left(\frac{\rho v^2}{2} + \frac{\gamma}{\gamma - 1} P\right)\boldsymbol{v} + \frac{\mathbf{B} \times (\boldsymbol{v} \times \mathbf{B})}{\mu_0} \tag{A.13}$$

Note that the last term in the energy flux $\mathbf{Q}$ is a reformulation of the Poynting flux using Ideal MHD.

In such a form, the continuity equations can again (as in Chapter 2) be solved via integration. Next, choose a rectangular fluid cell that straddles the shock layer and integrate

over the volume.

$$\int_\tau \left(\frac{\partial \rho}{\partial t} + \nabla \cdot \rho \boldsymbol{v}\right) d\tau = 0 \tag{A.14}$$

With the same application of Gauss' law as the hydro case:

$$\int_\tau \nabla \cdot \rho \mathbf{v}\ d\tau = \oint_\sigma \rho \boldsymbol{v} \cdot \hat{n}\ d\sigma = 0 \tag{A.15}$$

To the three continuity equations, Gauss' law for magnetism, and the induction equation, we get the following 6 Rankine-Hugoniot jump conditions for MHD discontinuities:

$$\Big[\ \rho v_n\ \Big]_d^u = 0 \tag{A.16}$$

$$\left[P + \rho v_n^2 + \frac{B_t^2}{2\mu_0}\right]_d^u = 0 \tag{A.17}$$

$$\left[\rho v_t v_n - \frac{B_t B_n}{\mu_0}\right]_d^u = 0 \tag{A.18}$$

$$\left[\left(\frac{\rho |v|^2}{2} + \frac{\gamma}{\gamma - 1} P\right) v_n + \frac{B_t}{\mu_0}\left(v_n B_t - v_t B_n\right)\right]_d^u = 0 \tag{A.19}$$

$$\Big[\ B_n\ \Big]_d^u = 0 \tag{A.20}$$

$$\Big[\ v_n B_t - v_t B_n\ \Big]_d^u = 0 \tag{A.21}$$

Henceforth we will replace the downstream 'd' subscript with primed ($'$) superscripts and leave the upstream variables naked. As before, we can define the compression ratio δ, the sound speed c_s, and the Mach number M_s. To this we will add the Alfvén speed v_A and the Alfvénic Mach number M_A, and β:

$$\delta \equiv \frac{\rho'}{\rho} \qquad \beta \equiv \frac{c_s^2}{v_A^2}$$

$$c_s \equiv \left(\frac{\gamma P}{\rho}\right)^{1/2} \qquad M_S \equiv \frac{v}{c_s}$$

$$v_A \equiv \left(\frac{B^2}{\mu_0 \rho}\right)^{1/2} \qquad M_A \equiv \frac{v}{v_A}$$

Note also that there is a small problem with the way that the coordinate system and the angle θ_{bn} have been defined. While we can use the magnetic field or velocity vectors to find θ, using θ to find the vectors will yield a sign ambiguity. This won't ultimately be a problem.

Our goal is an equation for the shock speed. Let's examine our equations step by step. Most obvious is the divergence free nature of B in A.20:

$$\frac{B_n'}{B_n} = 1 \tag{A.22}$$

Having defined δ, A.16 yields:

$$\frac{v_n'}{v_n} = \frac{1}{\delta} \tag{A.23}$$

From the cross shock transport of tangential momentum equation A.18, and using the dHT reference frame condition $v_n' B_t' - v_t' B_n' = 0$:

$$v_t v_n - \frac{B_t B_n}{\mu_0 \rho} = v_t' \left(v_n - \frac{\delta B_n^2}{v_n \mu_0 \rho} \right) \tag{A.24}$$

$$v_t^2 - v_A^2 \sin^2\theta = \frac{v_t'}{v_t} \left(v_t^2 - \delta v_A^2 \sin^2\theta \right) \tag{A.25}$$

$$\frac{v_t'}{v_t} = \frac{\left(v_n^2 - v_A^2 \cos^2\theta \right)}{\left(v_n^2 - \delta v_A^2 \cos^2\theta \right)} \tag{A.26}$$

Then using A.21 again and solving for B_t':

$$B_t' = \frac{v_t'}{v_n'} B_n = \delta B_t \frac{v_t'}{v_t} \frac{\tan\theta}{\tan\theta} \tag{A.27}$$

$$\frac{B_t'}{B_t} = \delta \frac{\left(v_n^2 - v_A^2 \cos^2\theta \right)}{\left(v_n^2 - \delta v_A^2 \cos^2\theta \right)} \tag{A.28}$$

And finally, the ratio of the pressures using the above and A.17

$$P' = P + \rho v_n^2 \left(1 - \frac{1}{\delta} \right) + \frac{\rho}{2} v_A^2 \sin^2\theta \left(1 - \delta^2 \frac{\left(v_n^2 - v_A^2 \cos^2\theta \right)^2}{\left(v_n^2 - \delta v_A^2 \cos^2\theta \right)^2} \right) \tag{A.29}$$

$$\frac{P'}{P} = 1 + \frac{\gamma v_n^2}{c_s^2} \left(\frac{\delta - 1}{\delta} \right) - \frac{\gamma}{2} \frac{v_n^2 v_A^2 \sin^2\theta}{c_s^2} (\delta - 1) \frac{v_n^2 (\delta + 1) - 2\delta v_A^2 \cos^2\theta}{\left(v_n^2 - \delta v_A^2 \cos^2\theta \right)^2} \tag{A.30}$$

Our remaining unused equation A.19 simplifies considerably when we recognize that in the dHT frame, $v_n B_t - v_t B_n = 0$. Rearranging eq. A.19:

$$\frac{\rho}{2} (v^2 - v'^2) + \frac{\gamma}{\gamma - 1} \left(P - \frac{P'}{\delta} \right) = 0 \tag{A.31}$$

Removing the $v^2 - v'^2$ term is tricky:

$$v^2 - v'^2 = \frac{v_n^2}{\cos^2\theta} - \frac{v_n'^2}{\cos^2\theta'} = v_n^2\left(1+\tan^2\theta\right) - \frac{v_n^2}{\delta^2}\left(1+\tan^2\theta'\right) \tag{A.32}$$

Where $\tan\theta'$ can be expressed as:

$$\tan\theta' = \frac{v_t'}{v_n'} = \delta\tan\theta\frac{v_n^2 - v_A^2\cos^2\theta}{v_n^2 - \delta v_A^2\cos^2\theta} \tag{A.33}$$

And so A.32 becomes:

$$\left(v^2 - v'^2\right) = v_n^2\left(1+\tan^2\theta\right) - \frac{v_n^2}{\delta^2}\left(1+\delta^2\tan^2\theta\frac{\left(v_n^2 - v_A^2\cos^2\theta\right)^2}{\left(v_n^2 - \delta v_A^2\cos^2\theta\right)^2}\right) \tag{A.34}$$

$$= v_n^2\left[\left(\frac{\delta^2-1}{\delta^2}\right) + \tan^2\theta\left(1 - \frac{\left(v_n^2 - v_A^2\cos^2\theta\right)^2}{\left(v_n^2 - \delta v_A^2\cos^2\theta\right)^2}\right)\right] \tag{A.35}$$

$$= v_n^2\left[\left(\frac{\delta^2-1}{\delta^2}\right) + \tan^2\theta\left(v_A^2\cos^2\theta(\delta-1)\frac{\left((\delta+1)v_A^2\cos^2\theta - 2v_n^2\right)}{\left(v_n^2 - \delta v_A^2\cos^2\theta\right)^2}\right)\right] \tag{A.36}$$

$$= v_n^2(\delta-1)\left[\left(\frac{\delta+1}{\delta^2}\right) + v_A^2\sin^2\theta\frac{\left((\delta+1)v_A^2\cos^2\theta - 2v_n^2\right)}{\left(v_n^2 - \delta v_A^2\cos^2\theta\right)^2}\right] \tag{A.37}$$

Now, insert our expression for $(v^2 - v'^2)$ and for P' into equation A.31.

$$\begin{aligned} 0 = {} & \frac{\rho}{2}\left[v_n^2(\delta-1)\left[\left(\frac{\delta+1}{\delta^2}\right) + v_A^2\sin^2\theta\frac{\left((\delta+1)v_A^2\cos^2\theta - 2v_n^2\right)}{\left(v_n^2 - \delta v_A^2\cos^2\theta\right)^2}\right]\right] \\ & + P\frac{\gamma}{\gamma-1}\left[\left(\frac{\delta-1}{\delta}\right) - \frac{\gamma}{\delta}\frac{v_n^2}{c_s^2}\left(\frac{\delta-1}{\delta}\right) + \frac{\gamma}{2\delta}\frac{v_n^2 v_A^2\sin^2\theta}{c_s^2}(\delta-1)\frac{\left((\delta+1)v_n^2 - 2\delta v_A^2\cos^2\theta\right)}{\left(v_n^2 - \delta v_A^2\cos^2\theta\right)^2}\right] \end{aligned} \tag{A.38}$$

Replace any outstanding P, B, or ρ with c_s, v_A, and δ, and factor out the $(\delta-1)$ term.

$$\begin{aligned} 0 = {} & (\gamma-1)v_n^2\left[\left(\frac{\delta+1}{\delta^2}\right) + v_A^2\sin^2\theta\frac{\left((\delta+1)v_A^2\cos^2\theta - 2v_n^2\right)}{\left(v_n^2 - \delta v_A^2\cos^2\theta\right)^2}\right] \\ & + \left[\frac{2c_s^2}{\delta} - \frac{2\gamma v_n^2}{\delta^2} + \frac{\gamma}{\delta}v_n^2 v_A^2\sin^2\theta\frac{\left((\delta+1)v_n^2 - 2\delta v_A^2\cos^2\theta\right)}{\left(v_n^2 - \delta v_A^2\cos^2\theta\right)^2}\right] \end{aligned} \tag{A.39}$$

Group the $\sin^2\theta$ terms and multiply by the common denominator:

$$0 = \left[(\gamma-1)v_n^2\left(\frac{\delta+1}{\delta^2}\right) + \frac{2c_s^2}{\delta} - \frac{2\gamma v_n^2}{\delta^2}\right]\left(v_n^2 - \delta v_A^2\cos^2\theta\right)^2 + v_n^2 v_A^2\sin^2\theta\left[(\gamma-1)\left((\delta+1)v_A^2\cos^2\theta - 2v_n^2\right) + \frac{\gamma}{\delta}\left((\delta+1)v_n^2 - 2\delta v_A^2\cos^2\theta\right)\right] \quad (A.40)$$

Almost finished. Multiply by δ^2, and arrange the second term by v_n^2 and $\delta v_A^2\cos^2\theta$:

$$0 = \left[v_n^2\left[(\gamma-1)(\delta+1) - 2\gamma\right] + 2\delta c_s^2\right]\left(v_n^2 - \delta v_A^2\cos^2\theta\right)^2 - \delta v_n^2 v_A^2\sin^2\theta\left[v_n^2\left[\gamma(\delta+1) - 2\delta(\gamma-1)\right] - \delta v_A^2\cos^2\theta\left((\gamma-1)(\delta+1) - 2\gamma\right)\right] \quad (A.41)$$

A.3 Discussion

Equation A.41 is the MHD Rankine-Hugoniot Shock Adiabatic equation. It's not obvious at first, but in the incompressible limit $\delta \to 1$ it simplifies considerably.

$$0 = \left[v_n^2 + c_s^2\right]\left(v_n^2 - v_A^2\cos^2\theta\right)^2 - v_n^2 v_A^2\sin^2\theta\left[v_n^2 - v_A^2\cos^2\theta\right] \quad (A.42)$$

The first solution is clearly $v_n^2 = v_A^2\cos^2\theta$, also known as an Intermediate or Shear Alfvén wave. The remaining equation is quadratic in v_n^2 and yields two solutions for v_n^2:

$$v_n^2 = {}^1\!/_2\left(v_A^2 + c_s^2 \pm \sqrt{\left(v_A^2 + c_s^2\right) - 4c_s^2 v_A^2\cos^2\theta}\right) \quad (A.43)$$

Known as the Fast $(+)$ and Slow $(-)$ waves, these MHD wave speeds are plotted in the polar Friedrich plots in Fig. 2.5 for three particular values of β.

This is a truly lovely result, but it rests on an assumption that is often temporarily broken. It demands that both the upstream and downstream are Maxwellian (maximal entropy) distributions, and in the shock layer some powerful entropy generating process (particle collisions) maintains this state throughout. It ignores the possibility of other non-Maxwellian states able to satisfy the continuity equations.

For example, a discontinuity at the interface of two cold counterstreaming beams created by perfect reflection off of wall has a compression of $\delta = 2$ and satisfies (in a kinetic formalism) the mass, momentum, and energy continuity equations. While this is a trivial solution, it is quite easily produced in the laboratory as seen in Chapters 2 and

3. The beauty of this derivation, imho, delayed the recognition of the important kinetic processes in laboratory experiments by attempting to interpret the results in terms of Fast, Intermediate, and Slow mode shocks.

Despite what I intoned above, the limits of these equations were quickly recognized. This led to the proliferation of "critical Mach numbers." The first critical Mach number acknowledged that, if the entropy is generated by electron-ion collisions (i.e., resistively), then the current J in the layer heats the plasma via Ohmic heating ηJ. But now there is a paradox: the total J (and thus total heating) is set by Maxwell's equations and the jump in B, which in the strong shock limit caps at $\delta = 4$. But since the plasma pressure increases without bound, there must be some point where the current can no longer supply the heating required. At this point, some other dissipative mechanism must appear, and often that is ion reflection.

Second critical Mach number where the downstream flow speed v_n' is equal to the downstream sound speed c_s'.

A third critical Mach number above which even ion reflection fails. [70]

B COMPACT TOROID INJECTOR

B.1 Summary

This appendix outlines the substantial work that was done to design and improve the BRB Compact Toroid Injection (CTI). Basic operating procedures are not included here. Instead, this section documents many tough experimental lessons that were learned the hard way.

B.2 Introducing the CTI to the BRB

In the spring of 2016, Tri-Alpha Energy (now TAE Technologies) shipped a Magnetized Coaxial Plasma Gun (MCPG) or Compact Toroid Injector (CTI) to the BRB lab in Madison. TAE developed CTIs to refuel their Field Reversed Configuration (FRC) plasmas without the strong cooling effect of pellet injection. The CTI launches a fully ionized plasmoid fast enough to penetrate the strong fields surrounding the FRC [78]. This plasmoid is often also called a compact toroid (CT) or a spheromak as it contains both poloidal and toroidal fields [51]. While the CT can be idealized as axisymmetric, in the BRB geometry it is free to expand, tilt, and relax to a twisted state [27]. The overall irreproducibility of the BRB CT magnetic signals suggests that those components become mixed as it begins tumbling or twisting.

The CTI operates as a magnetic railgun. As the current flows down the center conductor, through the plasma, and back through the outer conductor, the plasma in the gun barrel is accelerated by the $J_r \times B_\phi$ MHD force. When poloidal bias field is present, those fields are stretched until they reconnect and the CT detaches from the barrel. It is equally valid to consider the magnetic pressure of the piston balancing against the ram and internal pressure of the plasma. Either way, since both the current density J_r and toroidal magnetic field in the barrel B_ϕ depend on the total current I, maximizing I is a goal.

At the BRB, it took time to integrate the TAE-CTI with the BRB control systems and to learn to operate the HV pulsed power system. In parallel, we began developing our own version specific for the BRB that would enable us to perform CT collision experiments. As of the publication of this document, the original TAE-CTI has been returned, and a second BRB-CTI is nearing completion. The following sections will cover the control systems, the pulsed power set-up, and the pre-ionization system with sufficient detail for WiPPL users to reference.

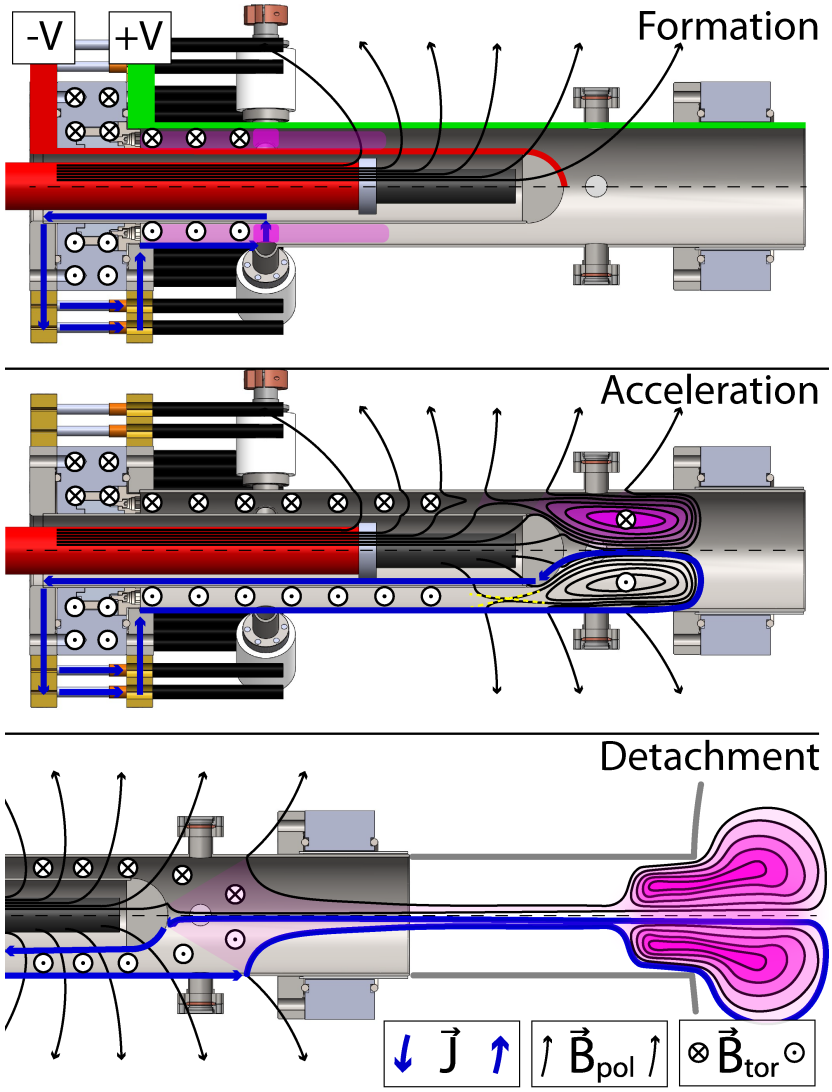

Figure B.1: Cross section of the magnetized coaxial plasma gun barrel during the formation, acceleration, and detachment of the CT. The diffuse plasma in the barrel from the PI system is sufficient that as voltage is applied to the inner conductor, current immediately begins flowing. All of the neutrals in the barrel become ionized from the intense UV. The plasma is accelerated down the barrel by the J×B force and sweeps up the poloidal bias flux, which reconnects as the CT moves past (the dashed yellow lines show the site of reconnection). Detachment occurs when all of the poloidal flux reconnects, and the current path is broken. If substantial current is still flowing in the circuit, a large inductive voltage spike will occur, and a second breakdown arc may appear where neutrals are injected into the breech.

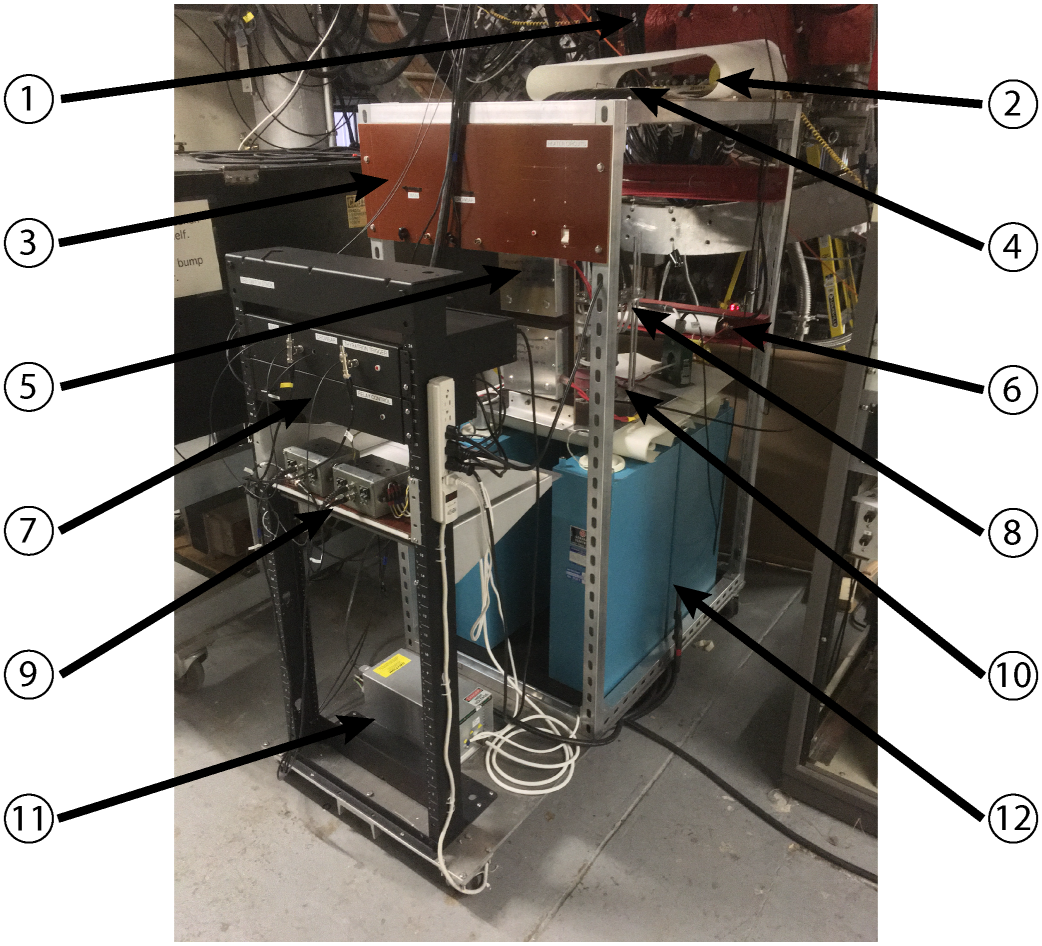

Figure B.2: Image of the CTI cart in position below the BRB. (1) HV transmission line. (2) Transmission Breakout panel. (3) Thryatron heater control circuit. (4) Breakout cables. (5) HV pulse transformers. (6) High impedance Pre-Ionization resistor. (7) Control boxes. (8) Crowbar Thyratron. (9) Puff valve trigger boxes. (10) Main Thyratron. (11) TDK-Lambda 1.5 kW, 20 kV negative polarity power supply. (12) Capacitor Bank, 5× 14 μF General Electric capacitors.

B.3 Improving the Pulsed Power Circuitry for the BRB

As mentioned, maximizing the total current I is essential to good CT performance. For the required fast turn on time and large currents, this demands that we minimize inductance. Fig. B.3 represents the pulsed power circuit, with the switch stack connected to the breakout, the transmission line, and finally the load. All of the extra resistance and inductance outside of the load is deleterious and reduces overall efficiency.

To improve gun performance, much work was done to shorten transmission lines, increase the number of cables/conducting rods, and redesign the CT itself. The TAE CTI was designed for operation on the C2-U vessel which necessitated long tranmission line and

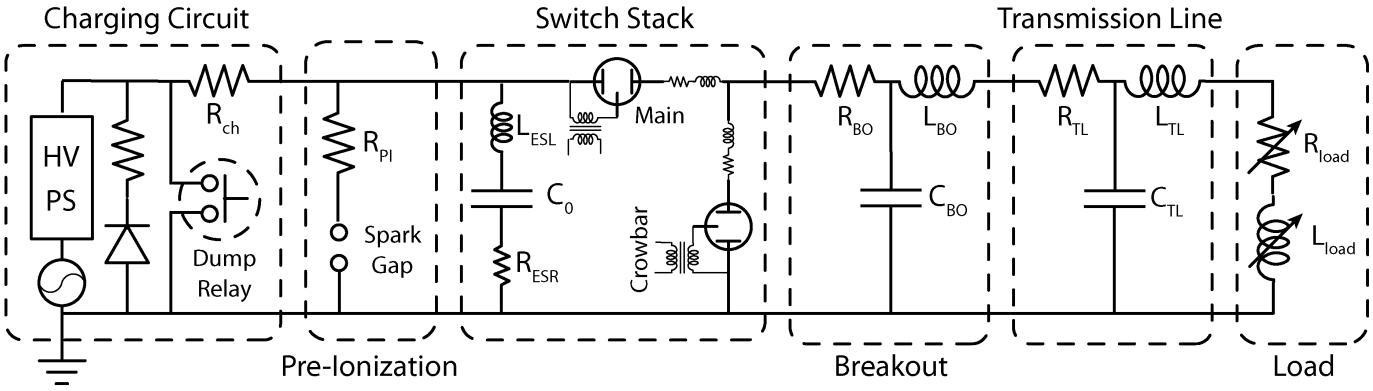

Figure B.3: Circuit diagram of the charging and pulsed power system. The variable load inductance can be modeled as the fixed inductance from the breech $L_{br}$and the variable inductance from the current path through the plasma L_{pl}. The variable resistance can be neglected if the pre-ionization coronal discharge produces consistent plasma in the spark gap.

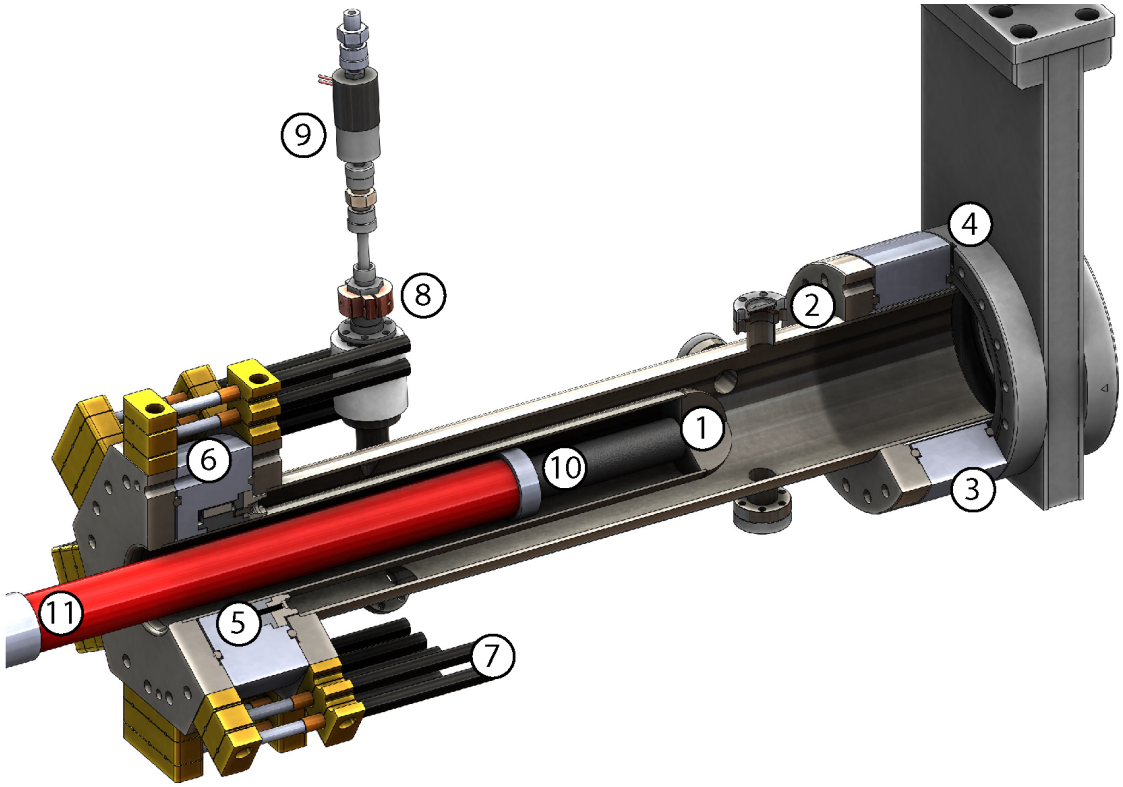

Figure B.4: Cross section of the BRB CTI. (1) Tungsten coated center conductor. (2) Stainless steel outer conductor. (3) High Density Poly-Ethylene (HDPE) Isolating flange. (4) Gate Valve. (5) Ceramic breech. (6) HV HDPE Breech. (7) HV transmission lines. (8) Old Pre-ionization gun. (9) Gas puff valve. (10) Iron Core. (11) Solenoid.

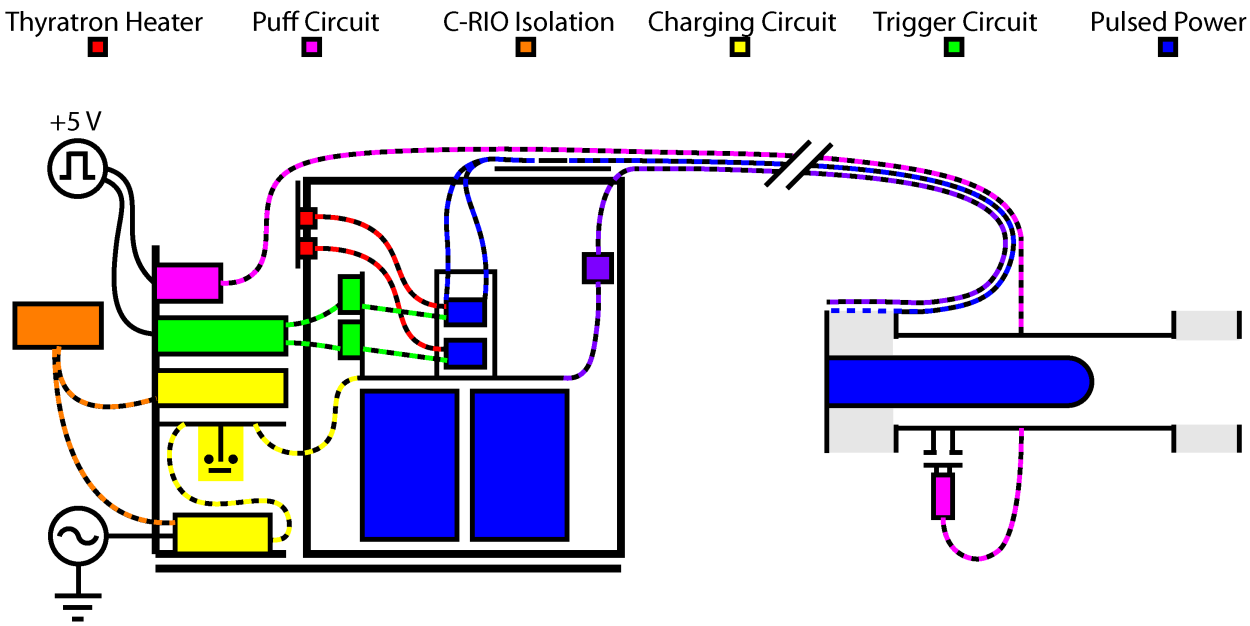

Figure B.5: Overall diagram of the Compact Toroid Injector system. Drawing not to scale. Signals from the C-RIO are isolated before going to the charging or trigger circuits. Ground is provided locally by the TDK-Lambda High Voltage Power Supply.

		TAE^{old}	TAE^{new}	BRB
Capacitor	C_0, μF	124	70	70
	L_{ESL}, nH	50	20	20
Switch Stack	L	75	75	60
Breakout	L	30	30	11
Trans. Line	L	30	30	16
Gun Breech	L	40	40	10
Total Fixed	L	225	195	120
	R, mΩ	2	2	2
Plasma	L	25+	25+	25+
$\tau_{1/4}$	μs	8.3	5.8	4.6
τ_{obs}	μs	8.5	6.0	4.0

Table B.1: Values of various parts of the CTI circuit showing the improvements from the TAE to the BRB version.

rigorous vacuum standards. The BRB, with its must less stringent vacuum requirements, can afford to use plastic flanges and O-rings where TAE can not. The large and expensive commercial high voltage standoffs used in the TAE CTI were replaced with much cheaper and lower inductance high-density polyethlene blocks. The table B.1 shows estimates of this and other improvements.

The measured performance improvement between the TAE and BRB CTIs reflects these

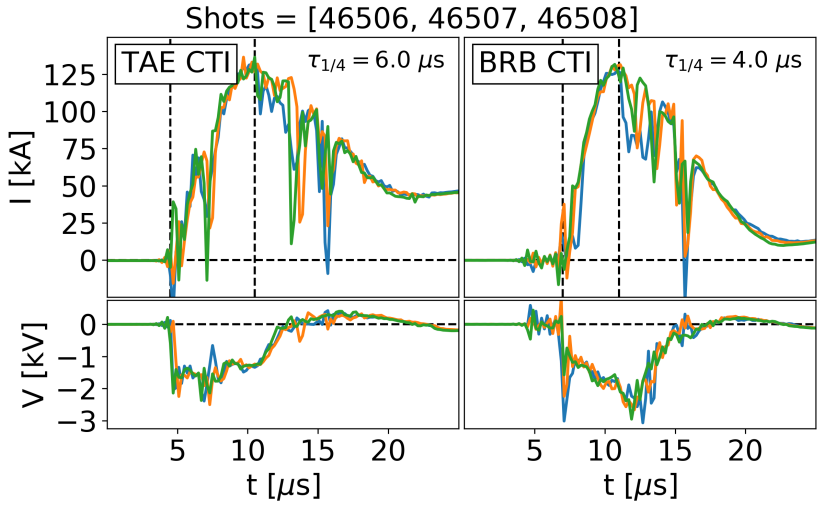

Figure B.6: Typical current traces for three consecutive firings of the TAE and BRB CTIs. For these shots, the cap bank voltages were 10 and 9 kV, respectively. Prior to these shots, the TAE cap bank capacitance had been decreased from 125 to 70 µF. The vertical lines show the rise times, which suggest total inductances of 210 and 95 nH, demonstrating the large improvements made on the BRB CTI. The voltage measurements were made with a Pearson current transformer around a 10 kΩ resistor across the breech, and show the increased voltage at the barrel and thus improved power transfer to the plasma. This measurement can no longer be made with the new PI system as it would drain the capacitor while it is charging. Note the large disruptions in the current around 15 µs. The dI/dt is around 500 kA/µs, which should produce voltages of $L dI/dt = 100$ kV, clearly unreasonable. This is believed to be instead a capacitive coupling effect from the Ion Physics brand current transformers that is picked up by the non-differential measurement. It may nonetheless correspond with significant events, such as detachment of the CT from the barrel.

values. A relevant number of import for operation of the CT is the quarter-wave rise time, $\tau_{\frac{1}{4}}$. This is the time at which the current peaks and the capacitor is fully discharged. It also sets the timing between the Main and Crowbar triggers, so that the crowbar properly diverts current from ringing the capacitor.

When the LC resonant frequency is $\omega_{LC} = (LC)^{-1/2}$, then $\tau_{\frac{1}{4}} = (2\pi\sqrt{LC}/4)$. Using only the fixed values of inductance and capacitance from Table B.1, the TAE and BRB rise times $\tau_{\frac{1}{4}}$ are at minimum 8.3 and 4.5 µs. For comparison, the TAE CTI was operated with a main-crowbar delay of 10 µs, while the BRB CTI operates with 5 µs. These improvements also allow the BRB CTI to be operated at lower capacitor voltages (8 versus 10 kV) to achieve the same 100 kA of current.

Unidentified Current Disruptions on the BRB CTI

Quite often, the BRB CTI registers a current disruption, shown in Fig. B.6. This disruption has been measured separately with both Pearson current transformers and integrated Rogowski coils and is believed to be real. The enormous dI/dt leads to a very substantial voltage spike due to the total inductance L. This could be due to the reconnection processes happening as the CT detaches from the gun, or from a instability rapidly increasing the resistance of the plasma (as occurs in a Dense Plasma Focus).

We can gain some insight into this if we very crudely estimate the acceleration of the CT down the barrel. Let's assume that the acceleration of the CT only occurs as the current peaks and approximate this peak as a square pulse of width 5 μs, meaning a constant acceleration. To reach the 100 km/s in 5 μs at constant acceleration means the CT has traveled 25 cm during this period. For reference, the CTI barrel length is 30 cm.

While not intending to be accurate, this suggests that the CT acceleration is reasonably matched to the barrel length. If detachment occurs as naively drawn in Fig. B.1, then perhaps this is responsible for the disruption. However, fast camera images reveal current rope structures attached to the gun that extend into the chamber, which is roughly 35 cm past the tip of the inner conductor. From earlier, fig. 4.12 shows what might be a kinked current rope structure which could be responsible for a sudden increase in plasma impedance. The upgrade of the BRB timing system will allow these images to be properly synced with the current and perhaps discriminate between these two mechanisms.

Current Limits on Pulsed Power Capacitors

Generally, pulsed power capacitors are labeled with values of import, namely the measured capacitance, voltage limits, equivalent series inductance, and whether it contains carcinogenic oil. Unfortunately, it is not standard practice to include the capacitor's rated operating current on the label. This learning curve was unforgiving.

The original capacitor from TAE was a Maxwell Labotaries Series C Model 32235 with a rating of 50 kA. In operating the capacitor at a nominal current of 100 kA, we were pushing the limits. After several shots attempting faster CTs at I=150 kA, the capacitor ruptured and had to be discarded. However, at the time it wasn't recognized that the failure was from exceeding the rated current. It was replaced with smaller 50 uF capacitors that ultimately suffered the same fate: the magnetic forces from the large currents internally tore the thin capacitor foil structure. While there was no catastrophic failure, the discharge current decreased noticeably in consecutive shots.

The current capacitor bank is parallel array of 5 General Electric series 30F1100 capacitors.

Series	30F1100
Rating	25 kV DC
C	14 uF -0/+10 %
T-C Test	41 kV - 60 s
T-T Test	40 kV - 60 s
L_{ESL}	100 nH
Discharge Type	Undamped Ringing
Percent Reversal	85%
Peak Current	30 kA
Ringing Frequency	40 kHz
Duty Cycle	5 - 10 minutes
Expected Lifetime	100,000 discharges

Table B.2: Parameters received from GE records on the original ratings for the capacitors currently used on the BRB CTI.

These were custom built for the University of Washington's Large "S" Experiment (LSX) in the early 90s exploring high Lundquist numbers (hence the S). According to scientists at the university, the capacitors "are over designed and under spec'd", and have been individually rung at 100 kA without failure. Table B.2 shows the ratings provided by GE, which state a rated peak current of 30 kA. The current set up is rated to 150 kA, but based on the U.Wash experience could be operated much higher without failure.

B.4 Preionization System

The original TAE CTI system had no preionization (PI) system. Instead, a large parallel inductor served as a load until an arc formed in the neutral gas in the barrel. While this rarely failed completely, the large jitter in formation was unacceptable for experiments involving collisions of CTs where the timing must be precisely controlled so that the fast moving CTs collide at a specific location.

Working to improve gun performance, TAE developed a mini magnetized coaxial plasma gun and used two of these mini guns to symmetrically inject plasma into the breech [37]. These guns enabled operation at lower neutral densities, increasing CT speed and temperature.

Other coaxial plasma guns also use pre-ionization systems. The guns developed by Hyper-V for the Los Alamos based Plasma Liner Experiment (PLX) had substantial preionization, with a ring of 32 pins each with series 8 Ω resistance switched onto a 35 kV, 0.6 μF capacitor bank [122]. To the BRB CTI system, a single washer gun with standard 100 kW, 10 ms PFN was added. While this worked, gun reliability was not ideal. In comparison,

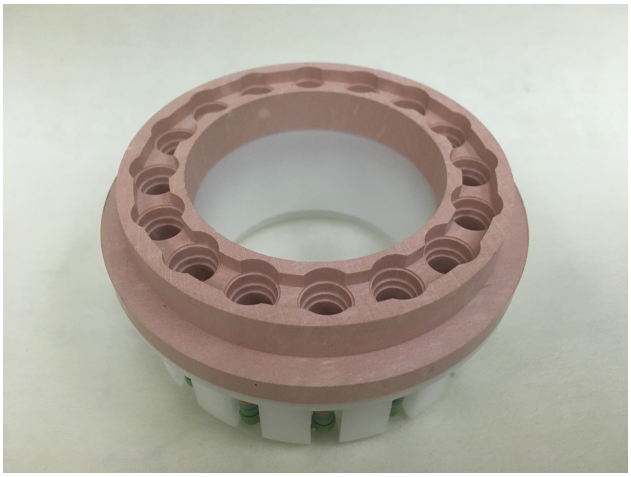

Figure B.7: A failed pre-ionization system for the BRB CTI. The sharp corners of the alumina-silicate ceramic insulator (pink) led to focused electric fields causing coronal discharge and a failure of the isolation. While this system could have insured a symmetric ionization, it was replaced in favor of the simpler glow discharge between the center and outer conductors.

the PI systems used at TAE and PLX had substantially more power: 2.4 MW for 20 μs and 4.0 GW for 5 μs, respectively.

While these pre-ionization systems did ensure a reliable plasma breakdown, the complications from a second high voltage pulsed power system are substantial. Inspired by simplifications from the PLX and Hyper-V plasma guns, the PI method presented in Fig. B.3 was adopted. Here, a large impedance resistor R_{PI} was connected directly from the main capacitor HV terminal to the inner conductor. In this configuration, the inner conductor is at potential as soon as the HV PS begins charging. As gas from the puff valve reaches the breech, plasma is formed within the barrel by coronal or glow discharge.

Different values of R_{PI} of 10, 1, and 0.6 kΩ were tested. The 0.6 kΩ resistor gives a nominal PI power of 170 kW, with a decay period of 42 ms (for $C_0 = 70$ μF). Of course, much of this power is being dissipated in the resistor rather than in the plasma itself. Decreasing the resistor value to 150 Ω would increase the PI power to 670 kW, while $\tau_{rc} = 10$ ms. If performance of the CT needs to be improved, I recommend installing a higher power resistor.

Attempts to make a similar higher power pre-ionization system on the BRB were extensive. A 16 pin sparker was designed to improve the symmetry of the pre-I plasma and ideally improve the repeatibility, shown in Fig. reffig:preIfail. Ultimately, the sharp corners on the ceramic insert, and the sharp edges of the molybdenum screw tips, prevented this design from sufficiently standing off enough voltage for safe operation. An insert with curved ceramic edges could be designed. Before doing so, one should take images of the preI coronal breakdown to determine if this is in fact necessary. If the coronal discharge appears symmetric and reliable, designing this sparker may be less effective than just increasing the power.

Never trust a puff

Perhaps most important for gun reliability is the operation of the puff valves. After much consternation examining the electrical systems, we thought to test the performance of the valves themselves. Rigorous testing by measuring the base pressure jump of the 10 m^3 BRB vessel revealed that the valves have quite a varied performance.

In fact, several identical valves in the normal plasma washer gun array were quite close to failure. When we thought our experiments were being saturated with neutrals, they were actually operated in a gas-starved regime.

After this realization, four puff valves were ultimately used on the CT to ensure consistent breakdown. A future upgrade to the gas puffing system improving reliability would be a significant improvement.

B.5 Magnetic Flux Injection

As detailed in the first section, the magnetized coaxial plasma gun is a subset of the larger class of coaxial plasma guns. Injecting bias flux into the gun barrel was originally done with a pulsed circuit. Following developments done at TAE, this pulsed system was eventually replaced with a DC solenoid with a soft iron core. The high magnetic moment of the iron ($\mu_r \geqslant 20,000$) amplifies the magnetic field and, when offset with the solenoid, produces an optimal radial geometry. The current BRB set-up copies exactly the configuration presented by Edo [37] and uses a DC power supply to drive a steady current of 0-3 A through a solenoid (500 turns, 2 layers, 12" long) around a soft iron core.

For the BRB CTI, we measured the normal magnetic field component at the surface of the iron core and integrated that to estimate the total magnetic flux. With this, we can compare our values with the theoretical flux at which the plasmoid will not detach from the barrel. As described by Barnes [2] and derived from considerations of force balance, the gun parameter λ compares the ratio of current to poloidal bias flux in the given geometry:

$$\lambda = \frac{\lambda_g}{\lambda_c} \equiv \frac{\frac{\mu_0 I_g}{\Psi_b}}{\frac{\pi}{d}} \geqslant 1 \tag{B.1}$$

Here, Ψ is the total poloidal flux, I the total current through the plasma, and d the radial gap distance. If $\lambda > 1$, the accelerating $J \times B$ force will exceed the poloidal field line tension and the plasmoid will escape by reconnecting. Using our maximum value of $\Psi = 0.43$ mWeber, $I = 100$ kA, and $d = (83.1 - 54.0)/2$ mm, our λ parameter is 1.4.

Clearly, when the bias flux is driven at 3 A, our CT is close to failing to detach. This

I_b [A]	Ψ_b mWebers
1.5 A	0.15
2.0 A	0.30
2.5 A	0.38
3.0 A	0.43

Table B.3: Magnetic flux vs solenoid current in the BRB CTI. This is for a solenoid whose end is offset 4 inches from the iron core tip, which is fully inserted into the center conductor, as shown in Fig. B.1. Hysteresis is an issue that is not represented in this table. These measurements should be repeated, particularly when an external HH field is applied.

represents a substantial improvement over the previous bias system. The original system was pulsed and injected approximately 35 μWebers of flux (220 A peak current on a 60 turn solenoid with ID 22 mm), giving a minimum $\lambda = 17$.

There are substantial complications when operating the CT injector while also using the Helmholtz or mirror coils. Both of those coils lead to axial fields at the locations of the CTI, 0.7 m away from the poles of the machine. These smaller fields change the magnetization of the iron core, leading to more or less flux depending on the orientation.

It is recommended that a high-permeability shield be placed around the CT barrel to shield the core from the fields of the HH/mirror coils. Back of the envelop calculations suggest that is is feasible to exclude the few milliTesla of field from the HH coils. However, in situ testing suggests otherwise.

We wrapped 5 layers of 4 mil thick mu-metal into a cylinder of length 20 cm. This was secured adjacent to the CTI barrel. A Hall probe was placed inside to measured the magnetic field and the field was ramped up. At an applied field of 4 mT, the measured field inside was well above 3 mT. This is woefully insufficient.

It is possible that a much thicker piece of mu-metal or soft iron might function better. Given the importance to many experiments of knowing precisely the initial magnetic flux, this is worth investigating.

C SHOCK EXPERIMENT PROBE DESIGN

C.1 Summary

This section details the development of the quadruple tip probes used for the parallel shock experiments. These efforts were successful in making plasma density measurements that were immune to pulsed power noise and potential fluctuations. They were only partly successful at making accurate electron temperature measurements. Suggestions for further development are given.

C.2 Probe Requirements in Pulsed Power Environments

The first experiments on the Big Red Ball (BRB) in the Madison Plasma Dynamo Experiment were quasi steady state experiments. To make measurements of the plasma density and temperature, single tip Langmuir probes sufficed for most experimental measurements. They generally had a voltage range from -150 to +40 V that was swept in a sawtooth waveform at 400-1000 Hz. This swept waveform limits the usefulness of the probes to phenomena slower than the sweep frequency. See D. Weisberg's thesis for examples [115].

In the last several years, fast dynamics in the Terrestrial Reconnection EXperiment (TREX) necessitated the use of a 16-tip Probe to measure the >1 MHz fluctuations. For this probe, 16 individual ground referenced probes sample the plasma IV curve at fixed voltages. See J. Olson's thesis for a complete description [84]. However, for the shock experiments in this regime, intense electric fields of over 2 kV/m have been observed in Argon plasmas. The large potential jumps from these electric fields can exceed the range of the ground-referenced fast Langmuir probe and seem to exacerbate arcing of the probe tips. Figure C.1 shows a dip in I_{sat} caused by a drop in the plasm potential, and not a density fluctuation.

These two limitations in speed and range initiated the development of probes for BRB specific pulsed power plasmas. More recent experiments involving the collision of two CTs have only underscored the need for reliable measurements in these types of plasmas [17].

The problem of making probe measurements in pulsed power plasmas is not a new one. Plasmas in coaxial plasma guns, dense plasma focii, laser ablation plasmas and other pulsed power experiments all struggle with the same challenge. Triple probes are often used in this situation for their fast response and resistance to large potential fluctuations (see e.g. [24, 78]).

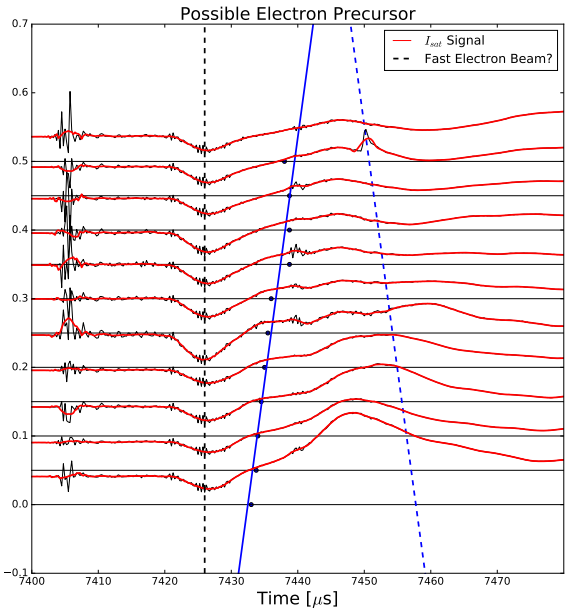

Figure C.1: An example of the limitation of ground referenced Langmuir probes. These 11 I_{sat} traces are from a multi-tip probe where each tip is independently biased to -150 V. They are offset in the z-direction by their vertical location, with shared units in amps. The blue line tracks the rise in density likely similar to that in Chapter 3, with the peak density of the CT coming later. The black dashed line shows a simultaneous dip across all channels, reflecting a sudden drop in the bulk plasma potential. The blue line intersects the black very close to Z=-1.5 m, and thus this plasma potential fluctuation is likely related to the entrance of the CT into the vessel.

As an example, the Compact Toroid Injector (CTI) loaned to the BRB from TAE Technologies uses a standard triple probe to make measurements in the very dense and hot ($n_e \sim 10^{20-21}$ m^{-3}, $T_e \sim 20$ eV) plasmas in the CTI barrel. The straightforward design uses a high impedance voltage divider (>100 kΩ) to measure the voltages of the floating and the positive bias tips, while a galvanically isolated Pearson model 4100 current transformer measures the current flowing between the two biased tips. This probe is mostly used for making measurements of the arrival time and peak density of the injected CT, a purpose it serves well.

Attempts to adapt similar triple probes for use in the BRB were met with several problems. First, the much lower densities ($2 \cdot 10^{17-19}$ m^{-3}) of the BRB background plasmas made the current signals quite small. The Pearson transformer has a 1.0 V/A calibration, and to increase the gain means either using multiple windings through the transformer core or increasing the probe tip collecting area. Second, the Pearson transformers rely on inductive electric fields and have a 3 dB corner frequency at 140 Hz. Typical pulsed experiments use a 10 ms washer gun produced background plasma. The high-pass filtering of the current transformers introduces significant droop in the signal even before the target plasma has reached steady state.

A third problem is that the large currents from the probe tips produce magnetic fields that inferred with the adjacent B-dot coil measurements. If an arc occurs, the magnetic signals are often also ruined because of the magnetic fields produced in the event. Finally,

noise from the pulsed power circuitry often makes analysis quite challenging.

With this experience as a guide, the requirements for an ideal probe for BRB pulsed power experiments can be outlined.

- Immune to large plasma potential fluctuations
- Frequency response good to 10 MHz
- Accurate density, potential, and temperature measurements
- Accurate magnetic field measurements
- Resistant to significant common mode noise

Triple probes are used in pulsed power experiments because they meet the first three of these requirements easily: they generally have a large impedance to ground, they have a maximum frequency response of near ω_{pi}, and in Maxwellian plasmas have a good theoretical underpinning. The last two requirements can be addressed with experimental techniques like proper shielding of cables, termination of transmission lines, good tip design, and exploiting common mode rejection via paired channel subtraction. This appendix documents the latest attempt to simultaneously meet these requirements.

C.3 Lessons Learned from Prior Probes

The original combination Mach/Langmuir probes used for the Madison Plasma Dynamo experiments used Tungsten and Tantalum probe tips. Making the electrical connections to these refractory metals was arduous: the copper transmission line was wrapped in nickle ribbon and then spot welded against the tantalum tip. This was finicky, time consuming, and the connection often failed during probe assembly. In contrast with spot welding, press fit connections with mechanical contact ensuring electrical contact are generally easy to assemble and reliable when in the plasma.

An early hanging array of triple probes used press fit connections (one tip shown in Fig. C.2) and was designed to give full coverage of the first CT experiments. A typical shot of a CT fired into plasma measured by the hanging triple probe array is shown in figure C.3. The probes used large tip sizes to increase the probe current and signal, and to compensate for the lower densities as the CT expands. Tip arcing, visible in three of the black traces, was a problem only because the tips never had a chance to be properly cleaned: the experiment was terminated early because of catastrophic failure in the CTI pulsed power circuitry. Nonetheless, they demonstrated the feasibility of triple probes for fast density measurements in the BRB bulk plasma.

Figure C.2: One triple probe segment of four in a hanging array, centered at R = 10, 30, 50, and 70 cm. The plasma-facing molybdenum probe tips are jammed onto the stainless steel cylinder springs, which are soldered then to the copper wire. This type of press fit connection obviated the need for spot welding. Such a probe was never put to good use because of a failure in the CT switch stack that ended the experiment early.

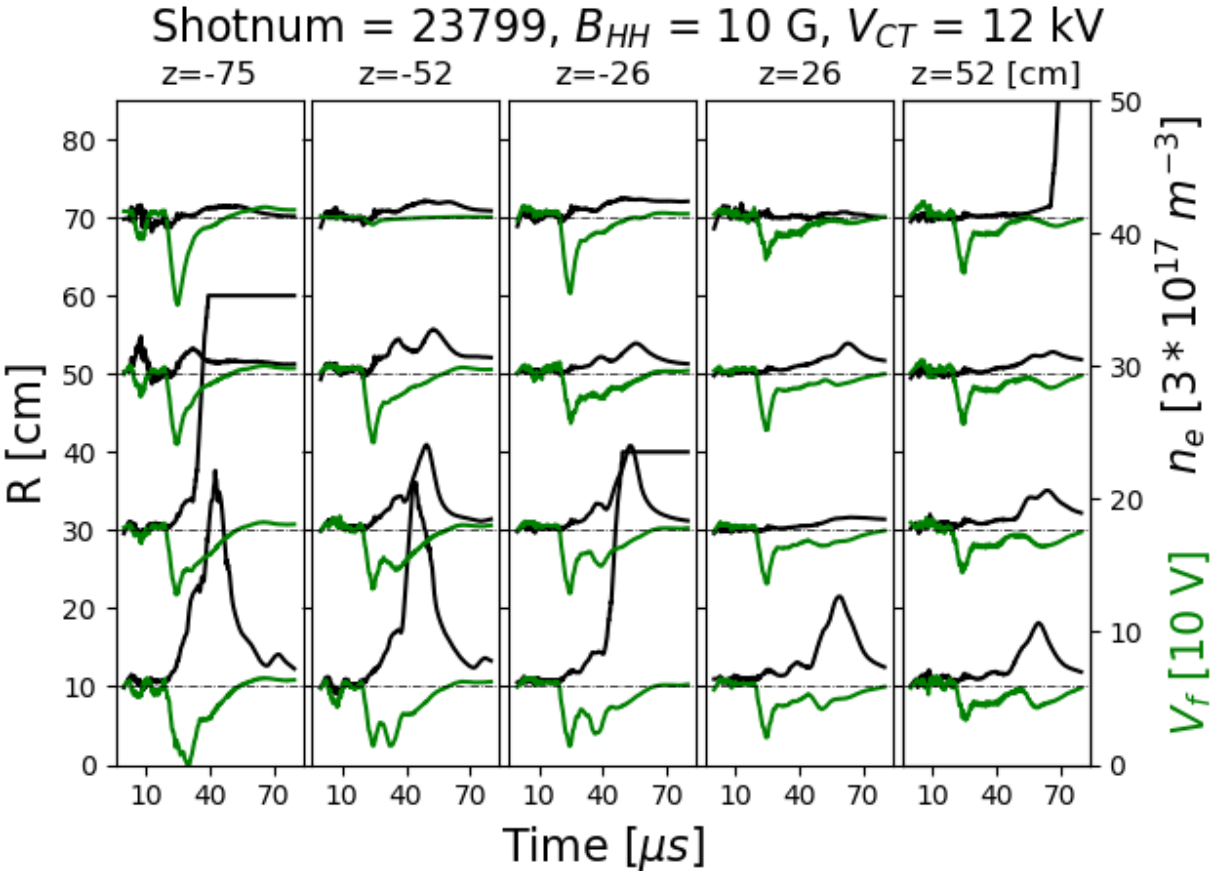

Figure C.3: Results from the 5 hanging triple probe arrays, showing density and floating potential measurements. Three probes at (R,Z) = (-75,30), (-26,10), and (52,70) showed arcing. Otherwise, this demonstrated the feasibility of using triple probes on a large scale. Electron temperature measurements from these probes did not agree with the Langmuir probe measurements, and sometimes went negative.

It was clear from the first shock experiments that a measurement of both the magnetic field and the plasma parameters at the same location was necessary. This is sometimes tricky when, for the large densities and fast flows of these shock experiments, the dI/dt to a probe tip can be substantial and will induce real signals in the B-dot probes that are near impossible to remove post-hoc.

One particularly audacious probe design involved the construction of a spiral tipped probe. This probe head had four separate tips forming two double wire pairs, with each wire wound one full helical turn around the 1" long shaft. A 3-axis $\dot{B}$ probe centered inside of the helix completed the design. In theory, since the currents flowing in and out of each probe pair were identical and symmetric around the magnetic coils, no amount of current could lead to spurious pick-up signals.

In practice, this was a foolhardy venture. This probe tip was complicated to build and relied on perfect symmetry between the tips to work. Ultimately, the probe tip was prone to arcing and was mostly useless. It served as an excellent example of the merits of the K.I.S.S. principle of design.

C.4 Parallel Shock Experiments Quad-tipped Probe Design

The following section outlines how the Quad-tipped probes were designed to meet the shock expeirment requirements.

First, meeting the high speeds required is always a challenge for the BRB because of its large size and transmission line effects. To reach the center of the machine requires a probe generally much longer than 1.5 m (2.5 m in this case), and then several meters of cabling to reach the digitizers. For cables that transmit at $^2/_3$ c, the quarter wavelength frequency for 5 m of cables is just under 10 MHz. Improper termination will lead to large noise in our measurements from reflections.

However, proper 50 Ω termination introduces another problem to the voltage division: a probe with high impedance to ground will divide down the measurement beyond the digitizers range and resolution. For example, probe-plasma impedances for these probes are generally less the 1 kΩ for the positively biased tip. A 10:1 voltage divider for 50 Ω termination is only a 500 Ω impedance, and so a substantial fraction of the total current being collected by the positive tip is passing through the divider. This may radically change the dynamics from the ideal double probe presented in Fig. C.8. A resistor of 4.71 kΩ was chosen as a compromise between high impedance and optimizing the digitizer range and resolution.

To protect the digitizers from this relatively low impedance path to ground (and catas-

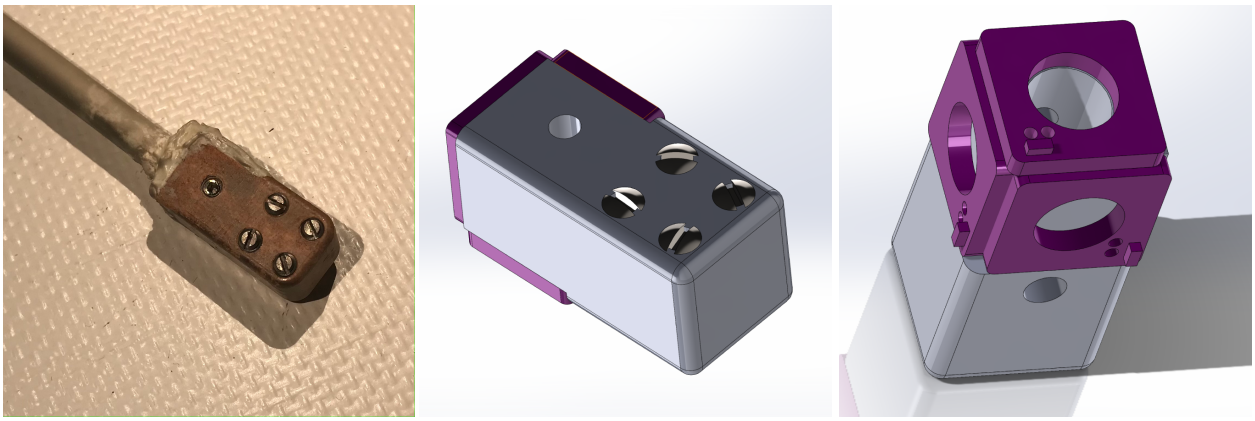

Figure C.4: This design is the latest probe iteration in the pursuit of a simple and reliable probe for shock experiments. At left, a probe tip after use in the experiment. The four slotted flat screw tips serve as planar langmuir probe tips. A 5′ long, 1/4" diameter alumina ceramic shaft supports the 1" long, 1/2″ wide LAVA body. In the renderings at right, the purple represents the magnetic pick-up coils: two turn square loops of 2 cm^2 total area with surface mount termination resistors. The coils are Oshpark printed thin PCB boards and are covered in torrseal epoxy to protect from the plasma.

trophic failure in the event of an arc), a 10 μF, HV blocking capacitor was placed at the top of the divider. This introduces its own set of challenges that will be dealt with in section C.6.

The probe tip is a simple to assemble and robust design, shown in Fig. C.4. The flat faces of four, #6-32 molybdenum slotted set screws serve as the plasma collecting surfaces, with areas of 9.7 mm^2. The probe faces are flush with the surface of the alumina silicate (LAVA) tip. These set screws make press fit connections with two pairs of 24 a.w.g. twisted pair, kapton-coated cables. Separated from the probe tips by 1 cm are three orthogonally-mounted, 2-turn magnetic pick-up coils. These are very precisely manufactured thin pcbs which are coated in torr-seal epoxy to protect from the plasma.

The three pairs of twisted pair, 28 a.w.g. wires from the magnetic probes are protected from the capacitive noise of the double probes by a grounded conducting jacket. These 10 wires pass through a 5′ long ceramic alumina, 1/4" diameter shaft into a 3′ long, 1/2" diameter stainless steel shaft with attached can, left Fig. C.5. They pass through an in-house produced D-sub 15 vacuum feedthrough, into the electronics box mounted directly onto the exterior of the can.

The electronics in the can are designed from several iterations of double probe circuitry. They are arranged to fit tightly in the can to shield from stray noise. One of the two PCB boards is shown in Fig. C.6.

The probes are mounted on top of the BRB on the boxports parallel to the machine axis.

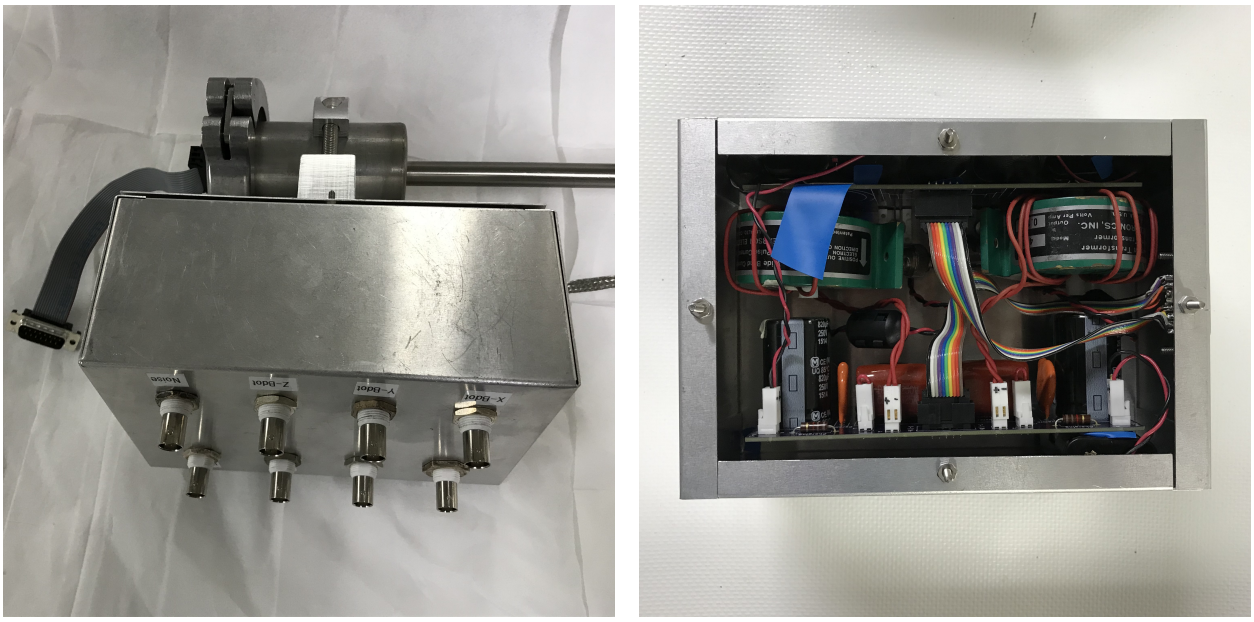

Figure C.5: The probe can mounted electronics box was designed to be as compact as possible so that it could be mounted as close to the probe as possible and reduce the already significant inductive transmission line effects from the 2.5 m long probe. The gray D-sub 15 cable connecting the probe feedthrough to the box is the only location where the signal carrying wires are unshielded. A better design might have solved this.

They have 2' lengths of vacuum garage so that the SS shaft need not be inserted past the magnetic cusp so as to not perturb the plasma potential. Coaxial cables run from the probe electronics boxes to a digitizer mounted on the vertical boxport above the North pole of the machine.

There are other ways to isolate probes. Very isolated probes with impedance to ground above the 10 or 100 MΩ range can be built with wireless transmitters, optical voltage to frequency converters, or Iso-amplifiers. These examples are more demanding than is typically necessary. Often, a cheap and simple voltage divider of sufficient impedance will properly isolate the probe.

C.5 Quadruple Probe Theoretical Background

In this section, we will derive the relationship between the desired parameters of plasma density (n_i), electron temperature (T_e), and plasma potential (ϕ_p, also called the Space Charge Potential) and the measured quantities of voltage and current. This is done specifically for a Quadruple probe: two double probes of differing voltages. The intention behind this design was to avoid one of the common experimental problems of triple probes, namely noise fluctuations causing the floating potential measurement to exceed the voltage of

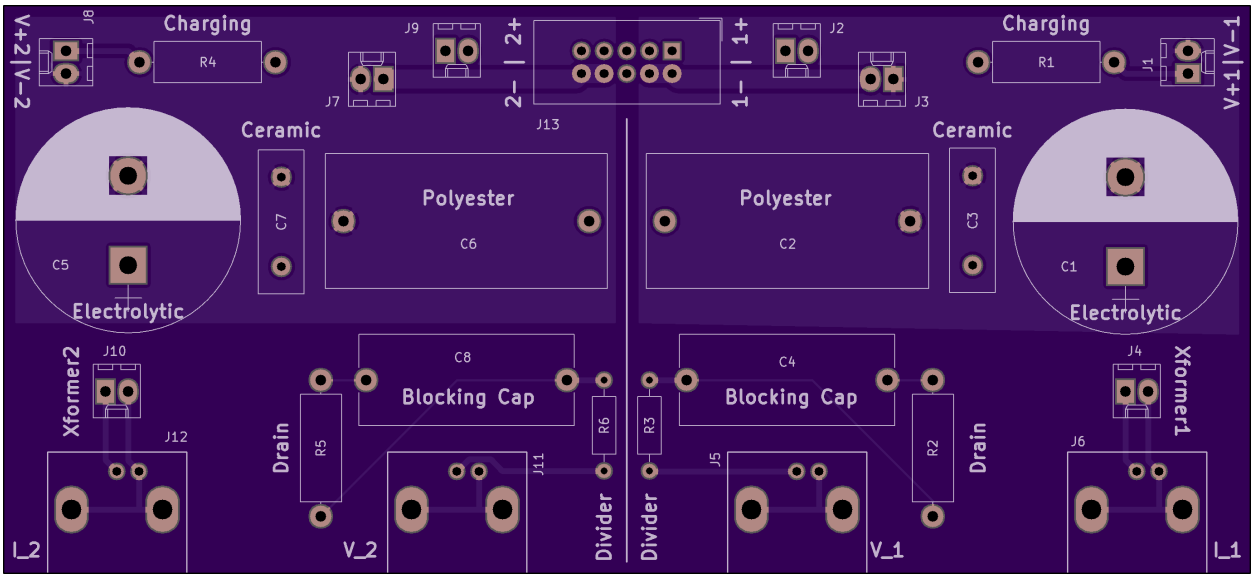

Figure C.6: One of the two circuit boards for each probe. Three capacitors (an electrolytic, polyester, and ceramic for good frequency response) form a total capacitance of around 850 µF. The junctions J2 and J9 pass through the probe current through the transformer core 10 times (red wires around Pearson in Fig. C.5), and the parallel junctions J3 and J7 are jumpered. These were swapped to test whether the capacitive pickup on the Pearson could be reduced by the location of the measurement, and it was found to be slightly better on the V+ side. Two different voltages, nominally +3 V and +54 V, powered the left and right sides, and made this into a unique quadrupole probe.

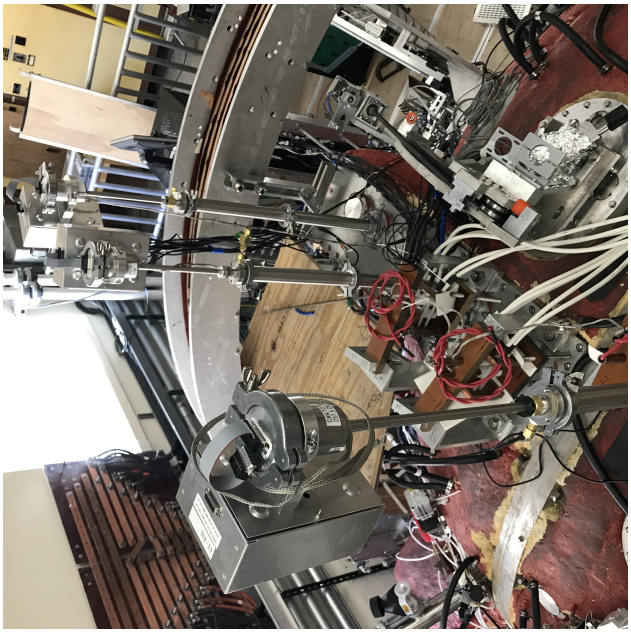

Figure C.7: Image of the hanging probes mounted on the top boxports of the BRB. Only three of the four probes are visible. Note how the probes are offset from the midplane of the machine. This prevents the probes from reaching below R = 14 cm. In the future, angled flanges enabling access to the machine axis are recommended. These probes have two 1′ lengths of housing outside of the machine, allowing for that much possible radial translation while ensuring that only the 5′ long insulating ceramic shaft is exposed to the plasma, and not a metal shaft that could possibly short the plasma dynamics.

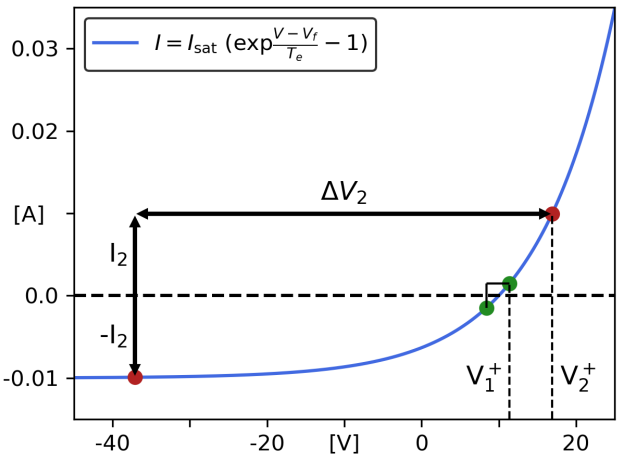

Figure C.8: Traditional triple probes measure both the floating potential and the positive tip potential, and from the difference calculate the electron temperature. Triple probes on the BRB have often shown a tendency for the measurement of the positive tip voltage to dip below the measured floating potential. This is obviously unphysical and is perhaps due to some capacitive or transmission line effect. It was hoped that by using symmetric circuits in the quadruple probe configuration, shown in the diagram at left, this could be prevented.

the positive tip. It was thought that by designing nearly identical circuits they would both behave similarly and also that common mode noise would be subtracted away in the differential measurement. This was mostly successful, but work remains to verify the trustworthiness of the electron temperature and plasma potential measurements.

Most first semester students of plasma physics know that an object placed in an ambient plasma doesn't charge up to the plasma potential, but instead charges to the floating potential (ϕ_f), the potential where the electron and ion currents are identical. This is because the electrons, generally faster by the square root of the ion-electron mass ratio, self consistently set up a sheath around the object to preserve the overall quasineutrality of the plasma. The current collected by the probe tip is commonly expressed with electron current as positive and ion current as negative:

$$I_{probe} = I_e - I_i \tag{C.1}$$

In an unmagnetized plasma, the electron current to a probe can be expressed using a Boltzmann distribution that reflects the potential barrier of the sheath [93]:

$$I_e = AJ_{e0} \exp\left(-\frac{e\phi_p^i}{T_e}\right) = Aen_e\sqrt{\frac{T_e}{2\pi m_e}} \exp\left(-\frac{e\phi_p^i}{T_e}\right) \tag{C.2}$$

where A is the collecting area of the probe tip, J_{e0} represents the random thermal electron current, e the fundamental charge of an electron, m_e the electron mass, and ϕ_p^i the potential difference of the i^{th} probe tip with respect to the plasma potential, $\phi_p^i = \phi_p - \phi_i$. The theoretical ion current is premised on the Bohm criterium: since the sheath is designed to repel electrons, any ion that enters the sheath will be trapped in the potential and collected at the probe tip. Thus, the ion current is determined by the ion flux into the sheath edge,

which depends on the ion thermal/sound speed in the ambient plasma:

$$I_{sat} = Aen_i\sqrt{\frac{T_e}{m_i}}\exp\left(-1/2\right) \tag{C.3}$$

Where the RHS shows the result of the thin sheath approximation, valid if the debye length is much less than the probe size, $d_e \ll l$ [65]. The factor $\sqrt{\frac{T_e}{m_i}}$ is a cold ion assumption, that the flux of ions to the sheath is dominated by the flux from pressure waves and not thermal ions. Combining these expressions gives us a useful model for the current to the probe tip:

$$I = Aen_i\sqrt{\frac{T_e}{m_i}}\exp\left(-\frac{1}{2}\right)\left[\sqrt{\frac{m_i}{m_e}}\frac{\exp\left(\frac{1}{2}\right)}{\sqrt{2\pi}}\exp\left(\frac{-e\phi_p^i}{T_e}\right)-1\right] \tag{C.4}$$

This model fails before it reaches the plasma potential, and also does not include the effects of ion sheath expansion. Setting the current to the probe tip to zero, we find the relationship between the floating potential and the plasma potential.

$$\phi_p^f = \phi_p - \phi_f = \frac{1}{2}\left(\ln\left(\frac{2\pi m_e}{m_i}\right)-1\right)\frac{T_e}{e} \tag{C.5}$$

$$\phi_f = \phi_p - 3.3\frac{T_e}{e} \tag{C.6}$$

Which reproduces for Hydrogen a common experimentalist rule of thumb that the plasma potential is 3.3 times the electron temperature (expressed in [eV/e]) above the floating potential.

Figure C.9 shows a simplified schematic of the double double probe circuitry. One circuit will have a bias voltage V_1 which is somewhat less than the nominal T_e, and the second circuit a bias V_2 larger than $3T_e/e$ [V]. Available batteries make 3 V and 54 V convenient numbers.

Using equation C.4, we can write the expected current into the positive and negative probe tips:

$$I_1^+ = Aen_i\sqrt{\frac{T_e}{m_i}}\exp\left(-\frac{1}{2}\right)\left[\sqrt{\frac{m_i}{m_e}}\frac{\exp\left(\frac{1}{2}\right)}{\sqrt{2\pi}}\exp\left(\frac{-e\phi_{p1}}{T_e}\right)-1\right] \tag{C.7}$$

$$I_1^- = Aen_i\sqrt{\frac{T_e}{m_i}}\exp\left(-\frac{1}{2}\right)\left[\sqrt{\frac{m_i}{m_e}}\frac{\exp\left(\frac{1}{2}\right)}{\sqrt{2\pi}}\exp\left(\frac{-e(\phi_{p1}+V_1)}{T_e}\right)-1\right] \tag{C.8}$$

The current into the second pair of tips is identical with a change of subscript. Together that gives four equations, with the four unknowns ϕ_{p1}, ϕ_{p2}, T_e, n_i. We can solve this system of

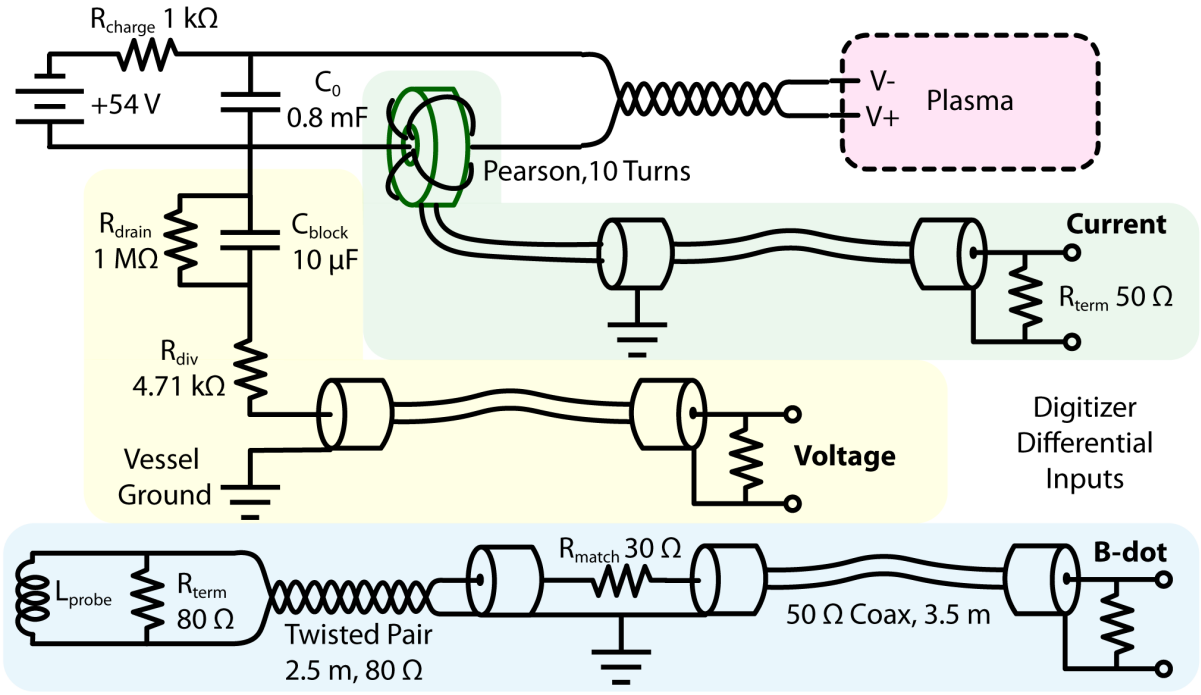

Figure C.9: A simplified circuit diagram of the quad tipped probe electronics, with the actual board shown in Fig. C.9. The probe tips in the plasma are connected via 2.5 m lengths of 24 a.w.g. kapton-insulated twisted pair cable from Accuglass. The electronics are housed in an aluminum box on the probe can shown in Fig. C.5, and are connected to the differential digitizer inputs by 4 m lengths of coax cable. For each probe there are three orthogonal B-dot circuits in blue, and two each of the voltage and current measurement circuits in yellow and green, for each pair of probe tips.

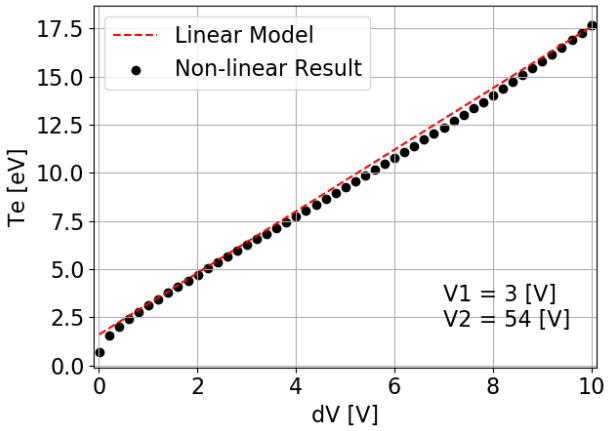

Figure C.10: A numerical solution to Eq. C.9, showing the mostly linear relationship between the plasma electron temperature and the measured voltage difference between the two probe tips. Most actual measurements of dV will be between 1 and 5 volts. This is a challenging measurement, as noise is substantial and fluctuations are much larger than 5 V. The attempt to reduce common mode noise via channel subtraction was only marginally successful.

equations for T_e, n_e, and ϕ_p in terms of $I_1 - I_2$ and $\phi_1 - \phi_2$, two measurements that take advantage of the common mode noise subtraction technique.

$$\phi_2 - \phi_1 = \frac{T_e}{e} \ln \frac{\left(1 + \exp\left(-\frac{eV_1}{T_e}\right)\right)}{\left(1 + \exp\left(-\frac{eV_2}{T_e}\right)\right)} \tag{C.9}$$

$$\phi_p = \frac{T_e}{e}\left[\ln \frac{\exp\left(\frac{e\phi_1}{T_e}\right)\left(1 + \exp\left(\frac{-eV_1}{T_e}\right)\right) + \exp\left(\frac{e\phi_2}{T_e}\right)\left(1 + \exp\left(\frac{-eV_2}{T_e}\right)\right)}{4\frac{\sqrt{2\pi}}{\exp\left(1/2\right)}\sqrt{\frac{m_e}{m_i}}}\right] \tag{C.10}$$

$$n_e = \frac{(I_2 - I_1)}{Ae}\sqrt{\frac{2\pi m_e}{T_e}}\left[\exp\left(-\frac{e\phi_p}{T_e}\right)\left(\exp\left(\frac{e\phi_2}{T_e}\right) - \exp\left(\frac{e\phi_1}{T_e}\right)\right)\right]^{-1} \tag{C.11}$$

Solving equation C.9 for the electron temperature can be done numerically in light of its non-linear nature. For fixed values of V_1 and V_2, the numerical solution is plotted in figure C.10 as a function of the voltage difference between the two probe tips $\phi_2 - \phi_1$. With a value for T_e, equation C.10 can now be solved, and then so can equation C.11. Error estimation and propagation through this system is messy and will be discussed in a later section.

C.6 Experimental Measurement Analysis

Measuring the voltage from the circuit drawn in Fig. C.9 is not as straightforward as multiplying by the voltage divider value. The actual voltage at the positive probe tip V^+ is measured voltage from the digitizer voltage $V_{digi.}$ multiplied by the voltage divider, plus the voltage across the blocking capacitor V_{cap}, plus the voltage drop from the Pearson transformer insertion resistance V_{Xfmr}, plus the voltage drop from the transmission line impedance V_{trans}:

$$V^+ = V_{div.} + V_{cap} + V_{Xfmr} + V_{trans} \tag{C.12}$$

Examining this term by term, we begin with the voltage divider. We multiply the digitizer voltage by the resistor values:

$$V_{div.} = \frac{4710\ \Omega + 50\ \Omega}{50\ \Omega} V_{digi.} \tag{C.13}$$

Fig. C.9 shows a drain resistor of 1 MΩ parallel to the 10 μF blocking capacitor. The RC time constant for this is simply 10 s, and it guarantees that at the start of each shot there is no residual voltage on the blocking capacitor. In that case, the voltage on the capacitor can

be integrated from the total measured current through the voltage divider:

$$V_{cap} = \frac{Q}{C} = \frac{1}{10\ \mu F}\int_0^t \frac{V_{digi.}}{50\ \Omega}dt \tag{C.14}$$

The insertion resistance from the Pearson transformer is an interesting effect. This is a small resistance $(0.02\ \Omega/\text{turn}^2)$ that appears on the primary winding. Since the two circuits V_1 and V_2 have 11 and 5 windings, respectively, we can write for the V_1 circuit:

$$V_{Xfmr} = I \cdot 0.02\ \Omega \cdot N^2 = \big(2.4\ \Omega\big)I \tag{C.15}$$

and we will find I from our analysis of the current later. Finally, finding the voltage drop across the transmission line is tricky. While capacitive effects can be substantial, it appears the largest contribution is from inductive effects as the probe tip current changes. For the 2.4 m length of 24 a.w.g. twisted pair cables, that's an approximate inductance of 1.1 µF.

$$V_{ind.} = L\frac{dI}{dt} = \big(1.1\ \mu F\big)\frac{dI}{dt} \tag{C.16}$$

Before the probe tip voltage can be calculated, a similar procedure needs to be performed on the measured current. From Fig. C.9, it is clear that the total current that passes through the Pearson $I_{Pearson}$ has a component that goes into charging the blocking capacitor and the voltage divider. That can be directly subtracted.

$$I_{tip} = I_{meas} - I_{div.} = \frac{11}{2}V_{Pearson} - \frac{V_{digi.}}{50\ \Omega} \tag{C.17}$$

Where, again, the factor 11/2 is for the 11 turn gain and the $^1/_2$ factor from the 50 Ω termination, per the Pearson specifications.

However, the frequency response of the Pearson transformers complicates this procedure further. The transformers provide galvanic isolation with a very linear response over a wide frequency band (3 dB points at 140 Hz to 15 MHz). Unfortunately, they cannot pass DC signals, and the low frequency 3 dB cutoff leads to a droop in the signal. From the Pearson Model 4100 data sheet, this droop is expressed as a rate of $D = 0.09\ \%/\mu s$ but it can also be related to the low end corner frequency as $D = 2\pi f$.

Compensating for this droop is fairly straightforward. Similar work was done for this lab group by M. Brookhart [12].

$$I_{actual} = I_{meas.} + \frac{1}{\tau}\int_0^t I_{meas.}dt' \tag{C.18}$$

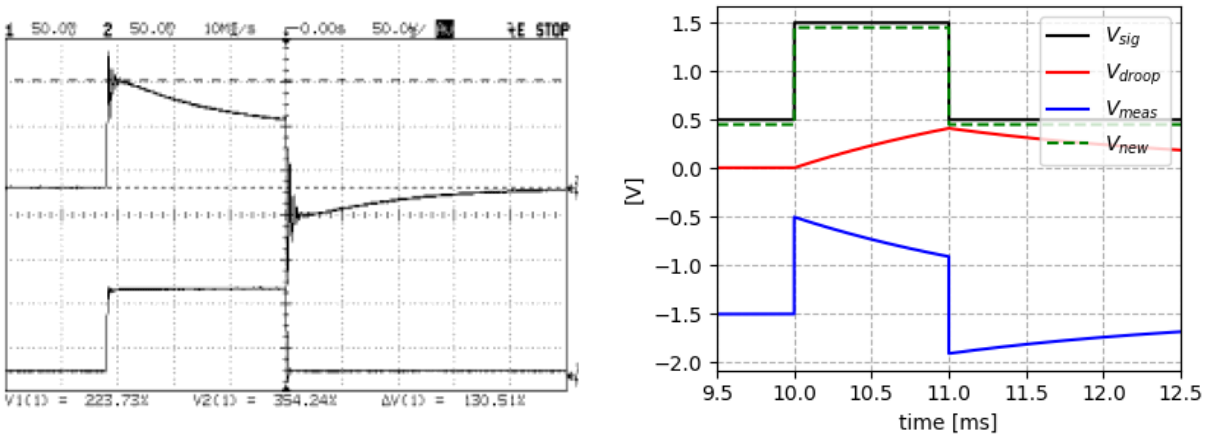

Figure C.11: At left, two traces that show the Pearson response (top) to a square current pulse (bottom). While good at high frequencies, the Pearson has a droop that needs to be corrected for. At right, simulated data showing the original signal in black, the simulation measured signal in blue, the cumulative droop in red, and the corrected signal which reproduces the original, dashed green line.

which can be easily implemented with a numberical cumulative summation routine. The time constant τ is close to $1/D$, but is experimentally determined: it is the value for which the current returns to zero after a standard 10 ms plasma gun.

It was found in the data analysis that this was not enough to properly model the currents to the probe. It was necessary to also include capacitive currents, perhaps flowing into the Pearson transformer itself:

$$I_{capac.} = \frac{d}{dt}(CV) = C\frac{dV}{dt} \tag{C.19}$$

The capacitance C was also experimentally determined by examining instances of rapid plasma potential fluctuation in the absence of density fluctuations.

This is now enough information to calculate the current flowing to the probe tips and the voltages of those tips. The result for a typical parallel shock experiment is shown in Fig. C.12. The quad probe density measurement shows excellent immunity to the plasma potential fluctuation as the CT enters the vessel. The electron temperature measurement appears to be a bit high for the background plasma.

C.7 Error Analysis

The non-linear nature of equation C.9 makes a traditional error analysis difficult. Ignoring the errors in the bias voltages V_1 and V_2, to estimate the error in T_e from the measurement error in $\phi_2 - \phi_1$, one would normally calculate the partial derivative $\frac{\partial T_e}{\partial \phi}$. Since ϕ_1 and ϕ_2 are direct measurements with identical uncertainties, we can combine them into a error

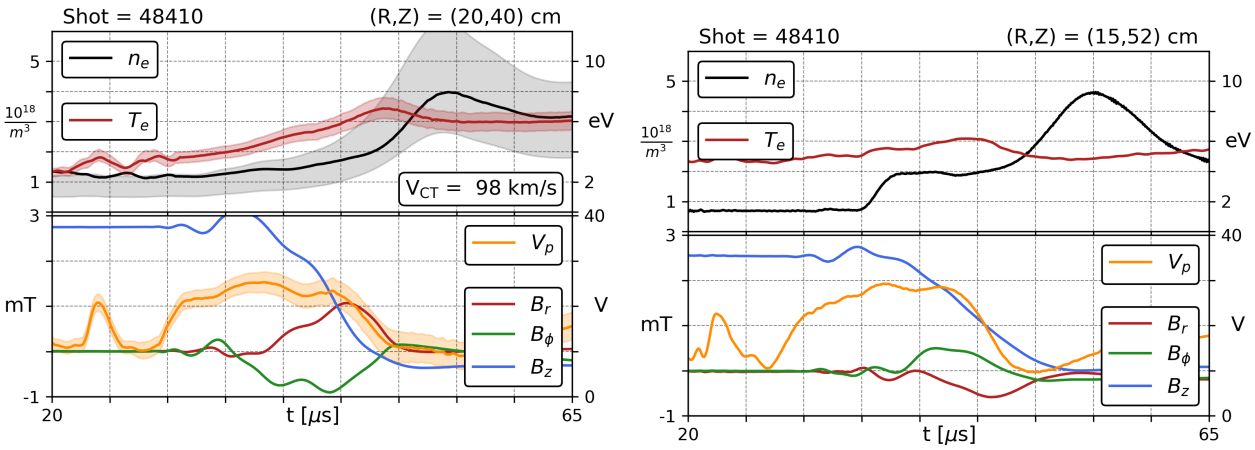

Figure C.12: A comparison of the responses between the T_e probe (left) and the quad-tipped probe (right). The probes are separated by the radial and axial distances shown, but also by about 30° in the toroidal direction, and so none of the signals should be identical. Note how for the large plasma potential fluctuations at 23-24 µs the quad probe shows almost no response in the density measurement, which we believe is correct. This resistance to potential fluctuations is the sole advantage over the T_e probe, which has a much more accurate measurement of the electron temperature.

$\sigma_{\Delta\phi}$ for the variable $\Delta\phi = \phi_2 - \phi_1$ as

$$\sigma_{\Delta\phi} = \sqrt{\sigma_{\phi 1}^2 + \sigma_{\phi 2}^2} \tag{C.20}$$

While a direct analytical solution isn't possible, figure C.10 shows that a linear fit is a reasonable approximation over the entire usable probe range. With a linear approximation, the partial derivative becomes trivial, and error propagation becomes simple.

$$\sigma_{T_e} \simeq 1.6\ \sigma_{\Delta\phi}$$
$$\sigma_{V_p} \simeq 6\ \sigma_{\Delta\phi}$$

Since n_e depends on $\nabla\phi$ and also ∇I, after some straightforward algebraic aerobics:

$$\sigma_{n_e} = \sqrt{\left(\frac{\partial n_e}{\partial \Delta\phi}\right)^2 \sigma_{\Delta\phi}^2 + \left(\frac{\partial n_e}{\partial \Delta I}\right)^2 \sigma_{\Delta I}^2 + \frac{\partial^2 n_e}{\partial \Delta\phi \partial I} \sigma_{\Delta\phi}\sigma_{\Delta I}} \tag{C.21}$$

we get Eq.C.21 which is a useful expression for the error in the density. A probabilistic model was used to test the accuracy of the above approximations. A set of 10^4 voltage and current samples were given a varying normal distribution, with standard deviations varying as a percent of the nominal value. Equations C.9, C.10, and C.11 were used to

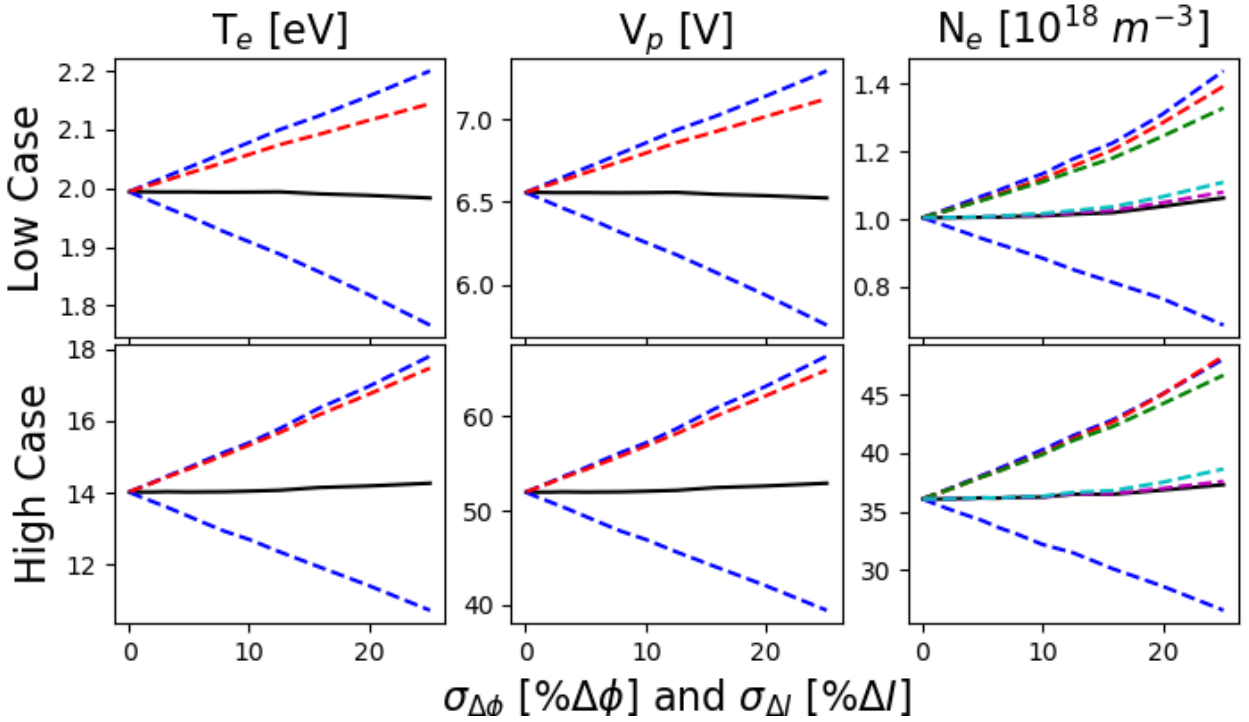

Figure C.13: Results from a statistical analysis of error propagation run for two example plasmas of low and high values of density and temperature. The x-axis shows the standard deviations of the input data $\Delta\phi$ and ΔI expressed as a percentage of the nominal value. The blue lines show the standard deviation of parameters calculated from the data. The red lines show the estimate of error from the linear model. The magenta, green, and cyan curves show the contributions from the first, second, and third terms in equation C.21.

compute the temperature, plasma potential, and density on this set. The resulting standard deviations for each were calculated and compared to the above results and plotted in Fig. C.13. The three plots use values for voltage and current that represent maximum, minimum, and expected plasma parameters for density and temperature. Note that at low values of T_e, where the linear model diverges from the non-linear solution in figure C.10, the agreement is the worst. Nonetheless, this appears to be an acceptable method for propagating the measurement error.

D PULSE FORMING NETWORKS AND PLASMA GUN ARRAY MODIFICATIONS

D.1 Pulse Forming Networks

These experiments relied heavily on plasma washer guns first developed by Gannady Fiksel [40], then later used on LTRX [12], and now heavily improved upon Pegasus experiment [62]. The washer guns are each powered by a Type E Pulse Forming Network (PFN), as shown in Fig. D.1. With 16 mF of capacitance, generally charged to 750 V, for a total stored energy $\frac{1}{2}CV^2$ of 4.5 kJ. They should be treated with lethal respect.

The PFNs discharge 1000 kA at 100 V for 10 ms, a characteristic impedance of 0.1 Ω. Typical current-voltage traces are shown in Fig. D.2. Note that the transmitted power is only 1 kJ, for a mysteriously low efficiency that is ultimately irrelevant. These PFN modules are overengineered, robust sources that have withstood substantial abuse and misuse. Below describes the modifications made to the system to optimize for, and protect from, the BRB.

When they began to be used on the BRB, the Silicon Controlled Rectifiers (SCRs) that

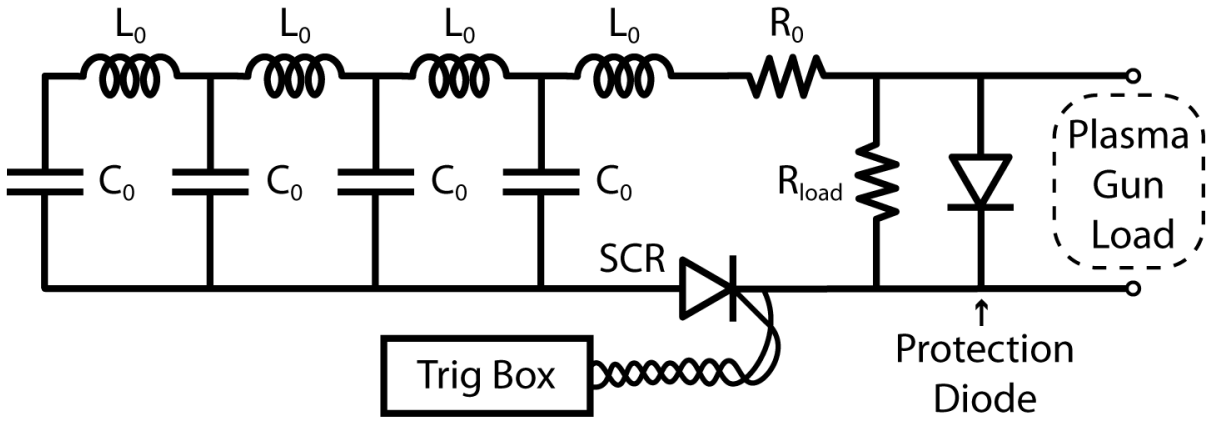

Figure D.1: Simplified circuit diagram of the Pulse Forming Networks (PFN) used to power the washer gun plasma sources. This is a standard type E PFN, where the four inductors are wound on the same support cylinder and have some mutual inductance. The two recent modifications to the circuit include the 2.5 Ω resistive load and the protective diode, both across the cathode-anode output. R_{load} serves as a high impedance load so that the SCR never "dry fires," which can lead to failure. The diodes are particularly useful for flux rope experiments, where sudden disruptions of the current led to large voltage spikes and SCR failures.

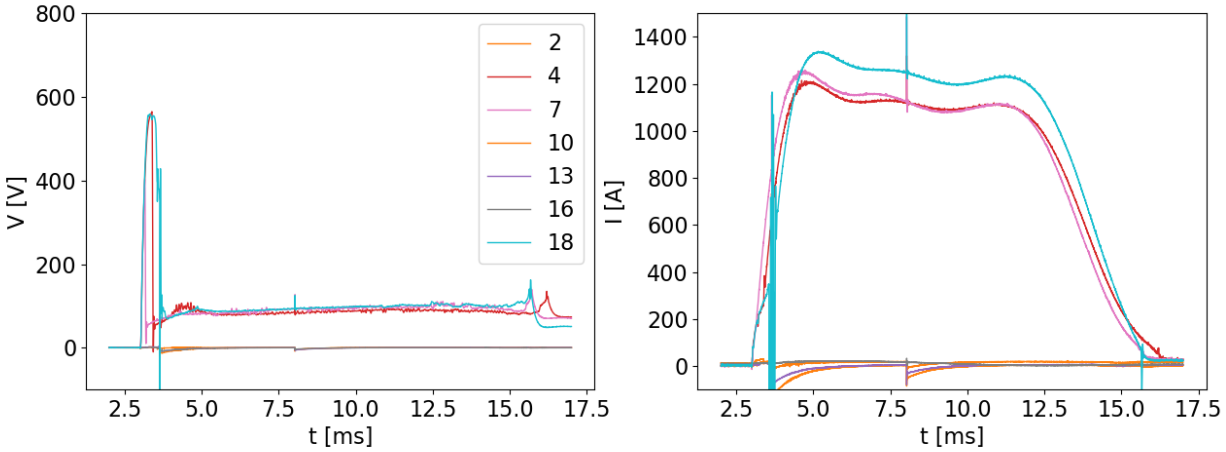

Figure D.2: Typical current and voltage traces for the plasma guns, taken from shot 48055. After the trigger but before the gas breaks down, the PFN discharges into the 2.5 Ω parallel load resistor and the voltage spikes up to ~ 550 V and the current to ~ 220 A. Once the plasma breaks down, the PFN enters its ideal operating mode where it is limited by its own internal impedance, Z ~ 1 kA/100 V = 0.1 Ω.

serve as the primary electrical switch in the PFN frequently failed. Two changes to the systerm were made to protect the SCRs: First, large "hockey-puck" type protection diodes were added across the outputs to protect against inductive voltage reversals. This was particularly necessary when the guns were being used for flux rope experiments which are prone to disruptions and inductive voltage spikes.

The second change was made after Paul Nonn observed that SCRs and thyristors generally don't appreciate being fired into open loads. To prevent this, 2.5 Ohm ballast resistors were added as a parallel load across the output terminals. This impedance is large compared to the plasma and PFN characteristic impedances. If the PFN is accidentally discharged into an open load (e.g. because of a failure of a puff valve), this ballast resistor conducts about 200 A at over 500 V, as shown in Fig. D.2. Once the plasma breaks down and provides a low impedance load, the PFN returns to its designed operating state of 1 kA at 100 V, and the ballast resistor carries only 40 A of the 1 kA total current, or a very acceptable 4% loss. Fig. D.6 plots the current-voltages traces from several guns with misbehaving puff valves. This shows how the SCRs are protected from the open load condition.

Varistors have also been added alongside the ballast resistors. However, these strongly limit the max charging voltage of the PFN. Operating at 800 V will cause those varistors to fail explosively (as they are designed to do). These should be removed.

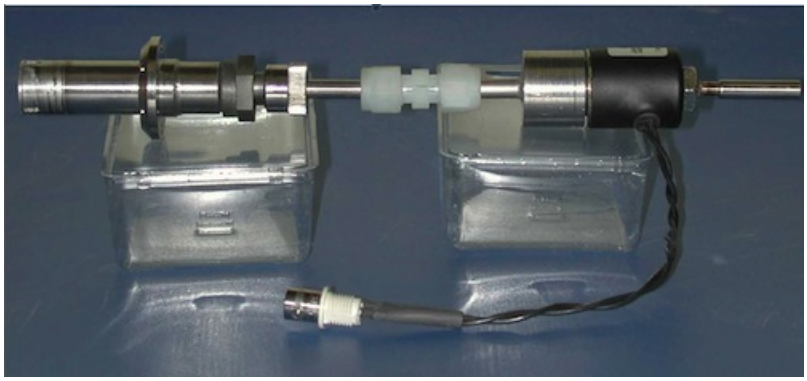

Figure D.3: A single puff valve mounted with an isolating nylon swagelok adaptor to a washer gun. Ultratorr connectors are easier to tighten in the confined space of the gun array, and most have been replaced.

D.2 Failures of the Puff Valves

In retrospect, many of the problems faced with the PFNs and washer guns came not from those systems but from the puff valves. The puff valves are produced by Precision Dynamics Inc. (model B2011-S67, orifice ID $1/16$", 24 VDC,) and are shown in the right of Fig. D.3. They have an opening time of between 1-2 ms, after which the gas must travel the length of the line (~ 40 cm) before it reaches the gun cathode.

The pre-existing PFN control circuitry includes an current-controlled interlock system that waits 10 ms after current enters the puff valve inductive relay. This was implemented to prevent the PFN from a dry-fire discharge. Unfortunately, the actuation mechanism can get stuck and the valve may not open fully. In situations like this, the interlock system does not protect the guns or PFNs from dry firing into an open load. After the two PFN changes described above protecting the SCRs, the current interlock system can be safely bypassed by jumping the appropriate leads inside the electronics box.

That these puff valves fail requires that, before and after any run campaign, each puff valves should be individually tested. A simple procedure for which follows: After temporarily closing the high vacuum pump gate valves, a single puff valve should be manually triggered, puffing gas into the BRB vessel, and the rise in the base pressure should be measured. Strong outlier valves should be replaced. Furthermore, if a voltage or current trace suddenly develops strong noise or signals of arcing (see Fig. D.6), it should immediately provoke a test of the possibly offending puff valve.

These changes to the BRB puff valve control system have significantly improved the neutral gas levels during the experiment. For Hydrogen gas at 25^{deg}C, the sound speed c_s is 450 m/s, and so in the 10 ms interlock delay period a neutral particle can travel 4.5 m. We

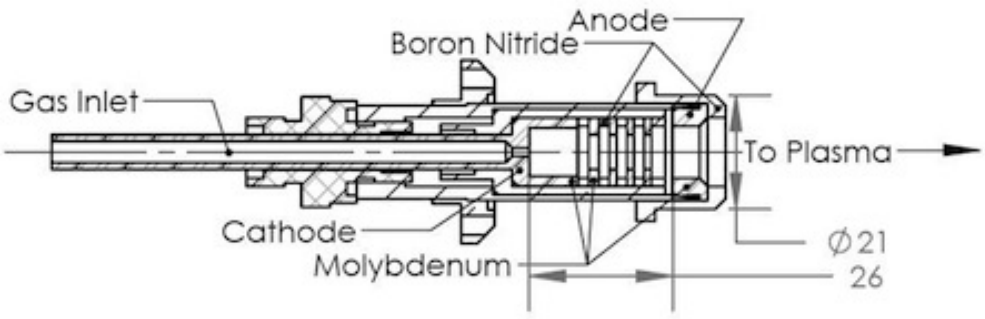

Figure D.4: Cross section of the washer gun plasma sources. Upon refurbishing, the cathode, anode, and both sets of washers are replaced. The cathode and anode have been redesigned such that the inner diameter is the same 1/4" as the washers. Image reproduced from Brookhart [12].

have every reason to believe that 10 ms after the puff valves open the vessel is filled with neutrals. This is not ideal for most experiments, where the optimum background neutral pressure is zero.

Bypassing the interlock, breakdown in the gun occurs as soon as the Paschén criterion is reached. This is almost immediately as the first neutral gas particles leave the puff valve and enter the gun barrel. With the extremely high densities and temperatures in the barrel, the plasma is likely near fully ionized as it enters the vessel. Assuming the background base pressure to be small, neutrals should then appear only through plasma recombination, and the total ionization fraction in the vessel should be vastly improved.

Without a fast measurement of the neutral density, we have not directly quantified this improvement. However, we can compare the background base pressure ($\leqslant 10^{-6}$ torr) with the base pressure post-shot ($\sim 5 \cdot 10^{-4}$ torr). Using the ideal gas law, the particle density:

$$\frac{N}{V} = \frac{P}{rT} = \frac{1e-6\text{torr}}{8.314\text{J/molK} \cdot 300\text{K}} = 3 \cdot 10^{16}\ \text{m}^{-3} \tag{D.1}$$

This density is insignificant for most experiments. However, the factor 500 increase to the peak base pressure at the end of the experiment makes the neutral density very important. A rough comparison could be made by looking at the neutral Hydrogen emission intensity and comparing that to interferometer density measurements.

D.3 Wear and Refurbishment of Plasma Guns

After several thousand shots, the molybdenum parts in the gun array generally need to be replaced. It was noticed that the outer and innermost washers eroded most severely,

Figure D.5: Image of a washer gun in dire need of refurbishment. Visible also are the copper faceplate and white Boron-nitride shield. The gun anode clearly became molten and formed the two beads visible top-left and bottom. This image was taken after the flux rope experiment configuration, in which the gun anode was used also as a cathode to drive current across the vessel.

leaving only a thin ring of molybdenum rather than a washer. It was believed this wear was exacerbated by the strong electric fields from the outer/innermost washers to the anode/cathode. To reduce these sharp edge effects, the designs were modified such that the inner radius of the cathode and anode matched the 1/4" washer ID.

However, after the realization that the puff valves are fallible, it became clear that lack of neutrals in the strongest factor in the wear experienced by the washers. A newly refurbished gun after only a few hundred shots with a malfunctioning puff valve displayed very obvious pitting and beading of melted molybdenum.

With an awareness of the importance of proper amounts of neutrals to the performance and lifetime of the guns, it is recommended that the puff valves are operated with 15-45 PSI of pressure in the foreline, and with gas puff durations of ideally 10 ms (and always greater than 3 ms).

Scientists who worked with these washer guns previously (namely M. Brookhart) stressed the importance of operating them with a modest magnetic field, claiming that such a guide field assisted in the breakdown inside the gun. A scan in guide field was performed on the BRB with a single mirror coil around the gun array, testing the gun reliability as a function of the axial magnetic field. It was observed that for fields between 100 Gauss to 1 kGauss, the guns rarely displayed arcing as in Fig. D.6. It is believed that higher fields may interfere with the puff valve actuation. Lower fields may not provide enough guide field for good breakdown, although neither of these ideas have been rigorously tested.

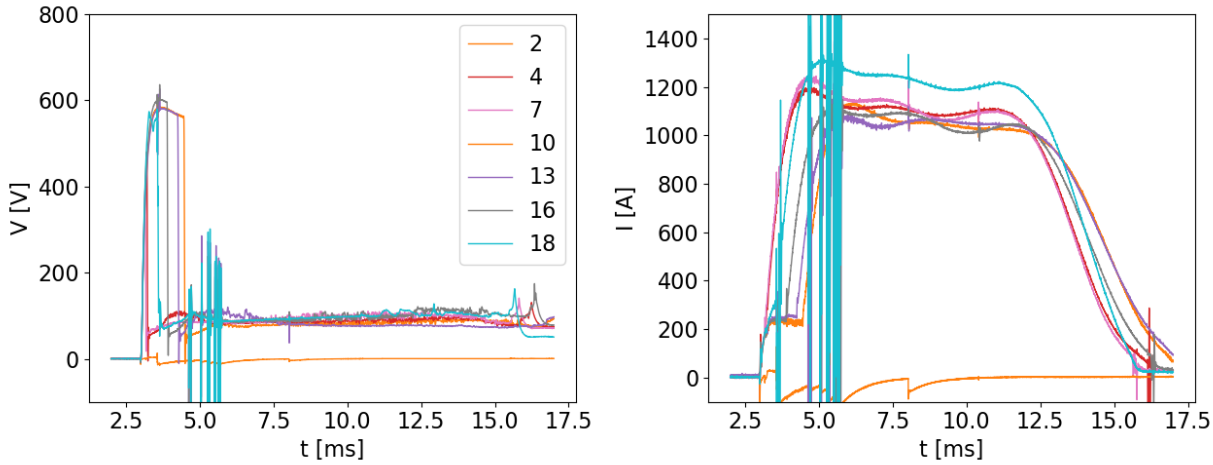

Figure D.6: Current and voltage traces from shot 48058 showing typical arcing behavior. While Gun 18 (cyan) breaks down quickly, the arcing likely indicates sputtering inside the gun. When confronted with a signal like this, the puff valve should be tested for abnormal behavior.

D.4 Isolating the gun array

In certain experiments, it is necessary to ensure proper isolation between the washer guns and the machine wall. Particularly for Flux rope experiments, where the gun anodes are biased positively against an anode across the machine, the existing PEEK insulating flange is insufficient to prevent surface arcing: rather than going through the plasma, the current often arcs along the surface of the insulation to enter the vessel wall. Such arcing has led to pitting of the 16" aluminum flanges. Thick pieces of Teflon wrapped around the array and opposing anode did not inhibit this behavior. A fully re-entrant plastic flange, with corners preventing surface arc breakdown, is the necessary next step.

D.5 Air Cooling

The gun array should always be operated with air cooling provided by compressed dry air blown on the flange outside. As a consequence of their electrical isolation, the internal washers have terrible heat conduction to the outside (good electrical insulators are generally good thermal insulators, with the exceptions of diamond and sapphire). Heat dissipation is through the boron-nitride cup is very slow. To prevent melting seen in Fig. D.5, the guns should be operated at a 3 minute rep-rate at most.

D.6 Obsolete Parts

It is becoming increasingly difficult to find manufacturers for the thyristors (SCRs). The series ST230S is a stud-mount (TO-93/TO-209AB), 1.2 kV reverse voltage standoff, capable of 5 kA of 10 ms pulsed current. Newer TO-200 puck style thyristors are not cheaper but are currently manufactured. Installing will be similar to the protection diodes (also TO-200).

BIBLIOGRAPHY

[1] Stuart Bale and Forrest Mozer. Measurement of large parallel and perpendicular electric fields on electron spatial scales in the terrestrial bow shock. *Physical review letters*, 98:205001, May 2007.

[2] C.W. Barnes, T.R. Jarboe, G.J. Marklin, S.O. Knox, and J. Henins. The impedance and energy efficiency of a coaxial magnetized plasma source used for spheromak formation and sustainment. In *U.S./Japan Compact Toroid Workshop*, Nov 1989.

[3] D. Biskamp. Collisionless shock waves in plasmas. *Nuclear Fusion*, 13(5):719–740, Oct 1973.

[4] D. Biskamp and H. Welter. Ion heating in high-mach-number, oblique, collisionless shock waves. *Phys. Rev. Letters*, 28(7):410–413, 1972.

[5] P. Bogen, K. J. Dietz, K. H. Dippel, E. Hintz, K. Hothker, F. Siemsen, and G. Zeyer. Shock waves and turbulent heating in low density plasma (iaea-cn-28/j-11). In *Plasma Physics and Controlled Nuclear Fusion Research, Volume III*, pages 277–288, 1971.

[6] J. Boris. Relativistic plasma simulations – optimization of a hybrid code. In *Proceeding of Fourth Conference on Numerical Simulations of Plasmas*, Nov 1970.

[7] N.L. Borodkova, V.G. Eselevich, G.N. Zastenker, O.V. Sapunova, Yu.I. Yermolaev, J. Šafránková, Z. Němeček, and L. Přech. Fine structure of interplanetary shock front—results from bmsw experiment with high time resolution. *Journal of Geophysical Research: Space Physics*, 124(11):8191–8207, 2019.

[8] K.J. Bowers, B. J. Albright, L. Yin, B. Bergen, and T. J. T. Kwan. Ultrahigh performance three-dimensional electromagnetic relativistic kinetic plasma simulation. *Physics of Plasmas*, 15(5):055703, 2008.

[9] K.J. Bowers, B.J. Albright, B. Bergen, L. Yin, K. J. Barker, and D. J. Kerbyson. 0.374 pflop/s trillion-particle kinetic modeling of laser plasma interaction on road-runner. *Proc. 2008 ACM/IEEE Conf. Supercomputing (Gordon Bell Prize Finalist Paper)*, 2008.

[10] K.J. Bowers, B.J. Albright, L. Yin, W. Daughton, V. Roytershteyn, B. Bergen, and T.J.T Kwan. Advances in petascale kinetic simulations with vpic and roadrunner. *Journal of Physics: Conference Series*, 180(012055), 2009.

[11] A. Bret and A. Pe'er. Bridging the gap between collisional and collisionless shock waves. *Journal of Plasma Physics*, 2(87), 2021.

[12] M.I. Brookhart. *Subcritical Onset of Plasma Fluctuations and Magnetic Self-Organization in a Line-Tied Screw Pinch*. PhD thesis, University of Wisconsin-Madison, 2015.

[13] D. Burgess. Cyclic behavior at quasi-parallel collisionless shocks. *Geophysical Research Letters*, 16(5):345–348, 1989.

[14] D Burgess. Foreshock-shock interaction at collisionless quasi-parallel shocks. *Advances in Space Research*, 15(8):159–169, 1995. Proceedings of the D2.1 Symposium of COSPAR Scientific Commission D.

[15] D. Burgess and M. Scholer. *Microphysics of Quasi-parallel Shocks in Collisionless Plasmas*, pages 437–457. Space Sciences Series of ISSI. Springer US, Boston, MA, 2013.

[16] David Burgess and Manfred Scholer. *Collisionless Shocks in Space Plasmas: Structure and Accelerated Particles*. Cambridge Atmospheric and Space Science Series. Cambridge University Press, 2015.

[17] T. Byvank, S.J. Langendorf, C. Thoma, and S.C. Hsu. Observation of shock-front separation in multi-ion-species collisional plasma shocks. *Physics of Plasma*, 27(042302), 2020.

[18] H.V. Cane, R.E. McGuire, and T.T. Von Rosenvinge. Two classes of solar energetic particle events associated with impulsive and long-duration soft x-ray flares. *The Astrophysical Journal*, 301:448–459, Feb 1986.

[19] D. Caprioli and A. Spitkovsky. Simulations of ion acceleration at non-relativistic shocks. i. acceleration efficiency. *The Astrophysical Journal*, 783(2):91, Feb 2014.

[20] Francis F. Chen. Helicon discharges and sources: a review. *Plasma Sources Science and Technology*, 24(1):014001, Jan 2015.

[21] Francis F. Chen. *Introduction to Plasma Physics and Controlled Fusion*. Springer, Spring Int'l Publishing Switzerland, 3 edition, 2016.

[22] L.J. Chen et al. Electron bulk acceleration and thermalization at earth's quasiperpendicular bow shock. *Physical Review Letters*, 120(22):225101, June 2018.

[23] L.J. Chen et al. Solitary magnetic structures at quasi-parallel collisionless shocks: Formation. *Geophysical Research Letters*, 48(1), 2021.

[24] Sin-Li Chen and T. Sekiguchi. Instantaneous direct-display system of plasma parameters by means of triple probe. *Journal of Applied Physics*, 36(8):2363–2375, 1965.

[25] Robert S. Cohen, Lyman Spitzer, and Paul McR. Routly. The electrical conductivity of an ionized gas. *Phys. Rev.*, 80:230–238, Oct 1950.

[26] F.V. Coroniti. Dissipation discontinuities in hydromagnetic shock waves. *Journal of Plasma Physics*, 4:265–282, May 1970.

[27] C. D. Cothran, M. R. Brown, T. Gray, M. J. Schaffer, and G. Marklin. Observation of a helical self-organized state in a compact toroidal plasma. *Phys. Rev. Lett.*, 103:215002, Nov 2009.

[28] A.D. Craig and J.W.M. Paul. Observation of a 'switch-on' shock in a magnetized plasma. *Journal of Plasma Physics*, 9(2):161–186, 1973.

[29] B. Dasgupta, R. Burrows, G. P. Zank, and G. M. Webb. Hydrodynamics of shock waves with reflected particles. i. rankine-hugoniot relations and stationary solutions. *Physics of Plasmas*, 13(8):082112, 2006.

[30] W.D. Davis. Spectroscopic observations of turbulence in a fast theta pinch. *The Physics of Fluids*, 15(12):2383–2390, 1972.

[31] W.D. Davis, A.W. DeSilva, W.F. Dove, H.R. Griem, N.A. Krall, and P.C. Liewer. Ion heating in a high voltage theta pinch (iaea-cn-28/j-12). In *Plasma Physics and Controlled Nuclear Fusion Research, Volume III*, pages 289–302, 1971.

[32] H. De Sterck, B. C. Low, and S. Poedts. Complex magnetohydrodynamic bow shock topology in field-aligned low-β flow around a perfectly conducting cylinder. *Physics of Plasmas*, 5(11):4015–4027, 1998.

[33] D.J. den Hartog and R.J. Fonck. A fast spectroscopic diagnostic for the measurement of plasma impurity ion dynamics. *Review Scientific Instruments*, 65(20):3238–3242, October 1994.

[34] C. L. Dobbs. Gmc formation by agglomeration and self gravity. *Monthly Notices of the Royal Astronomical Society*, 391(2):844–858, Dec 2008.

[35] J. P. Edmiston, C. F. Kennel, and David Eichler. Escape of heated ions upstream of quasi-parallel shocks. *Geophysical Research Letters*, 9(5):531–534, 1982.

[36] J.P. Edmiston and C.F. Kennel. A parametric survey of the first critical mach number for a fast mhd shock. *Journal of Plasma Physics*, 32(3):429–441, Dec 1984.

[37] T. Edo et al. Performance improvement of a magnetized coaxial plasma gun by adopting iron-core bias coil and pre-ionization systems. *Plasma and Fusion Research*, 13:3405062–3405062, 2018.

[38] Douglass Endrizzi, J. Egedal, M. Clark, K. Flanagan, S. Greess, J. Milhone, A. Millet-Ayala, J. Olson, E. E. Peterson, J. Wallace, and C. B. Forest. Laboratory resolved structure of supercritical perpendicular shocks. *Phys. Rev. Lett.*, 126:145001, Apr 2021.

[39] Victor Eselevich, N. Borodkova, O. Sapunova, G. Zastenker, and Y. Yermolaev. Effect of reflected ions on the formation of the structure of interplanetary quasi-perpendicular shocks for mach numbers lower than the first critical mach number. *Cosmic Research*, 55:403–416, 11 2017.

[40] G. Fiksel, A.F. Almagri, D. Craig, M. Iida, S.C. Prager, and J.S. Sarff. High current plasma electron emitter. *Plasma Sources Science and Technology*, 5(1):78–83, Feb 1996.

[41] W.L. Fite. Free hydrogen atom cross sections of interest in controlled thermonuclear research. *IAEA Conference Proceedings*, Session A-10:P/348, 1958.

[42] Richard Fitzpatrick. *Plasma Physics: An Introduction*. CRC Press, 2015.

[43] F. Fiuza, G.F. Swadling, A. Grassi, et al. Electron acceleration in laboratory-produced turbulent collisionless shocks. *Nat. Phys.*, 16:916–920, 2020.

[44] C.B. Forest et al. The wisconsin plasma astrophysics laboratory. *Journal of Plasma Physics*, 81(5):345810501, 2015.

[45] D. W. Forslund, R. L. Morse, and C. W. Nielson. Nonlinear electron-cyclotron drift instability and turbulence. *Phys. Rev. Lett.*, 27:1424–1428, Nov 1971.

[46] D. W. Forslund, K. B. Quest, J. U. Brackbill, and K. Lee. Collisionless dissipation in quasi-perpendicular shocks. *Journal of Geophysical Research: Space Physics*, 89(A4):2142–2150, 1984.

[47] S. Gary. Electromagnetic ion/ion instabilities and their consequences in space plasmas: A review. *Space Science Reviews*, 56, Jun 1991.

[48] M. Gedalin. Collisionless relaxation of non-gyrotropic downstream ion distributions: dependence on shock parameters. *Journal of Plasma Physics*, 81(6):905810603, 2015.

[49] M. Gedalin. Transmitted, reflected, quasi-reflected, and multiply reflected ions in low-mach number shocks. *Journal of Geophysical Research: Space Physics*, 121(11):10,754–10,767, 2016.

[50] M. Gedalin and M. Balikhin. Rankine–hugoniot relations for shocks with demagnetized ions. *Journal of Plasma Physics*, 74(2):207–214, 2008.

[51] C. G. R. Geddes, T. W. Kornack, and M. R. Brown. Scaling studies of spheromak formation and equilibrium. *Physics of Plasmas*, 5(4):1027–1034, 1998.

[52] Imogen Gingell et al. Mms observations and hybrid simulations of surface ripples at a marginally quasi-parallel shock. *Journal of Geophysical Research: Space Physics*, 122(11):11,003–11,017, 2017.

[53] R.J. Goldston and P.H. Rutherford. *Introduction to Plasma Physics*. Institute of Physics Publishing, Bristol and Philadelphia, 1995.

[54] Katherine A. Goodrich et al. Mms observations of electrostatic waves in an oblique shock crossing. *Journal of Geophysical Research: Space Physics*, 123(11):9430–9442, 2018.

[55] E. W. Greenstadt and M. M. Mellott. Plasma wave evidence for reflected ions in front of subcritical shocks: Isee 1 and 2 observations. *Journal of Geophysical Research: Space Physics*, 92(A5):4730–4734, 1987.

[56] S. Greess, J. Egedal, A. Stanier, W. Daughton, J. Olson, A. Le, R. Myers, A. Millet-Ayala, M. Clark, J. Wallace, D. Endrizzi, and C. Forest. Laboratory verification of electron-scale reconnection 2 regions modulated by a three-dimensional instability. *Journal Geophysical Research: Space Physics*, 2021.

[57] E. Hairer and C. Lubich. Energy behaviour of the boris method for charged-particle dynamics. *Bit Numer Math*, 58:969–979, 2018.

[58] E. L. M. Hanson, O. V. Agapitov, F. S. Mozer, V. Krasnoselskikh, S. D. Bale, L. Avanov, Y. Khotyaintsev, and B. Giles. Cross-shock potential in rippled versus planar quasi-perpendicular shocks observed by mms. *Geophysical Research Letters*, 46(5):2381–2389, 2019.

[59] E. Heintz, C. Bustard, and E.G. Zweibel. The role of the parker instability in structuring the interstellar medium. *The Astrophysical Journal*, 891(2):157, mar 2020.

[60] Robert A. Helliwell. *Whistlers and Related Ionospheric Phenomena*. Stanford University Press, Stanford, CA, 1965.

[61] Peter Heuer et al. Laboratory observations of ultra-low frequency analogue waves driven by the right-hand resonant ion beam instability. *The Astrophysical Journal Letters*, 891:L11, Feb 2020.

[62] E. T. Hinson, J. L. Barr, M. W. Bongard, M. G. Burke, R. J. Fonck, and J. M. Perry. Impedance of an intense plasma-cathode electron source for tokamak startup. *Physics of Plasmas*, 23(5):052515, 2016.

[63] Y. Hobara, M. Balikhin, V. Krasnoselskikh, Michael Gedalin, and H. Yamagishi. Statistical study of the quasi-perpendicular shock ramp widths. *Journal of Geophysical Research*, 115, Nov 2010.

[64] J.D. Huba. *NRL Plasma Formulary*. The Office of Naval Research, 2013.

[65] I.H. Hutchinson. *Principles of Plasma Diagnostics, 2nd Ed.* Cambridge University Press, 2002.

[66] Michel Y. Jaffrin and Ronald F. Probstein. Structure of a plasma shock wave. *The Physics of Fluids*, 7(10):1658–1674, 1964.

[67] A. Johlander et al. Rippled quasiperpendicular shock observed by the magnetospheric multiscale spacecraft. *Phys. Rev. Lett.*, 117:165101, Oct 2016.

[68] B.D. Keenan, A.N. Simakov, W.T. Taitano, and L. Chacón. Ion species stratification within strong shocks in two-ion plasmas. *Physics of Plasmas*, 25(3):032103, 2018.

[69] M. Keilhacker, M. Kornherr, H. Niedermeyer, K.H. Steuer, and R. Chodura. Experimental study of collective dissipation in shock waves for a wide range of plasma parameters (IAEA-CN-28/J-10). In *Plasma Physics and Controlled Nuclear Fusion Research, Volume III*, page 265, 1971.

[70] C.F. Kennel, J.P. Edmiston, and T. Hada. *A Quarter Century of Collisionless Shock Research*, chapter 1, pages 1–36. American Geophysical Union (AGU), 2013.

[71] V. Krasnoselskikh, M. Balikhin, S.N. Walker, et al. The dynamic quasiperpendicular shock: Cluster discoveries. *Space Sci Rev*, 178:535–598, 2013.

[72] V. Krasnoselskikh, Bertrand Lembège, P. Savoini, and Vasili Lobzin. Nonstationarity of strong collisionless quasiperpendicular shocks: Theory and full particle numerical simulations. *Physics of Plasmas*, 9:1192–1209, Apr 2002.

[73] M. M. Leroy, D. Winske, C. C. Goodrich, C. S. Wu, and K. Papadopoulos. The structure of perpendicular bow shocks. *Journal of Geophysical Research: Space Physics*, 87(A7):5081–5094, 1982.

[74] W.A. Livesey, C.T. Russell, and C.F. Kennel. A comparison of specularly reflected gyrating ion orbits with observed shock foot thicknesses. *Journal of Geophysical Research*, 89(A8):6824–6828, Aug. 1984.

[75] V. V. Lobzin, V. V. Krasnoselskikh, J.-M. Bosqued, J.-L. Pinçon, S. J. Schwartz, and M. Dunlop. Nonstationarity and reformation of high-mach-number quasiperpendicular shocks: Cluster observations. *Geophysical Research Letters*, 34(5), 2007.

[76] R. Lowe and Devin Burgess. The properties and causes of rippling in quasi-perpendicular collisionless shock front. *Annales Geophysicae*, 21, 03 2003.

[77] E. A. Lucek, T. S. Horbury, I. Dandouras, and H. Rème. Cluster observations of the earth's quasi-parallel bow shock. *Journal of Geophysical Research: Space Physics*, 113(A7), 2008.

[78] T. Matsumoto et al. Development of a magnetized coaxial plasma gun for compact toroid injection into the c-2 field-reversed configuration device. *Review of Scientific Instruments*, 87(5):053512, 2016.

[79] C. Mazelle, Bertrand Lembege, A. Morgenthaler, Karim Meziane, T. Horbury, Vincent Génot, Elizabeth Lucek, and Iannis Dandouras. Self-reformation of the quasi-perpendicular shock: Cluster observations. *Twelfth International Solar Wind Conference*, 1216, 03 2010.

[80] R.L. Merlino, G.C. Goldenbaum, C. Chin-Fatt, Y.P. Chong, A.W. DeSilva, H.R. Griem, R.A. Hess, and D. P. Murphy. Electron and ion heating in a high-voltage toroidal theta pinch with parallel or antiparallel bias fields. *The Physics of Fluids*, 24(12):2358–2371, 1981.

[81] Elizabeth C. Merritt, Auna L. Moser, Scott C. Hsu, Colin S. Adams, John P. Dunn, A. Miguel Holgado, and Mark A. Gilmore. Experimental evidence for collisional shock formation via two obliquely merging supersonic plasma jets. *Physics of Plasmas*, 21(5):055703, 2014.

[82] S. Messer, A. Case, L. Wu, S. Brockington, and F. D. Witherspoon. Nonlinear compressions in merging plasma jets. *Physics of Plasmas*, 20(3):032306, 2013.

[83] C. Niemann, W. Gekelman, C. G. Constantin, E. T. Everson, D. B. Schaeffer, A.S. Bondarenko, S.E. Clark, D. Winske, S. Vincena, B. Van Compernolle, and P. Pribyl. Observation of collisionless shocks in a large current-free laboratory plasma. *Geophysical Research Letters*, 41(21):7413–7418, 2014.

[84] J. Olson. *Exploring Driven, High Lundquist Number Magnetic Reconnection in the Laboratory: Studies of Sub-Ion Scale Plasmoids, and the Interplay between Shocks and Magnetic Flux Pileup*. PhD thesis, University of Wisconsin-Madison, 2020.

[85] J. Olson, J. Egedal, S. Greess, R. Myers, M. Clark, D. Endrizzi, K. Flanagan, J. Milhone, E. Peterson, J. Wallace, D. Weisberg, and C. B. Forest. Experimental demonstration of the collisionless plasmoid instability below the ion kinetic scale during magnetic reconnection. *Phys. Rev. Lett.*, 116:255001, Jun 2016.

[86] T. G. Onsager, D. Winske, and M. F. Thomsen. Interaction of a finite-length ion beam with a background plasma: Reflected ions at the quasi-parallel bow shock. *Journal of Geophysical Research: Space Physics*, 96(A2):1775–1788, 1991.

[87] F.G.E. Pantellini, A. Heron, J.C. Adam, and A. Mangeney. The role of the whistler precursor during the cyclic reformation of a quasi-parallel shock. *Journal of Geophysical Research*, 97(A2):1303–1311, Feb 1992.

[88] K. Papadopoulos. *Microinstabilities and Anomalous Transport*, pages 59–90. American Geophysical Union (AGU), 2013.

[89] H.-S. Park et al. Collisionless shock experiments with lasers and observation of weibel instabilities. *Physics of Plasmas*, 22(5):056311, 2015.

[90] G. Paschmann, N. Sckopke, S.J. Bame, and J.T. Gosling. Observations of gyrating ions in the foot of the nearly perpendicular bow shock. *Geophysical Research Letters*, 9(8):881–884, 1982.

[91] J. Paul, L. Holmes, and M. Parkinson. Experimental observations on the structure of collisionless shock waves in a magnetized plasma. *Nature*, 208:133–135, 1985.

[92] J.W.M. Paul, C.C. Daughney, L.S. Holmes, P.T. Rumsby, A.D. Craig, E.L. Murray, D.D.R. Summers, and J. Beaulieu. Experimental study of collisionless shock waves (iaea-cn-28/j-9). In *Plasma Physics and Controlled Nuclear Fusion Research, Volume III*, pages 251–263, 1971.

[93] E. W. Peterson and L. Talbot. Collisionless electrostatic single-probe and double-probe measurements. *AIAA Journal*, 8(12):2215–2219, 1970.

[94] Ethan E. Peterson, Douglass A. Endrizzi, Michael Clark, Jan Egedal, Kenneth Flanagan, Nuno F. Loureiro, Jason Milhone, Joseph Olson, Carl R. Sovinec, John Wallace, and Cary B. Forest. Laminar and turbulent plasmoid ejection in a laboratory parker spiral current sheet, 2021.

[95] P.E. Phillips and A.E. Robson. Influence of reflected ions on the magnetic structure of a collisionless shock front. *Physical Review Letters*, 29(3):154–157, July 1972.

[96] S. A. Pope, M. Gedalin, and M. A. Balikhin. The first direct observational confirmation of kinematic collisionless relaxation in very low mach number shocks near the earth. *Journal of Geophysical Research: Space Physics*, 124(3):1711–1725, 2019.

[97] E. Priest. *Magnetohydrodynamics of the Sun*. Cambridge University Press, 2014.

[98] L. et al Romagnani. Observations of collisionless shocks in laser-plasma experiments. *Physical Review Letters*, 101:025004, Jul 2008.

[99] M. Rosenbluth. Infinite conductivity theory of the pinch. *Los Alamos Scientific Laboratory, Controlled Thermonuclear Processes*, 1954.

[100] R.Z. Sagdeev. Cooperative phenomena and shock waves in collisionless plasmas. *Reviews of Plasma Physics*, 4:23, Jan 1966.

[101] Manfred Scholer. Upstream waves, shocklets, short large-amplitude magnetic structures and the cyclic behavior of oblique quasi-parallel collisionless shocks. *Journal of Geophysical Research: Space Physics*, 98(A1):47–57, 1993.

[102] Manfred Scholer, Harald Kucharek, and Iku Shinohara. Short large-amplitude magnetic structures and whistler wave precursors in a full-particle quasi-parallel shock simulation. *Journal of Geophysical Research*, 108, July 2003.

[103] Steven Schwartz, Edmund Henley, Jeremy Mitchell, and V. Krasnoselskikh. Electron temperature gradient scale at collisionless shocks. *Physical review letters*, 107:215002, Nov 2011.

[104] Steven J. Schwartz and David Burgess. Quasi-parallel shocks: A patchwork of three-dimensional structures. *Geophysical Review Letters*, 18(3):373–376, 1991.

[105] N. Sckopke, G. Paschmann, S. J. Bame, J. T. Gosling, and C. T. Russell. Evolution of ion distributions across the nearly perpendicular bow shock: Specularly and non-specularly reflected-gyrating ions. *Journal of Geophysical Research: Space Physics*, 88(A8):6121–6136, 1983.

[106] Jack D. Scudder. On the Causes of Temperature Change in Inhomogeneous Low-Density Astrophysical Plasmas. *The Astrophysical Journal*, 398:299, Oct 1992.

[107] J.D. Scudder, A. Mangeney, C. Lacombe, C.C. Harvey, T.L. Aggson, R.R. Anderson, J.T. Gosling, G. Paschmann, and C.T. Russell. The resolved layer of a collisionless, high beta, supercritical, quasi-perpendicular shock wave: 1. rankine-hugoniot geometry, currents, and stationarity. *Journal of Geophysical Research: Space Physics*, 91(A10):11019–11052, 1986.

[108] R. L. Stenzel. Self-ducting of large-amplitude whistler waves. *Phys. Rev. Lett.*, 35:574–577, Sep 1975.

[109] R. L. Stenzel. Whistler waves in space and laboratory plasmas. *Journal of Geophysical Research: Space Physics*, 104(A7):14379–14395, 1999.

[110] A. H. Sulaiman, A. Masters, M. K. Dougherty, D. Burgess, M. Fujimoto, and G. B. Hospodarsky. Quasiperpendicular high mach number shocks. *Phys. Rev. Lett.*, 115:125001, Sep 2015.

[111] D Gary Swanson. *Plasma Waves, 2nd Edition*. Institute of Physics Publishing, 2003.

[112] D.A. Tidman and N.A. Krall. *Shock waves in collisionless plasmas*. Wiley-Interscience, 1971.

[113] B.T. Tsurutani and P. Rodriguez. Upstream waves and particles - an overview of isee results. *Journal Geophysical Research*, 86:4317, Jun 1981.

[114] M.S. Weidl, P. Heuer, D. Schaeffer, R. Dorst, D. Winske, C. Constantin, and C.. Niemann. Towards a parallel collisionless shock in LAPD. *Journal of Physics: Conference Series*, 900:012020, Sep 2017.

[115] D.B. Weisberg. *PURSUING THE PLASMA DYNAMO AND MRI IN THE LABORATORY :HYDRODYNAMIC STUDIES OF UNMAGNETIZED PLASMAS AT LARGE-MAGNETIC REYNOLDS NUMBER*. PhD thesis, University of Wisconsin-Madison, 2016.

[116] W.P. Wilkinson and S.J. Schwartz. Parametric dependence of the density of specularly reflected ions at quasiperpendicular collisionless shocks. *Planetary and Space Science*, 38(3):419–435, 1990.

[117] L. B. Wilson III, C. A. Cattell, P. J. Kellogg, K. Goetz, K. Kersten, J. C. Kasper, A. Szabo, and M. Wilber. Large-amplitude electrostatic waves observed at a supercritical interplanetary shock. *Journal of Geophysical Research: Space Physics*, 115(A12), 2010.

[118] L. B. Wilson III, A. Koval, A. Szabo, A. Breneman, C. A. Cattell, K. Goetz, P. J. Kellogg, K. Kersten, J. C. Kasper, B. A. Maruca, and M. Pulupa. Observations of electromagnetic whistler precursors at supercritical interplanetary shocks. *Geophysical Research Letters*, 39(8), 2012.

[119] L. B. Wilson III, A. Koval, A. Szabo, M. L. Stevens, J. C. Kasper, C. A. Cattell, and V. V. Krasnoselskikh. Revisiting the structure of low-mach number, low-beta, quasi-perpendicular shocks. *Journal of Geophysical Research: Space Physics*, 122(9):9115–9133, 2017.

[120] L. B. Wilson III, D. G. Sibeck, A. W. Breneman, O. Le Contel, C. Cully, D. L. Turner, V. Angelopoulos, and D. M. Malaspina. Quantified energy dissipation rates in the terrestrial bow shock: 1. analysis techniques and methodology. *Journal of Geophysical Research: Space Physics*, 119(8):6455–6474, 2014.

[121] L.B. Wilson III, Li-Jen Chen, and Vadim Roytershteyn. The discrepancy between simulation and observation of electric fields in collisionless shocks. *Frontiers in Astronomy and Space Sciences*, 7:97, 2021.

[122] D.F. Witherspoon, A. Case, S.J. Messer, R. Bomgardner, M.W. Phillips, S. Brockington, and R. Elton. A contoured gap coaxial plasma gun with injected plasma armature. *Review of Scientific Instruments*, 80(8):083506, 2009.

[123] L.C. Woods. On double-structured, perpendicular, magneto-plasma shock waves. *Plasma Physics*, 13(4):289–302, Jan 1971.